Energie, Matériaux et Télécommunications Research Centre (EMT)

CONTROLLING THE MORPHOLOGY OF HEAVILY DOPED NEODYMIUM (Nd^{3+}) ION IN RARE EARTH NANOPARTICLES (RENPs) FOR FUTURE USE IN CANCER THERAPY.

Par

Chizoba Anita Duru

Thèse présenté(e) pour l'obtention du grade de

Maître ès Sciences (M. Sc.)

Jury d'évaluation

Président du jury et examinateur interne	Prof. Bienvenu Ndagano Institut National De La Recherché Scientifique EMT
Examinateur externe	Prof. Sigoli Fernado University of Campinas
Examinateur interne	Prof. Bienvenu Ndagano Institut National De La Recherché Scientifique EMT
Directeur de recherche	Prof. Fiorenzo Vetrone Institut National De La Recherché Scientifique EMT
Codirecteur de recherche	Prof. Federico Rosei Institut National De La Recherché Scientifique EMT

REMERCIEMENTS

I would like to thank God almighty for the strength and wisdom given to me to be able to complete this project.

It is a privilege to study at the Centre for Energy, Materials and Telecommunications, Institut National de la Recherche Scientifique (INRS-EMT), University of Quebec, Canada. The amazing facilities and community made my research work easier and the learning process faster. To my colleagues, Miao and Arohan that taught me the lab work, I am grateful. Thanks to the INRS community for the encouragement and support.

To my supervisors, Prof Federico Rosei and Prof Fiorenzo Vetrone, thank you for the financial, mental, and academic support throughout the duration of my study. It was indeed a learning experience for me.

Thanks to all my teachers for the knowledge imparted via the courses taught, presentations, and assignments. I have gained invaluable experience that would further impact the scientific and industrial world.

I would also like to thank every single employee that makes up the EMT centre, it was an honour working with you, IT department, thank you for responding to my technical needs, the first aid department, thank you for ensuring my safety, the receptionist, thank you for answering all my questions, CSEIME, PHOTONICS and every other groups, thank you for the trainings, social skills acquisitions.

I want to especially thank my family back in Nigeria for their unwavering support and love. I love you Mrs Gladys, Chidinma, Obinna, Tochukwu and Ogechi. To my wonderful friends, to mention but a few, Omachonu, Ikogi, Edmond, Peter, Abimbola, Charles, Benenwei, thank you all so much for the emotional support.

Finally, my gratitude also goes to my church community, Christ Embassy Lasalle, Montreal. Thank y'all for supporting me throughout this journey.

RÉSUMÉ

CONTRÔLE DE LA MORPHOLOGIE DE L'ION NÉODYME (Nd^{3+}) FORTEMENT DOPÉ DANS LES NANOPARTICULES DE TERRES RARES (SNP) POUR UTILISATION FUTURE DANS LA THERAPIE CONTRE LE CANCER.

Les nanoparticules à base de terres rares (RENPs) possèdent un potentiel significatif pour des applications en milieu biologique, à condition qu'elles puissent émettre de la lumière avec une intensité élevée. Pour atteindre cet objectif, il est crucial qu'elles présentent une efficacité optimale d'absorption pour des longueurs d'onde qui ne sont ni absorbées ni diffusées par les tissus biologiques. Une longueur d'onde de 800 nm, dite « biocompatible », est souvent privilégiée car elle réduit l'atténuation du signal et minimise le chauffage nocif tout en permettant une pénétration profonde dans les tissus. En utilisant le néodyme (Nd^{3+}) conjointement avec l'ytterbium (Yb^{3+}) dans des RENPs à base de lanthanides, il est possible de déplacer l'absorption de 980 nm à 800 nm, une plage où l'eau n'absorbe pas la lumière. Des concentrations élevées en Nd^{3+} (60 mol%) sont avantageuses car elles augmentent à la fois l'absorption et l'émission. Cependant, les nanoparticules fortement dopées RENPs rencontrent souvent des limitations dues aux distorsions du réseau cristallin dans qu'elles soient de type cœur ou cœur-noyau (CS NPs). Ce défi est relevé en optimisant les méthodes de synthèse, notamment en ajustant la température, la concentration des solvants et la durée de réaction.

Cette étude porte sur la synthèse, le contrôle morphologique et l'application de néodyme (Nd^{3+}) fortement dopé pour des usages futurs dans les thérapies photodynamiques (PDT), photothermiques (PTT) et en nanothermomètrie. Ici, le $LiYbF_4$ est utilisé comme matrice hôte pour les RENPs en raison de sa faible énergie photonique, qui favorise une intensité de luminescence élevée avec du Nd^{3+} fortement dopé. Les performances de luminescence ont été optimisées en construisant une structure cœur/noyau ($LiYbF_4$: Nd^{3+}@$LiYF_4$), qui aide à minimiser l'extinction de la luminescence causée par les défauts. La méthode de synthèse par décomposition thermique a été utilisée pour obtenir des nanoparticules monodisperses. L'ajustement des conditions de réaction, telles que la température et la durée, a permis de former différentes morphologies. Plus précisément, une température de réaction de 330 °C et une durée de 2 h ont favorisé la formation de particules de taille plus grande et plus uniforme. La présence de surfactants comme l'acide oléique (OA), l'oléylamine (OM) et l'octadécène (ODE) a influencé leur forme et leur distribution de taille. La morphologie des RENPs a été caractérisée à l'aide des techniques TEM, SEM, XRD et EDX. De plus, les propriétés de luminescence, pour déterminer

la luminescence descendante et la luminescence en fonction de la température (nanothermométrie), ont été analysées par spectroscopie de photoluminescence (PL). La morphologie des RENPs joue un rôle clé dans la détermination des propriétés optiques, des interactions biologiques et de la détection non invasive de la température, ce qui est essentiel pour assurer une efficacité globale dans le traitement du cancer. Des nanoparticules uniformes et bien définies présentent une excellente efficacité de luminescence, une meilleure absorption cellulaire et une distribution améliorée dans l'organisme.

Mots-clés : nanoparticules à base de terres rares, proche infrarouge, dopants, décomposition thermique, photoluminescence, luminescence descendante, thérapies photothermiques.

ABSTRACT

Rare-earth nanoparticles (RENPs) have significant potential for use in biological settings, provided they can emit light with high intensity. To achieve this, it's crucial that they have optimal absorption efficiencies for wavelengths that are neither absorbed nor scattered by biological tissues. A wavelength of 800 nm 'biobenign' is often favored because it reduces signal attenuation and minimizes harmful heating while allowing for deep tissue penetration. By using neodymium (Nd^{3+}) together with ytterbium (Yb^{3+}) in lanthanide-based RENPs, it's possible to shift the absorption from 980 nm to 800 nm, a range where water does not absorb light. High concentrations of Nd^{3+} concentrations (60 mol%) are advantageous because they enhance both absorption and emission. However, heavily doped RENPs often face limitations due to lattice distortions in core and core–shell nanoparticles (CS NPs). This challenge is addressed by optimizing synthesis method which involves adjusting the temperature, solvent concentration and reaction time.

This study focuses on the synthesis, morphological control and application of heavily doped Neodymium (Nd^{3+}) for future use in photodynamic (PDT), photothermal therapies (PTT) and nanothermometry. Here $LiYbF_4$ is used as a host matrix for RENPs because of its low phonon energy which gives way to high luminescence intensity with heavily doped Nd^{3+}. The luminescence performance was optimized by constructing a core/shell structure ($LiYbF_4$:Nd^{3+}@$LiYF_4$) which helps to minimize luminescent quenching caused defects. Thermal decomposition synthesis method was used here to achieve the monodisperse nanoparticles. Adjusting the reaction conditions such as temperature and time allowed for the formation of different morphology. Specifically, a reaction temperature of 330 ^oC and reaction time of 2 h favoured the formation of larger and more uniform particle size. The presence of surfactants such Oleic Acid (OA), Olyeamine (OM) and Octadecene (ODE) influenced their shape and distribution of size. The morphology of RENPs was characterized using TEM, SEM, XRD, and EDX technique. Also, the luminescence properties to determine the downshifiting luminescence and luminescence as a function of temperature (nanothermometry) were analyzed using the photoluminescence (PL) spectroscopy.

The morphology of RENPs is important in determining the optical properties, biological interactions, non invasive temperature detection which is important in ensuring the overall efficiency in cancer treatment. Uniformly shaped and well-defined nanoparticles shows great luminescence efficiency, improved cellular uptake and enhanced biodistribution.

Keywords : rare-earth nanoparticles, near infrared, dopants, thermal decomposition, photoluminescence, downshifiting, photothermal therapies.

SOMMAIRE RÉCAPITULATIF

Chapitre 1

Introduction

Aperçu de l'impact de la nanotechnologie dans les domaines biomédicaux

La nanotechnologie a considérablement transformé les sciences biomédicales, fournissant de nouveaux outils pour le diagnostic, l'imagerie et la thérapie. Les nanoparticules, en raison de leur petite taille et de leurs propriétés uniques, peuvent interagir avec les systèmes biologiques au niveau moléculaire, offrant des possibilités sans précédent d'améliorer l'efficacité des traitements médicaux [3]. Les nanoparticules sont à l'étude pour leur potentiel dans l'administration de médicaments ciblés, l'imagerie non invasive et en tant qu'agents thérapeutiques dans le traitement du cancer [4]. L'utilisation de la lumière pour déclencher des nanoparticules et des médicaments qu'ils transportent représente une nouvelle approche pour le traitement non invasif de différentes maladies. L'utilisation de ces caractéristiques optiques uniques permet l'imagerie et le traitement ciblés de zones spécifiques tout en minimisant l'exposition aux parties non affectées du corps [5]. Parmi les différents types de nanoparticules, les nanoparticules de terres rares (RENPs) ont attiré une attention considérable pour leur capacité à convertir la lumière proche infrarouge (NIR) à faible énergie en lumière visible ou ultraviolette de plus haute énergie [6]. Cette propriété est particulièrement avantageuse dans les applications biomédicales, car la lumière NIR peut pénétrer plus profondément dans les tissus biologiques avec un photodamage minimal [3]. Les RENPs se sont révélés prometteurs en améliorant la sensibilité et la résolution des techniques de bioimagerie et en permettant des modalités thérapeutiques innovantes [7]. Les progrès continus dans ce domaine sont très prometteurs pour la mise au point de traitements non invasifs et ciblés contre le cancer, ce qui, en fin de compte, améliore les résultats pour les patients [3]. L'incorporation d'éléments de terres rares dans les RENPs est essentielle pour obtenir une luminescence de upconversion efficace [8]. Le Néodyme (Nd), un élément des terres rares, est particulièrement remarquable pour ses fortes capacités d'absorption du NIR [9]. Le dopage des RENPs avec du néodyme peut améliorer considérablement leurs propriétés luminescentes, ce qui les rend très appropriés pour des applications dans l'imagerie et la thérapie des tissus profonds. Cependant, l'atteinte de concentrations élevées de dopage, telles que 60% de néodyme, tout en maintenant le contrôle sur la morphologie des nanoparticules, présente des défis importants [3].

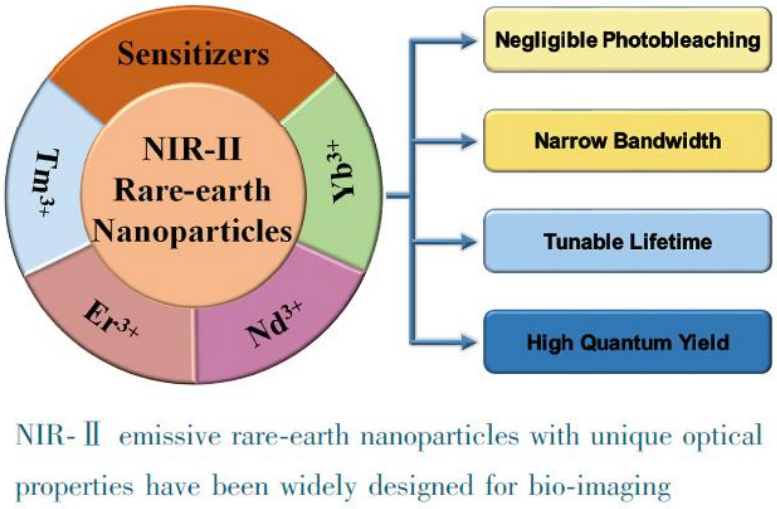

Figure 1.1 Proprietes et application des RENPs

Divers mécanismes pour la luminescence ont été identifiés, se produisant souvent seul ou en combination. Trois mécanismes fondamentaux sont 1. Absorption excitée de l'état (ESA), 2. avalanche de photons (PA), et 3. transfert d'énergie upconversion (ETU) (Absorption de l'état excité (ESA). Absorption de l'état excité (ESA) L'ESA (Energy State Absorption) implique un processus d'excitation en plusieurs étapes où plusieurs photons sont absorbés séquentiellement, à partir de l'état sol jusqu'à un stade de réservoir intermédiaire, et finalement atteindre un état excité. À partir de cet état excité, la luminescence se produit. Avalanche de photons (PA) Le processus PA (Photon Avalanche) est plus complexe et peut être caractérisé par trois comportements non linéaires distincts : la transmission, l'émission et le temps de montée, qui dépendent tous de l'intensité de puissance de la pompe et impliquent généralement un seuil de pompe critique. Par exemple, dans un système à quatre énergies, les états E0, E1 et E2 représentent l'état fond, les états intermédiaires et les états excités supérieurs, respectivement.

Mecanisme de transfert d'energie dans les nanoparticules de terres rares dopées (RENPS)

Nd^{3+} les nanoparticules de terres rares dopées aux ions Néodymes (Nd^{3+}), qui peuvent être excitées avec un laser 808 nm, ont attiré une attention significative en raison de leur compatibilité avec les applications biomédicales. Nd^{3+} a une grande section efficace d'absorption d'environ $1{,}2\times10^{-19}cm^2$, ce qui est dix fois plus élevé que celui de Yb^{3+} [52, 53]. Il est important de noter que Nd^{3+} a une absorption élevée de la lumière NIR autour de 808 nm, ou l'absorption d'eau est 20 fois inferieure à celle des ions Yb^{3+}. [54] bien que Nd^{3+} ait une longueur d'onde d'excitation dans la première fenêtre biologique (650-900 nm), ce qui est idéal pour les applications biologiques, les bandes d'émission résultantes dans la première (650-1000 nm) et la seconde

(1000-1350 nm) fenêtres biologiques limitent le transfert d'énergie directe des ions Nd^{3+} aux ions émetteurs, entravant une upconversion efficace.

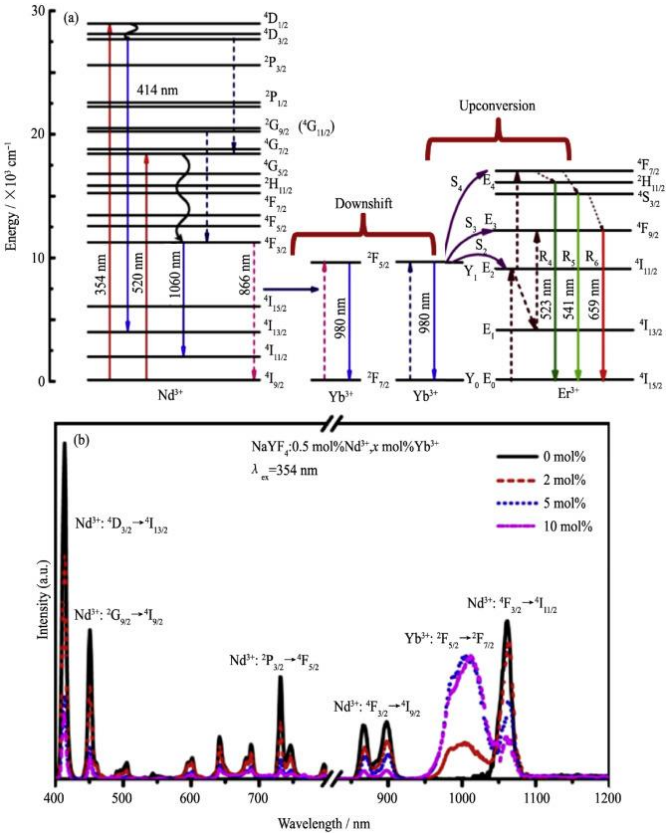

Fig 1.2 (a) Illustration schématique du diagramme des processus de transfert d'énergie et des transitions correspondantes du couple Nd^{3+} à Yb^{3+} (rétrogradation) et des transitions de Yb^{3+} à Er^{3+} (upconversion) ; (b) Spectres d'émission de $NaYF_4$:0.5 mol%Nd^{3+}, x mol%Yb^{3+} (où x 0, 2, 5, et 10) dans la région visible (gauche) et NIR (droite) sous l'excitation de 354 nanomètre

Cependant, le codage des ions Yb^{3+} en tant que pont entre les ions Nd^{3+} et les ions émetteurs dans les nanoparticules de terres rare améliore l'efficacité du transfert d'énergie de Nd^{3+} aux ions émetteurs. Cette approche réduit également considérablement les effets de surchauffe et améliore la profondeur de pénétration du laser. [55] Dans les nanoparticules co-dopees Nd^{3+}/Yb^{3+}, Nd^{3+} absorbe les photons du laser 808nm et transfère l'énergie aux ions Yb^{3+}. En conséquence, les ions Yb^{3+} sont excites et transfèrent ensuite de l'énergie aux activateurs ou aux émetteurs. Il existe différentes méthodes pour calculer l'efficacité du transfert d'énergie (η) entre le donneur d'énergie et l'accepteur d'énergie. Ces intensités peuvent être mesurées sous irradiation laser 808nm et 980nm pour le transfert d'énergie des ions Nd^{3+} aux ions Yb^{3+}, et des

ions Yb^{3+} aux ions émetteurs, respectivement. L'efficacité du transfert d'énergie des ions Nd^{3+} vers les ions Yb^{3+} a été rapportée à environ 70%[56].

Morphologie des nanoparticules de terres rares (RENPs) fortement dopées les nanoparticules sensibilises par Nd^{3+}-sensibilise sont très recherches pour les applications biomédicales, telles que l'imagerie des tissus profonds et la thérapie photodynamique, en raison de leur biocompatibilité accrue. Cependant, le rapport surface/volume élevé des nanoparticules upconversion de petite taille conduit souvent à de nombreux défauts de surface, ce qui peut augmenter la trempe de surface et réduire la luminescence de la conversion vers le haut. Le dopage d'ions métalliques dans n'importe quelle couche de nanoparticules de terres rares (RENPs) peut remplacer les ions lanthanide dans le cristal hôte, ce qui pourrait résoudre ces problèmes. Si l'ion lanthanide substitue et l'ion métallique dope ont des électrons de valence différents, ils induiront des déséquilibres de charge dans le réseau cristallin, provoquant la diffusion des ions crées à la surface des nanoparticules. Une fois que le processus de diffusion est saturé, il en résulte une couverture complète des nanoparticules, conduisant à une morphologie uniforme avec moins de défauts de surface et une intensité de luminescence de la reconversion améliorée [67].

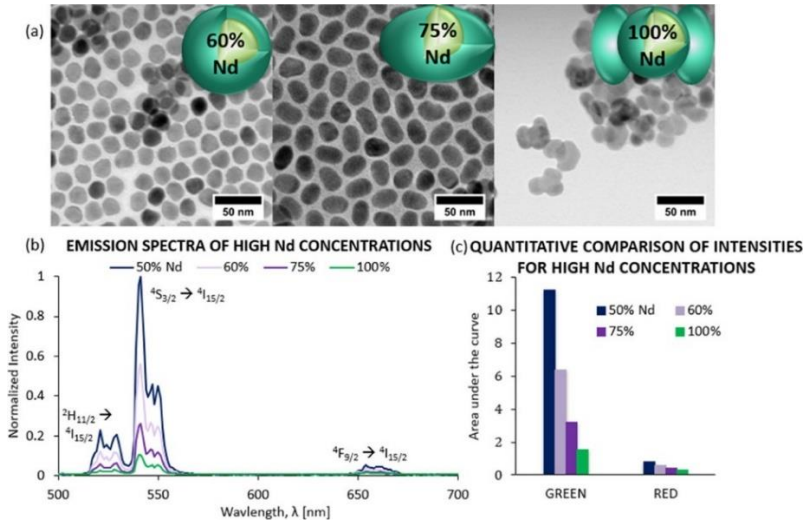

Figure 1.3 Effets des concentrations élevées de Nd^{3+} dans la coque. (a) Image TEM de $NaYF_4$:Yb/Gd/Er@$NaLuF_4$:60%Nd (gauche), @$NaLuF_4$:75%Nd (milieu) et @$NaNdF_4$ (à droite). b) Spectres d'émission de CS NPs dopés Er^{3+} de concentrations élevées de Nd obtenues au moyen d'un fluorimètre dont la source d'excitation est réglée à 0,6 W/cm^2 à 800 nm. c) Quantification de l'aire sous la courbe. Les émissions vertes comprennent des pics à 522 et 545 nm. L'émission rouge comprend un pic à 645 nm[1]

Dans ce contexte, zhang et al [2]. Fabriques ultra-petits, très émissifs Nd^{3+}-sensibilise upconversion nanoparticules dopées avec des ions Ca^{2+} ($NaGdF_4$, Tm, Ca@$NaYbf_4$@$NaNdF_4$, Ca) pour 808 nm de libération de médicaments actives par laser. Le dopage de 10mol% des ions Ca^{2+} dans toutes les couches des nanoparticules a entrainé des ucnps significativement petits avec une augmentation de trois fois l'intensité de la luminescence de la version upconversion par rapport aux nanoparticules sans Ca^{2+}. Cette amélioration est attribuée a une symétrie plus faible du champ cristallin autour de Yb^{3+} et Tm^{3+}, a une amélioration de la cristallinité des matériaux hôtes et a une réduction de la trempe de la surface en raison du remplacement des ions Gd^{3+} par des ions Ca^{2+} dans le cristal hôte ($NaGdF_4$), ce qui a induit des vacances. Ces postes vacants ont non seulement supprimé les défauts de surface, mais ont également améliore l'uniformité des nanoparticules.

Synthese des nanoparticules de terres rares (RENPs)

Pour atteindre une efficacité de luminescence élevée, il est essentiel de synthétiser des RENPs) de haute qualité. Il existe trois méthodes courantes pour synthétiser les RENPs : la décomposition thermique, la synthèse hydrothermale et la synthèse a base de liquides ioniques.

Méthode de décomposition thermique La décomposition thermique est l'une des méthodes les plus populaires, produisant des particules bien formées avec un bon contrôle de taille dans un temps de réaction relativement court. Cette méthode consiste généralement à dissoudre les précurseurs organiques dans des solvants organiques à haute ébullition à l'aide de tensioactifs. Les précurseurs organiques courants comprennent les composés du trifluoroacétate, tandis que les tensioactifs typiques ont des groupes de capsulage polaire et de longues chaînes hydrocarbonées, telles que l'acide oléique (OA), l'oléylamine (OM) et le 1-octadécène (ODE). [100] Mai et coll. ont systématiquement étudié le mécanisme de croissance des nanocristaux, identifiant une voie de nucléation retardée unique pour les précurseurs de trifluoroacétate dans des solutions de surfactants chauds. Le processus de synthèse est divisé en quatre étapes : la nucléation après un retard, la croissance des particules par l'approvisionnement en monomères, la réduction de la taille par dissolution et l'agrégation. La figure ci-dessous illustre la synthèse de nanoparticules des terres rare à base de lanthanide.

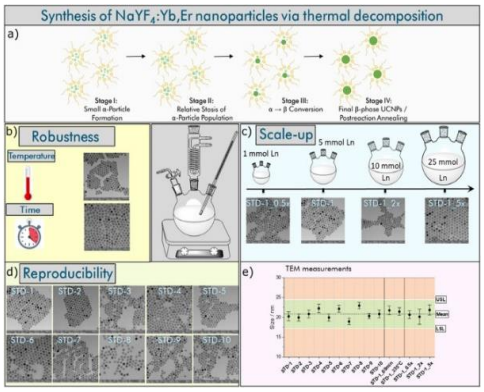

Figure 2.2 (a) illustration schématique de la formation et de la croissance des RENPs par la methode de décomposition thermique selon refs[101, 102]. Le précurseur ln se décompose thermiquement a une température plus élevée pour produire initialement de petites particules cubiques α, qui sont ensuite transformées en plus grandes particules hexagonales β-phase thermodynamiquement favorisées via un processus de dissolution-recristallisation thermodynamiquement entraine. B-e) reproductibilité, robustesse et évolutivité a la hausse de la procédure synthétique de base qui donne 20 nm β-Yb, Er-co-dope $NaYF_4$ RENPs. Images tem des RENPs obtenues à partir (b) d'une réaction réalisée avec une température accrue (335 °c au lieu de 325 °c) et un temps de réaction prolonge (60 minutes au lieu de 30 minutes) ; c) différentes tailles de lots (précurseurs d'1 à 25 mm d'er) pour évaluer la robustesse de la synthèse, et d) dix réactions indépendantes effectuées dans les mêmes conditions de reaction (std 1–std 10) pour explorer la reproductibilité de la synthèse. E) répartition par taille des ucnps obtenus, telle que déterminée par TEM.

Application Biologique de Nd^{3+}

En raison de leurs propriétés distinctives, y compris les effets de surchauffe minimisent et l'amélioration de la profondeur de pénétration, les nanoparticules de terres rares (RENPs) sensibilisées au Nd^{3+}- montrent une promesse significative pour des applications pratiques, en particulier dans les domaines biologiques. Ces applications comprennent la détection tissulaire, l'imagerie et le traitement du cancer. Cette section explorera les utilisations des RENPs Nd^{3+}-sensibilises, en se concentrant sur leurs rôles dans la photoluminescence vers le bas / conversion vers le haut pour la bioimagerie, la microscopie à haute résolution, l'imagerie des tissus profonds, et le diagnostic et la thérapie des tumeurs.

Application dans le traitement du cancer :

Le cancer est devenu la principale cause de décès dans le monde, posant un obstacle important à l'augmentation de l'espérance de vie et devrait être la principale cause de décès prématurés (avant l'âge de 70 ans) à l'échelle mondiale au cours de ce siècle [170]. Selon le Centre international de recherche sur le cancer, près de 10 millions de personnes sont mortes du cancer

en 2020, ce qui représente près d'un décès sur six. On estime que le fardeau mondial de cancer atteindra 28,4 millions de cas d'ici 2040, soit une augmentation de 47 % par rapport à 2020[170], et on prévoit qu'il double d'ici 2070 selon les tendances récentes [171]. Le traitement photothermique (PT) moderne a été utilisé pour le traitement du cancer depuis peu de temps après les essais sur le décollement de la rétine dans les années 1960 [172]. Dans les premiers stades, les lasers ont été directement utilisés pour enlever thermiquement le tissu tumoral par chauffage induit par irradiation [173, 174], un processus connu sous le nom de thérapie thermique du cancer (TT) [175], qui est considéré comme un précurseur de la thérapie photothermique du cancer (PTT) [172]. Cependant, le TT de cancer basé au laser a fait face aux limitations significatives, telles que viser avec précision les cellules malignes pour chauffer sélectivement la tumeur sans affecter les tissus sains environnants, la profondeur limitée de pénétration de laser, et l'interférence des substances endogènes comme les chromophores ou l'eau. De plus, la densité de puissance élevée du laser a soulevé des préoccupations en matière de sécurité [172, 176]. Pour résoudre ces problèmes et améliorer l'efficacité de la PT cancéreuse, l'utilisation d'agents photosensibles exogènes a été introduite [44, 177-179]. Ces agents absorbent l'énergie lumineuse et la convertissent en une autre forme d'énergie pour des effets thérapeutiques, réduisant ainsi la densité de puissance requise de la source lumineuse. Le ciblage et la sélectivité du traitement peuvent également être améliorés si les agents photosensibles fournissent des conseils d'imagerie. Selon les fonctions et les voies de traitement des agents, la PTOG du cancer comprend principalement la thérapie photothermique (PTT)[180, 181] et la thérapie photodynamique (PDT) [182, 183]. Les thérapies à base de lumière sont utilisées depuis plus de 3000 ans dans diverses cultures, notamment l'Égypte ancienne, l'Inde et la Chine [184, 185]. Un développement significatif s'est produit il y a plus de 100 ans quand Oscar Raab, un étudiant allemand en médecine, a découvert qu'une combinaison de lumière et d'acridine pourrait induire la mort cellulaire, un phénomène plus tard appelé « action photodynamique»[186]. La thérapie photodynamique (TPD), qui met à profit ce principe, a été officiellement approuvée en 1993 au Canada, en utilisant la photofrine comme photosensibilisant pour le traitement du cancer de la vessie. La TPD comporte trois composantes clés : la lumière, un photosensibilisant et l'oxygène. Le processus commence avec le photosensibilisant étant excité de son état de fond à un état excité sous des longueurs d'onde spécifiques de la lumière. Lorsque le photosensibilisant revient à son état sol, l'énergie libérée est transférée aux molécules d'oxygène voisines, générant des espèces réactives de l'oxygène (ROS) comme l'oxygène sice (O_2). Ces ROS peuvent induire des dommages oxydatifs aux cellules adjacentes, conduisant finalement à la mort cellulaire [187, 188].

Nanothermométrie

La température est l'une des fonctions d'état les plus essentielles largement utilisées et étudiées paramètre thermodynamique [243, 244]. Une augmentation de la température peut accélérer de nombreuses réactions chimiques, ainsi que des processus biologiques et physiques, à la fois dans la nature et dans des conditions de laboratoire. Cela rend la surveillance précise et précise de la température cruciale dans diverses applications industrielles, scientifiques, environnementales et biologiques [210, 245, 246]. Ceci est particulièrement important dans la biomédecine moderne, où la régulation continue et en ligne de la température est utilisée dans le diagnostic médical, le traitement des maladies et les soins de santé généraux [247-249]. La mesure de la température a été accomplie de diverses manières au cours des siècles. Aujourd'hui, les thermomètres les plus courants fonctionnent en utilisant : (I) des solvants liquides ou du mercure, qui reposent sur des propriétés de dilatation thermique ; II) l'effet thermoélectrique dans les thermocouples ; III) thermomètres à résistance qui mesurent les changements de résistivité électrique avec la température ; et (IV) les pyromètres, qui détectent le rayonnement infrarouge émis par un objet et le mettent en corrélation avec la température [243, 244, 250]. Cependant, la plupart de ces méthodes nécessitent une connexion physique ou électrique avec l'objet mesuré, ce qui complique la détection de la température à distance ou non invasive, comme dans le corps humain, à l'intérieur de systèmes mécaniques fermés ou dans des zones microscopiques ou à l'échelle nanométrique [243, 244, 250]. Les pyromètres, bien qu'ils n'aient pas besoin d'un contact direct, ne mesurent que la température de surface et sont généralement moins précis avec une résolution spatiale plus faible, ne fournissant souvent que des estimations de température approximatives pour les objets plus grands [243-245]. Les défis associés aux méthodes traditionnelles peuvent être relevés grâce à la (nano)thermométrie par luminescence, une technique qui permet la détection de température à distance et non invasive en surveillant les changements induits par la température dans certaines propriétés de luminescence des sondes optiquement actives. Cette technique permet la surveillance de la température dans des zones microscopiques et à l'échelle nanométrique [216, 250-254] en utilisant des caractéristiques spectroscopiques à l'état stable ou à résolution temporelle dépendantes de la température. Ces caractéristiques comprennent le rapport d'intensité de luminescence/fluorescence (LIR/FIR), l'intensité du signal, la position spectrale de la raie d'émission, la pleine largeur à la moitié maximale (FWHM) de la bande, ou les temps de désintégration/montée de la luminescence [216, 235, 250-252, 255-257]. Chacun de ces facteurs peut être utilisé comme « paramètre thermométrique », qui peut être étalonné pour être corrélé avec la température du système [235, 250, 256]. Les paramètres thermométriques les plus utilisés sont le LIR/FIR et le temps de

désintégration des émissions. Bien que le LIR/FIR soit relativement facile à surveiller à l'aide de systèmes de détection standard, il peut être influencé par les effets de réabsorption/diffusion et les variations de la densité de puissance d'excitation sur la cible lors de mesures du système réel, telles que les expériences in vitro ou in vivo [250, 258, 259]. En revanche, le temps de désintégration des émissions est moins affecté par ces facteurs et peut fournir des lectures de température précises dans divers environnements, bien qu'il nécessite

Objectifs et contribution de la thèse la réalisation d'une excitation de longueur d'onde biobenign est possible en introduisant le Néodyme (Nd^{3+}) dans les nanoparticules de terres rares (RENPs) dopées d'Ytterbium (Yb^{3+}). Le Néodyme (Nd^{3+}) est un dopant efficace en raison de sa forte absorption dans la région NIR, de sa pénétration des tissus profonds, de sa réduction de l'autofluorescence et de sa grande application en thérapie photothermique et photodynamique d'où son utilisation dans ce projet. En utilisant le Néodyme (Nd^{3+}) avec Ytterbium (Yb^{3+}) dans les RENPs à base de lanthanide, il est possible de déplacer l'absorption de 980nm a 800nm, une gamme ou l'eau n'absorbe pas la lumière. Des concentrations élevées de Nd^{3+} sont avantageuses car elles améliorent à la fois l'absorption et l'émission. Dans la thérapie de cancer, RENPs fortement dope peut convertir efficacement la lumière de NIR en lumière visible, activant des photosensibilisants pour générer des espèces réactivées de l'oxygène (ROS) qui tuent des cellules cancéreuses. L'émission améliorée et les capacités fonctionnelles de ces RENPs fortement dopes cible le traitement efficace des tissus cancéreux tout en réduisant les dommages aux cellules saines qui est ce que nous voulons réaliser. D'après l'examen de la littérature, la majorité des travaux publies portaient sur des niveaux de dopage inferieurs a 10 mol%, quelques études rapportant jusqu'à 30 mol% [4-7]. La difficulté d'obtenir une bonne morphologie pour les nanoparticules de terres rares (RENPs) fortement dopées (RENPs) est due à l'augmentation des taux de nucléation / croissance, des souches / défauts de réseau, de la distribution non homogène des dopants et de la sensibilité a la température. Cela a entrainé une forme et des tailles non uniformes qui, en retour, affectent son application dans le traitement du cancer, entre autres. Par conséquent, les objectifs de mes thèses sont énoncés ci-dessous :

1. Procédure de synthèse optimisée dans la première partie de ce projet, nous nous sommes concentres sur la conception et la synthèse optimisée de nanoparticules des terres rare $LiYbF_4:Nd^{3+}$ (60%) 2.5 mmol fortement dopées. L'objectif est d'obtenir une bonne morphologie pour les nanoparticules des terres rare fortement dopées en optimisant différents paramètres tels que le temps de réaction, la température et la concentration des ligands utilises pour leur application dans le traitement du cancer. Une

bonne morphologie améliore l'efficacité de luminescence et le traitement efficace des tissus cancéreux tout en minimisant les dommages aux cellules saines.

2. Propriétés optiques améliorées pour la détection de température non invasive en allant plus loin, j'ai essayé d'améliorer l'efficacité de la version luminescence en créant une structure de coque noyau / inerte qui est composée d'aucun dopant dans la coque du $LiYbF_4 : Nd^{3+}@LiYF_4$ fortement dope (60%). L'objectif est de réduire les défauts de surface et les impuretés, d'améliorer le transfert d'énergie entre les ions sensibilisants et activateurs tout en réduisant la trempe de la concentration pour améliorer l'efficacité globale de la luminescence. Une approche de synthèses optimisée a été utilisée pour contrôler la morphologie.

Organisation des thèses il y a cinq parties de ces thèses, et l'organisation est décrite ci-dessous :
Chapitre 1 : présente le contexte de l'étude, les problèmes de recherche, les buts de motivation et les objectifs de ce travail le
Chapitre 2 : décrit les matériaux utilisés dans la synthèse et les propriétés de luminescence du noyau $LiYbF_4: Nd^{3+}$ (60 mol%)2.5 mmol et $LiYbF_4@LiYF_4$(2 mmol).
Chapitre 3 : traite des détails expérimentaux de la méthode de synthèse utilisée (méthode de décomposition thermique par injection à chaud), des techniques de stabilisation et des résultats obtenus pour le noyau $LiYbF_4$(60% Nd) 2.5 mmol. Il discute également des détails expérimentaux de l'optimisation des propriétés de luminescence en créant une structure noyau-coque $LiYbF_4@LiYF_4$ (2 mmol), la stabilisation et les résultats obtenus.
Chapitre 4 : traite des résultats obtenus à partir des propriétés de caractérisation et de luminescence.
Chapitre 5 : résume brièvement les conclusions de ce travail, son application, ses défis et ses perspectives.

Chapitre 2

Matériaux et caractérisation

Dans ce chapitre, nous mettrons en évidence la méthode de synthèse générale utilisée pour synthétiser $LiYbF_4$ (60% Nd) 2.5 mmol et $LiYbF_4@LiYF_4$ et la technique de caractérisation utilisée. Matériaux : Y_2O_3 (reacton, 99.999%), Yb_2O_3 (reacton, 99.998%), Tm_2O_3 (reacton, 99.997%), Nd_2O_3 (reacton, 99.997%) acide trifluoroacetique (99%), 1-octadecene (ODE, 90%), et l'acide oléique (OA, 90%) ont été achetés auprès d'alfa aéras (états-unis). Le trifluoroacetate de Lithium

(98%) et l'oleylamine (OM, 70%) ont été obtenus de sigma-aldrich (etats-unis). Tous les produits chimiques ont été utilisés tels qu'ils ont été reçus.

Chapitre 3

Méthodologie

Core et Shell $LiYbF_4$: Nd^{3+} (60% and 2%) 2.5 mmol

1. Préparation des précurseurs.
2. Synthèse a taille contrôlée de $LiYbF_4$: Nd^{3+} RENPs
3. Synthèse de $LiYbF_4$: Nd^{3+} Coré. RENPs par l'intermédiaire de la méthode d'injection à chaud
4. Stabilisation de $LiREF_4$:RE^{3+} Coré

Synthèse de Coré/Shell $LiYbF_4$: $Nd^{3+}/LiYF_4$

Les RENPs de noyau/coquille ont été synthétisés en développant épitaxialement la couche de coquille, avec les précurseurs appropriés injectés dans la solution de noyau préformée utilisant un système de pompe-seringue. La solution A à été préparée dans une fiole de 100 mL en dissolvant 0.5 mol de matériau de base dans une solution d'OA/ODE, avec des volumes égaux d'OA et d'ODE représentant un total de 20 mL. La solution B se composait de 2mol de précurseurs de coque mélangés à 10 mL d'OA et à 10 mL d'ODE. Les deux solutions ont été agitées et dégazées sous vide à 110 °C pendant 30 min. Dans une atmosphère Ar, la température de la solution A à été augmentée à 315 °C, et 7ml de solution B ont été injectés à un taux de 1.5 mL/min à un intervalle de temps de 40 min. Une fois l'injection terminée, les étapes suivantes - refroidissement, lavage et stockage - ont suivi les procédures décrites précédemment.

Chapitre 4

Résultat et discussion

D'après l'examen de la littérature, nous pouvons voir que l'augmentation de la température et du temps de réaction des nanoparticules de terres rares fortement dopées (RENPs) peut entraîner des nanoparticules uniformément formées et uniformément réparties. Il a également été observé que la création d'une structure noyau /coquille aide à augmenter la luminescence et son application dans le traitement du cancer. Caractérisation morphologique du noyau $LiYbF_4$: Nd^{3+} La formation image de TEM a été employée pour vérifier la morphologie du noyau $LiYbF_4$: Nd^{3+}(60%) RENPs. Le diamètre du noyau varie entre 25 nm-29 nm. Nous pouvons voir que les particules sont uniformément réparties avec une structure hexagonale. Les images TEM et le graphique de distribution des tailles peuvent être vus dans la figure ci-dessous.

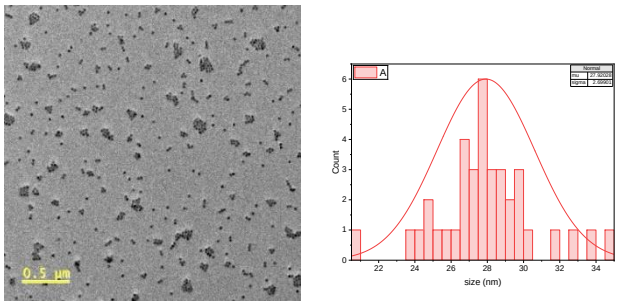

Figure 4.1 Image TEM de $LiYbF_4$: Nd^{3+} (60%) et graphique de distribution de taille

Caractérisation morphologique du noyau/coquille $LiYbF_4$: Nd^{3+}@$LiYF_4$

La formation image de TEM a été employée pour vérifier la morphologie du noyau/coquille $LiYbF_4$:Nd^{3+}@$LiYF_4$ RENPs. Le diamètre du noyau varie entre 31 nm-35 nm. La croissance de la coquille est d'environ 2nm-5nm. Nous pouvons voir que les particules sont uniformément réparties avec une structure hexagonale. Les images TEM et le graphique de distribution des tailles peuvent être vus dans la figure ci-dessous.

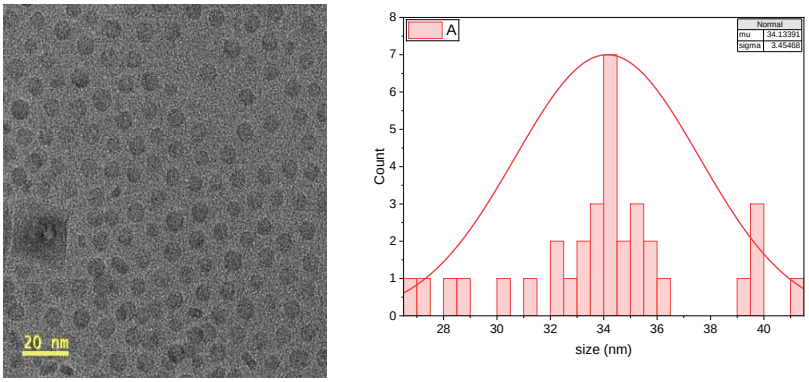

Figure 4.2 Image TEM et graphique de distribution de taille

Caractérisation optique du Noyau/coque $LiYbF_4$: Nd^{3+}@$LiYF_4$ (60% et 2% Nd)

Nous avons caractérisé les propriétés d'émission du CS tel que synthétise pour évaluer l'effet de Nd^{3+} fortement dope. L'émission de photoluminescence de RENPs dans la gamme spectrale de 400 nm-1100 nm a été mesurée sous excitation 808 nm les niveaux habituels de dopant sensibilisant sont maintenus en dessous de 30% mol car cela pourrait affecter l'efficacité du transfert d'énergie et la relaxation croisée. Par l'intermédiaire de plusieurs étapes d'etu qui a été expliqué précédemment, nous avons remarqué plusieurs émission d'uc une fois irradie avec 800nm, $LiYbF_4$: Nd^{3+}@$LiYF_4$ (60%), il y avait un profil d'émission couvrant des gammes

spectrales d'environ 400nm-700nm. Des émissions of Nd^{3+} ont été remarquées autour de Les bandes d'émission en décroissance sont observées à environ 920 nm, 1050 nm et 1100 nm, correspondant aux transitions des états excités $^4F_{3/2}$ vers les sous-niveaux de Stark des multiplets $^4I_{9/2}$ et $^4I_{11/2}$

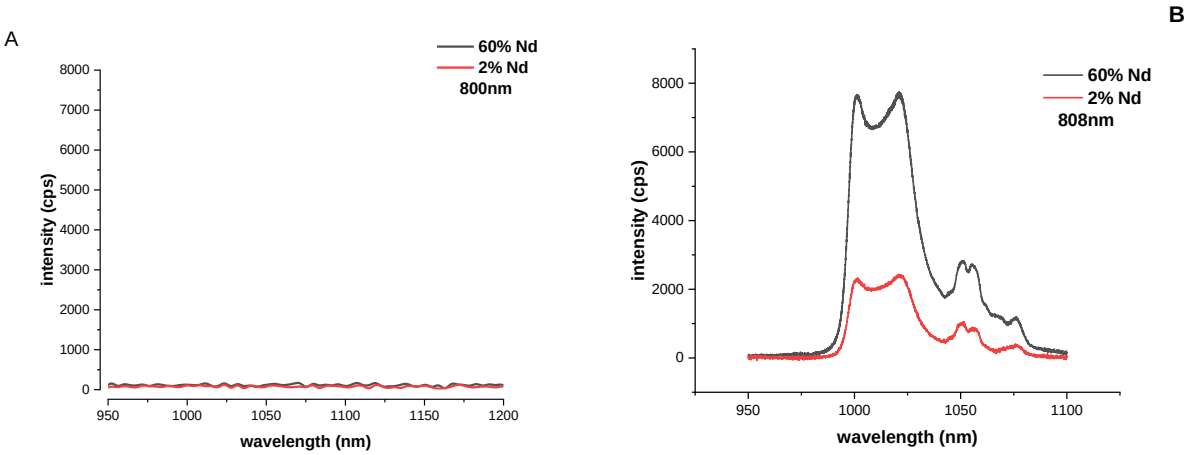

Figure 4.3 Rétrogradation spectrale des émissions de $LiYbF_4:Nd^{3+}@LiYF_4$ à 808 nm et ~140W/cm² et rétrogradation spectrale des émissions émission spectrale de noyau / enveloppe de cœur de Nd^{3+}.

Nanothermométrie

Indépendamment de l'imagerie NIR, les émissions de DS peuvent spectralement donner des informations sur les températures qui peuvent être extraites en même temps que nous avons discuté dans la revue de littérature. Cela permettra une surveillance de la température en temps réel tout en essayant d'éviter la surchauffe et les dommages aux tissus. Un support de cuvette à température contrôlée a été utilisé pour surveiller le changement de température. À différentes températures, il a été observé que l'intensité de Nd^{3+} est presque restée presque constante avec quelques changements d'intensité (Figure 4.3). Nous avons également calculé le rapport d'intensité luminescente (LIR) Δ entre les 2 composantes austères. Δ (= I1(1000.7-1015.5 nm)/ I2 (1019.9 nm-1022.6 nm) les plages d'intégration ont été utilisées pour tracer le paramètre thermométrique Δ en fonction de la température. La bande d'émission Nd^{3+} a montré une sensibilité thermique élevée autour de 1040 nm, ce qui le rend adapté à la thermométrie de photoluminescence à distance. Le LIR Δ a montré une progression linéaire lorsqu'il est représenté par rapport au changement de température dans la gamme de 25-45 ^oC à une augmentation de la température de 5 ^oC. (Figure 4.4B)

On peut observer que la sensibilité thermique relative diminue légèrement à mesure que la température augmente. L'échantillon de noyau / coque $LiYbF_4$: $Nd^{3+}@LiYF_4$ était excité à une

longueur d'onde d'excitation de 808 nm pendant 50 min, et la température était surveillée à l'aide d'une caméra thermique. Il a été observé qu'aucun changement de température de l'échantillon n'a été enregistré même après 50 min. Cela pourrait signifier que le rayonnement émis par l'échantillon ne change pas avec la température. En outre, nous avons vérifié le changement dans le spectral rétrograde sous une irradiation laser continue pendant 20 min, aucun changement n'a été remarqué sur l'échantillon.

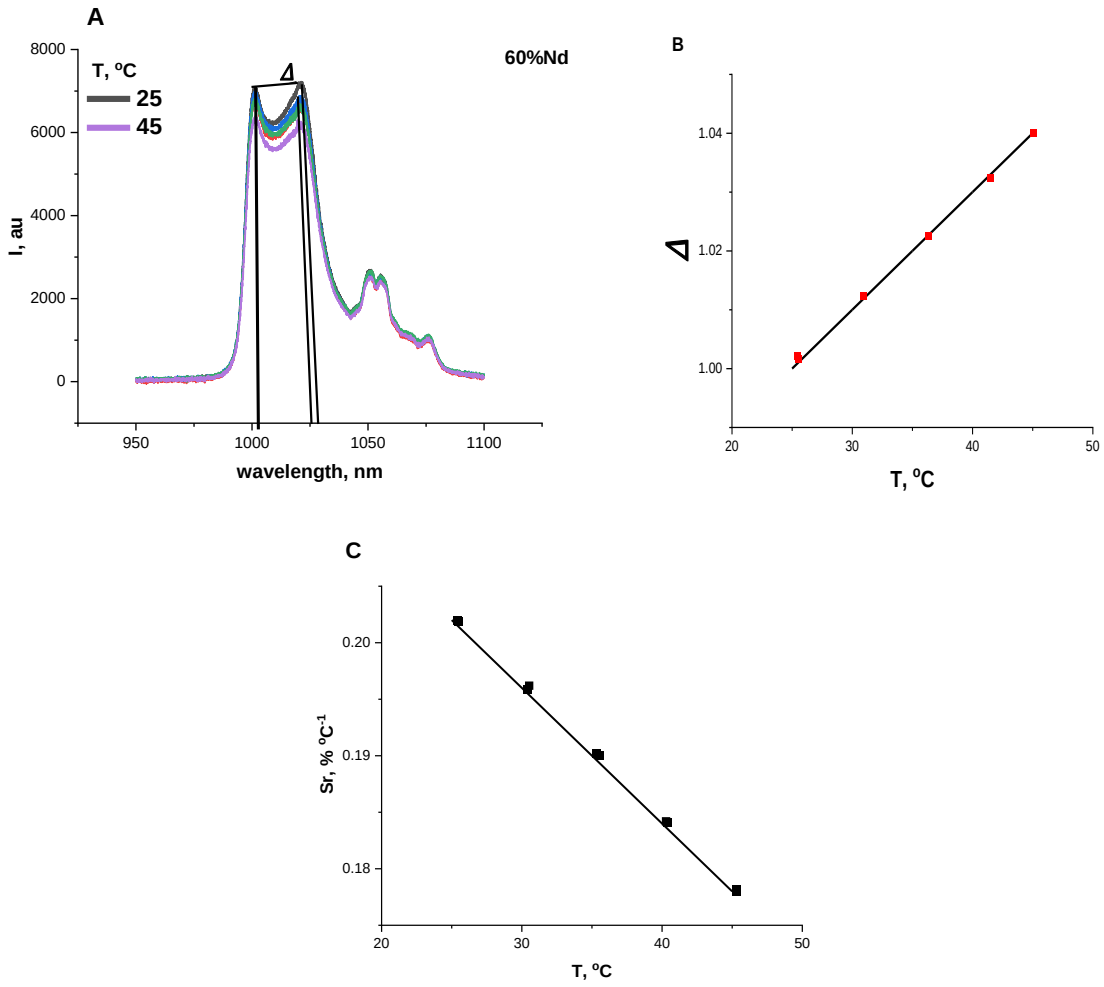

Figure 4.4 A- Luminescence descendante spectres d'emission de Nd^{3+} renps sous l'excitation 808 nm. Les valeurs sous la courbe sont utilisees pour calculer le parametre thermometrique lir δ. B- graphique du parametre thermometrique lir δ par rapport a la temperature. C- sensibilite relative a la temperature (Sr) en fonction de la temperature.

Chapitre 5

Conclusion

En résumé, nous avons réalisé la synthèse contrôlée de nanoparticules de terres rares (RENPs) fortement dopées $LiYbF_4$: Nd^{3+} (60 mol%) en optimisant différents paramètres pouvant influencer la contrainte du réseau cristallin. Nous avons également amélioré les propriétés optiques et réduit l'extinction de surface en concevant une structure cœur/coquille inerte $LiYbF_4$: Nd^{3+}@$LiYF_4$. Nous avons déterminé qu'en augmentant le temps de réaction à plus de 2 h, en abaissant la température de réaction de 330 °C à 315 °C et en contrôlant la concentration, il était possible d'obtenir des RENPs uniformes et bien dispersées. Ces particules uniformes sont cruciales pour des applications en thérapie photothermique (PTT) ou photodynamique (PDT) contre le cancer, car des nanoparticules de tailles différentes peuvent se comporter différemment dans l'organisme. Ainsi, une monodispersibilité est essentielle pour envisager des applications biomédicales futures.

De plus, nous avons étudié les propriétés de photoluminescence des RENPs $LiYbF_4$: Nd^{3+}@$LiYF_4$. Le spectre de photoluminescence de décalage vers le bas des RENPs dopées Nd^{3+} sous une excitation à 808 nm a révélé des pics d'émission distincts à environ 920 nm, 1050 nm et 1100 nm, le pic dominant étant situé autour de 1050 nm. Ce fort pic d'émission dans le proche infrarouge (NIR) rend les RENPs adaptées à des applications d'imagerie biomédicale et de capteurs optiques. Le spectre de photoluminescence par conversion ascendante montre une forte émission verte autour de 530 nm et 550 nm, des émissions rouges dans la plage de 660 à 670 nm, ainsi que des pics mineurs dans la région bleue autour de 450 nm. Les émissions dominantes dans le vert et le rouge témoignent d'une conversion ascendante efficace. Ces émissions sont idéales pour les applications biomédicales en raison de leur profondeur de pénétration dans les tissus biologiques. Le rapport d'intensité de luminescence (LIR) obtenu à partir de mesures de nanothermométrie a montré une progression linéaire avec l'augmentation de la température, démontrant que ces RENPs peuvent être utilisées comme capteurs de température. Cependant, la sensibilité relative (Sr) diminue à mesure que la température augmente, ce qui peut être attribué aux effets d'extinction thermique, couramment observés dans les RENPs. Les RENPs $LiYbF_4$: Nd^{3+}@$LiYF_4$ montrent ainsi un potentiel significatif pour des applications biomédicales sensibles à la température.

TABLE OF CONTENT

LISTE DES FIGURES

LIST OF TABLES

LIST OF ÉQUATIONS

LISTE DES ABRÉVIATIONS

RENPs……RARE-EARTH NANOPARTICLES

DS……DOWNSHIFTING

NIR……..NEAR INFRARED

Nd……NEODYMIUM

PDT……PHOTODYNAMIC THERAPY

PTT……PHOTOTHERMAL THERAPY

OA……OLEIC ACID

OM……OLYEAMINE

ODE……OCTADECENE

TEM……...TRANSMISSION ELECTRON MICROSCOPY

PL……..PHOTOLUMINESCENCE

ESA……...EXCITED STATE ABSORPTION

PA……PHOTON AVALANCHE

ETU……ENERGY TRANSFER UPCONVERSION

Ln……LANTHANIDE

RE……..RARE EARTH

REF……...RARE-EARTH FLOURIDES

AREF……..ALKALI RARE-EARTH FLOURIDES

QD……..QUANTUM DOT

UCN……...UPCONVERSION NANOMATERIAL

UCNs……...UPCONVERSION NANOMATERIALS

UV……ULTRAVIOLET

S……..SENSITIZER

A……ACTIVATOR

NC……NANOCARRIERS

AA……...ACRYLIC ACID

RES……RETICULOENDOTHELIAL SYSTEMS

BBB……...BLOOD BRAIN BARRIER

DLS……...DYNAMIC LIGHT SCATTERING

PS……..POLYSTYRENE

ROS……REACTIVE OXYGEN SPECIES

NPs……NANOPARTICLES

PA……PHOTOACOUSTIC

LSPR……LOCALIZED SURFACE PLASMON RESONANCE

PAI……..PHOTOACOUSTIC IMAGING

UC……...UPCONVERSION

CW……...CONTINUOUS-WAVE

FRET……..FÖRSTER RESONANCE ENERGY TRANSFER

TT……THERMAL THERAPY

PT……PHOTOTHERMAL

NHs……NANOHEATERS

NThs……NANOTHERMOMETERS

BWs……BIOLOGICAL WINDOWS

ET……ENERGY TRANSFER

D……DONOR

FWHMs……..FULL WIDTH AT HALF MAXIMUMS

DOX……DRUG DOXORUBICIN

TFA……TRIFLUOROACETIC ACID

HRTEM……..…HIGH RESOLUTION TRANSMISSION ELECTRON MICROSCOPY

MPM……MULTIPHOTON MICROSCOPY

NA……NUMERICAL APERTURE

IET……INTERFACIAL ENERGY TRANSFER

CS……CORE/SHELL

FIR……FLUORESCENCE INTENSITY RATIO

LIR…… LUMINESCENCE INTENSITY RATIO

I_1……INTENSITY OF LOWER BAND

I_2……INTENSITY OF HIGHER BAND

T……ABSOLUTE TEMPERATURE

K_B……BOLTZMANN CONSTANT

UCNPs……UPCONERSION NANOPARTICLES

XRD……X-RAY DIFFRACTION

SEM……SCANNING ELECTRON MICROSCOPE

EDX……ENERGY DISPERSIVE X-RAY

S_r ……THERMAL SENSITIVITY

RXN……REACTION

1 INTRODUCTION

1.1 Introduction to Nanotechnology in Biomedical Applications

1.1.1 Overview of nanotechnology impact on biomedical fields

Nanotechnology has had a profound impact on the biomedical sciences, introducing innovative tools for diagnostics, imaging, and therapy. Due to their diminutive size and distinctive properties, nanoparticles can interact with biological systems at the molecular level, opening unparalleled opportunities to enhance the effectiveness of medical treatments [1]. Researchers are exploring the potential of nanoparticles for targeted drug delivery, non-invasive imaging, and as therapeutic agents in cancer treatment [2]. An emerging approach involves using light to activate nanoparticles and the drugs they carry, offering a new avenue for non-invasive treatment of various diseases. Leveraging these unique optical properties enables targeted imaging and treatment of specific areas while minimizing exposure to unaffected parts of the body [3]. Among the various types of nanoparticles, rare-earth nanoparticles (RENPs) have garnered significant attention due to their ability to convert low-energy near-infrared (NIR) light into higher-energy visible or ultraviolet light [4]. This characteristic is particularly advantageous in biomedical applications, as NIR light can penetrate deeper into biological tissues with minimal photodamage [1]. RENPs have exhibited promise in improving the sensitivity and resolution of bioimaging techniques and enabling innovative therapeutic approaches [5]. Ongoing advancements in this field hold tremendous potential for the development of non-invasive and targeted cancer treatments, ultimately leading to improved patient outcomes [1]. The inclusion of rare earth elements in RENPs is crucial for achieving efficient upconversion/downshifting luminescence [6] . Neodymium (Nd), a notable rare earth element, is particularly valued for its strong NIR absorption capabilities [7] . Doping RENPs with Neodymium can significantly enhance their luminescent properties, making them highly suitable for applications in deep-tissue imaging and therapy. However, achieving high doping concentrations, such as 60% Neodymium, while maintaining control over the morphology of the nanoparticles, presents significant challenges [1].

1.2 Upconversion

Upconversion is a process in which lower-energy (longer wavelength) photons are converted into higher-energy (shorter wavelength) photons. This phenomenon is observed in specific materials called upconversion phosphors or upconversion nanoparticles [8]. These materials can absorb

two or more low-energy photons and then emit a single photon of higher energy. Upconversion can be seen in transition metals, actinides, but mostly in rare earth elements, which consist of the Lanthanide (Ln) series, yttrium, and scandium [9]. Ln^{3+} are made up of 4f, $5d_{0-1}$ inner shell configurations covered by outer shells, exhibiting abundant and distinctive energy-level structures. These materials display remarkable luminescence emissions through intra-4f or 4f-5d transitions. These exceptional luminescence properties, which are narrow bandwidth, long-time emission, and anti-Stokes shift, have been used extensively in lasers, optical imaging, photodynamic therapy, and solar cells. Anti-Stokes shift occurs when a thermally excited ground state is electronically excited, resulting in a shift of only a few kBT (25.7 mev). Achieving high luminescence efficiency is a challenge. From research, it is paramount to choose an appropriate host material with low phonon energy to achieve maximum upconversion efficiency. Presently, host materials, such as fluoride, chloride and bromide, have been shown to improve upconversion luminescence intensity. However, most chlorides and bromides are moisture-sensitive, making them unsuitable for labeling biomolecules often used in aqueous solutions [10]. Rare-earth fluorides, such as REF_3 and $AREF_4$ (A = alkali), are considered excellent host materials due to their high refractive index and low-energy phonons, which reduce the probability of nonradiative decay and increase luminescence quantum yield.

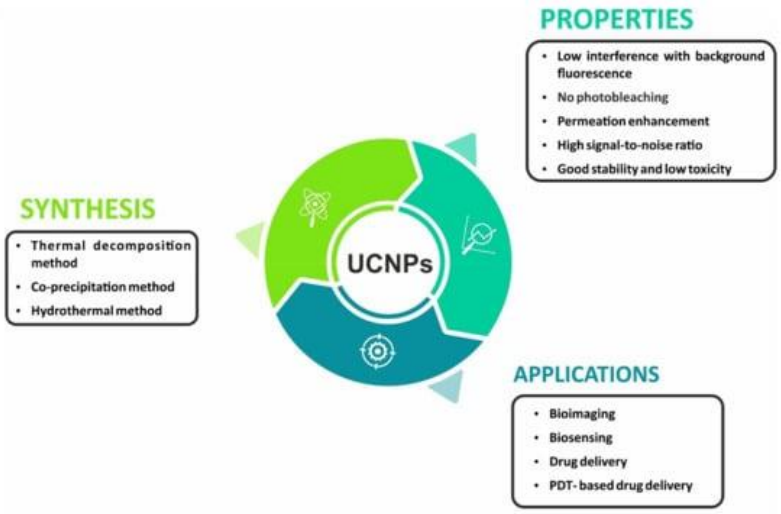

Figure 1.1 Synthesis, properties, and application of UCNPs

Figure 1.1 shows the synthesis, properties, and applications of UCNPs.

Most fluorescent materials, including dye molecules, quantum dots, and dye-doped silica/gold nanomaterials, emit light through a downshifting process, which involves emitting lower-energy

photons under higher-energy irradiation. Despite the significant progress made using conventional organic dye molecules/quantum dot (QD) based biomarkers in real-time detection and bioimaging, they still have notable drawbacks. These materials are typically excited by ultraviolet (UV) or visible light, which can cause autofluorescence and photodamage to biological samples, leading to a low signal-to-noise ratio and limited sensitivity. These issues have driven the development of upconversion nanomaterials (UCNs), which consist of an inorganic host doped with Ln^{3+} ions. UCNs exhibit good biocompatibility, generally low cytotoxicity, and are non-cytotoxic to a wide range of cell lines [11, 12]. Surface modification techniques such as ligand engineering [13-15], ligand attraction [16], surface polymerization [11, 17-21], self-assembly [22-24], and layer-by-layer assembly [25] have expanded their applications. Among these, surface modification with a silica shell is the most popular and practical approach [11, 19, 26-28]. This allows proteins, DNA, biological macromolecules, or other desirable targets to be easily linked to UCNs [29-31]. The ability of UCNs to emit visible light under NIR irradiation makes them ideal for both in vivo and in vitro bioimaging.

Theoretically, most lanthanide ions can undergo the NIR-to-visible upconversion process, but detectable upconversion is achievable only with a few trivalent lanthanide ions (e.g., Er^{3+} and Tm^{3+}) under low pump densities (980 nm excitation). Currently, the most used upconversion nanoparticles are Yb^{3+}-Er^{3+} or Yb^{3+}-Tm^{3+} co-doped $NaYF_4$/$LiYF_4$ nanomaterials ($NaYF_4$/$LiYF_4$+, Er^{3+} or $NaYF_4$/LiF_4, Nd^{3+}, Tm^{3+} UCNs).

1.2.1 Basic concepts of rare-earth nanoparticles (RENPs)

A photon is the smallest unit of light or other electromagnetic energy, carrying both energy and momentum [32]. The energy and momentum of a photon are determined by its wavelength (λ) according to the equation:

$$E=hc/\lambda \tag{1.1}$$

where h is Planck's constant, c is the speed of light, and λ is the wavelength.

Photons can be emitted through several natural processes, such as molecular, atomic, or nuclear transitions from higher to lower energy levels, resulting in a spectrum of photon energies from low (radio waves) to high (gamma rays). Photon upconversion is a specific mechanism of photon emission. In photon upconversion, nanoparticles absorb long-wavelength (low energy) NIR radiation and emit shorter-wavelength (higher-energy) radiation ranging from UV to infrared. This

process involves the sequential absorption of two or more photons, resulting in anti-Stokes emission [33, 34].

Rare-earth nanoparticles (RENPs) consist of three primary components: an inorganic crystalline host lattice and two types of lanthanides (Ln^{3+}) ions—sensitizers (donors) and activators (emitters). The properties of RENPs are heavily influenced by the host lattice and the doped lanthanide ions, which enable these nanoparticles to emit a broad spectrum from UV to NIR under NIR laser irradiation.

Ytterbium ion (Yb^{3+}) is the most used NIR photon energy harvester (sensitizer) in UCNPs. Its energy gap ($^2F_7/_2$ to $^2F_5/_2$) matches well with the energy levels of commonly used activators (Er^{3+}, Tm^{3+}, Ho^{3+}), resulting in efficient emission under 980 nm laser irradiation. However, Yb^{3+} has only one excited state energy level ($^2F_5/_2$) [35-37], leading to a single band absorption that limits the pumping wavelength to the 920-1050 nm range [38], peaking around 980 nm, coinciding with the absorption peak of water.

Since water is a major component of living tissues, this overlap poses challenges for using Yb^{3+} sensitized UCNPs in biomedical applications such as photodynamic therapy, photothermal therapy, bioimaging, and sensing, due to the risk of overheating and reduced laser penetration depth. To address these issues, efforts have been made to shift the excitation wavelength of RENPs from 980 nm to around 808 nm, significantly reducing water absorption[39]. One successful approach involves using Nd^{3+}-sensitized RENPs.

1.2.2 Properties and Composition of RENPs

The properties of RENPs can be tailored by using appropriate host-dopant combinations, core-shell nanostructures, and energy exchange with "alien species" like organic dyes and quantum dots [40].

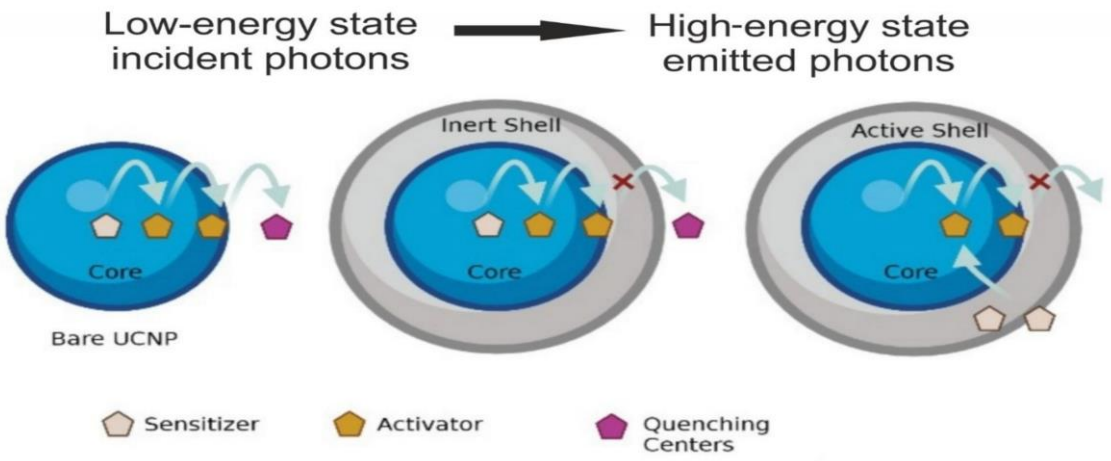

Figure 1.2 Structure of core-shell upconversion nanoparticles [41]

These versatile characteristics make RENPs an outstanding biomaterial for a variety of applications, including multimodal tumor imaging, drug delivery, cell labeling, sensing, photodynamic therapy (PDT), and photothermal therapy (PTT) [42-44]. The signal from RENPs can be accurately measured due to the direct relationship between particle number and signal intensity. Additionally, RENPs are well-suited for multiplexing because of their narrow emission band, allowing multiple colors to be displayed in a single image. Other notable features of RENPs include enhanced chemical and physical stability, low toxicity, and resistance to photobleaching.

For the Ln^{3+} ion(s) of interest, the multiphonon relaxation rate constant (k_{nr}) can be determined by the following relationship [45]:

$$k_{nr} = A \exp(-\alpha \nabla E / h\omega_{max}) \quad (1.2)$$

where ∇E represents the energy gap between a populated energy level and the next lower lying energy level of the Ln^{3+} species of interest, β is a constant that is dependent on the host material, and $h\omega_{max}$ represents the highest vibrational mode of the host lattice associated with the phonon energy of the host.

RENPs are composed of inorganic host molecules doped with rare earth (RE)-based lanthanides or actinides dopants integrated into the host lattice. Various dopants, such as transition metal ions like Ti^{2+}, Ni^{2+}, Mo^{3+}, Re^{4+}, or Os^{4+}, embedded in appropriate host molecules, exhibit photon upconversion. Among these, lanthanide-doped (Ln^{3+}) materials show the highest upconversion efficiencies at room temperature due to the electron transitions in the 4f subshell. Lanthanides,

ranging from lanthanum to lutetium, have their 4f energy levels filled, with valence electrons shielded from external interactions. Although all lanthanides can undergo upconversion, only erbium (III), holmium (III), and thulium (III) can absorb and transition to the visible and UV ranges, thanks to their inner shell electrons being shielded by the 5s and 5p subshells. This shielding results in numerous metastable energy states, facilitating upconversion. While a single lanthanide ion can produce the upconversion (UC) effect, co-doping is typically used to boost UC efficiency, as most lanthanide ions have low absorption cross-sections and weak emission[46]. Increasing the dopant concentration of lanthanide ions per nanocrystal can enhance absorption, but high concentrations can cause concentration quenching, leading to radiation-free deactivation and cross-relaxation processes, thus limiting the dopant quantity to below 2 mol% to prevent excitation energy loss is encouraged. Co-doping sensitizer ions with activator ions, matched closely in intermediate-excited states, is necessary to achieve high upconversion efficiency. These sensitizer ions facilitate efficient nonradiative energy transfer to activator ions, enhancing absorption [47, 48]. Yb^{3+} ions are commonly used as sensitizers for Er^{3+}, Tm^{3+}, or Ho^{3+} and Nd^{3+} doped UCNPs [49].

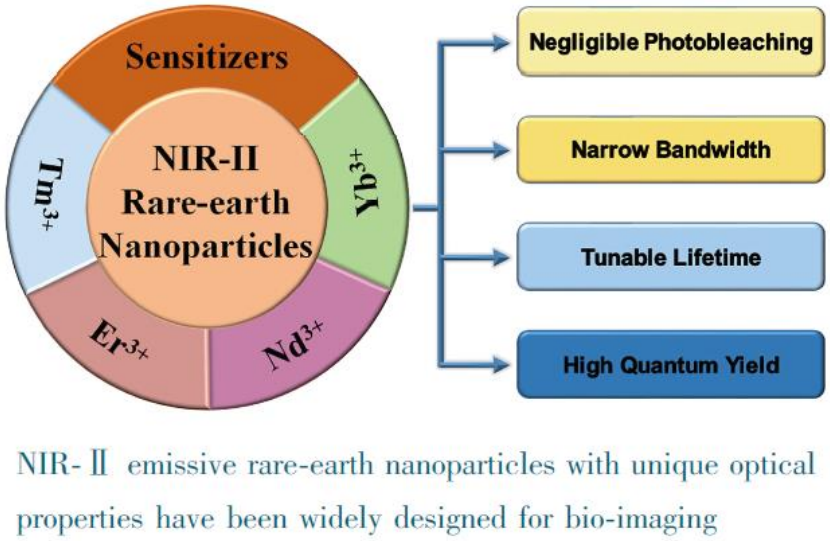

Figure 1.3 Components and optical properties of RENPs

Fig 1.3 describes the different sensitizers and optical properties best for RENPs. [41]

1.2.3 Mechanism

Various mechanisms for upconversion luminescence have been identified, often occurring alone or in combination. Three fundamental mechanisms are 1. excited state absorption (ESA), 2.

photon avalanche (PA), and 3. energy transfer upconversion (ETU) (Excited State Absorption (ESA).

1.2.3.1 Excited State Absorption (ESA)

ESA (Energy State Absorption) involves a multistep excitation process where multiple photons are sequentially absorbed, starting from the ground state to an intermediate reservoir stage, and eventually reaching an excited state. From this excited state, upconversion luminescence occurs**.**

1.2.3.2 Photon Avalanche (PA)

The PA (Photon Avalanche) process is more complex and can be characterized by three distinct nonlinear behaviors: transmission, emission, and rise time, all of which depend on the pump power intensity and typically involve a critical pump threshold. For instance, in a four-energy system, the states E0, E1 and E2 represent the ground state, intermediate states, and upper excited states, respectively.

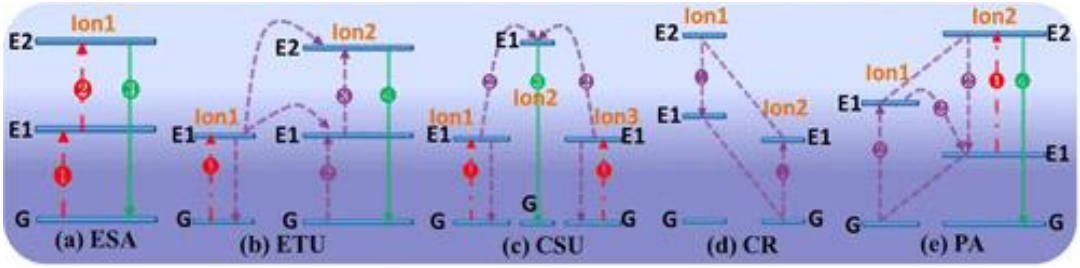

Figure 1.4 Principal UC processes for lanthanide-doped UCNPs: (a) excited-state absorption (ESA), (b) energy transfer upconversion (ETU), (c) cooperative sensitization upconversion (CSU), (d) cross relaxation (CR), and (e) photon avalanche (PA). The red, violet, and green lines represent photon excitation, energy transfer, and emission processes, respectively [1]

1.2.3.3 Non-radiative energy transfer

In ETU, two primary mechanisms are discussed: resonant non-radiative transfer and phonon-assisted non-radiative transfer, both involving a two-ion system [9]. In the resonant non-radiative transfer, when the excited energies of the sensitizer (S) and activator (A) are nearly equal and the distance between them is sufficiently small, energy is transferred from S to A, exciting A from its ground state to an excited state before S emits photons. In phonon-assisted non-radiative transfer, there is an energy mismatch between S and A ions, requiring phonon assistance to facilitate the energy transfer process.

Figure removed due to copyrights issues

Figure 1.5 Non-radiative energy transfer of downshifting processes between two ions: (a) resonant non-radiative transfer; (b) phonon assisted non-radiative transfer (S: sensitizer ions, A: activator ions) [9]

1.2.3.4 Surface modification of RENPs

RENPs can only be dispersed in non-polar solvents and have ligands, usually oleic acid, that do not allow their dispersibility in water for application in biomedicine. For applications in biomedicine, the surface needs to be modified, enabling its dispersibility in water. Different methods have been employed in achieving this, but some of the common ones are: polymer coating [50], silica coating [51], ligand exchange [52], biofunctionalization [53] and surface grafting [54].

1.3 Mechanism of transfer of energy in Nd^{3+} doped rare-earth nanoparticles (RENPs)

Neodymium ion (Nd^{3+}) doped upconversion nanoparticles, which can be excited with an 808 nm laser, have garnered significant attention due to their compatibility with biomedical applications. Nd^{3+} has a large absorption cross-section of approximately 1.2×10^{-19} $cm^{2,}$ which is ten times higher than that of Yb^{3+}[55, 56]. Importantly, Nd^{3+} has a high absorption of NIR light around 808 nm, where water absorption is 20 times lower than that of Yb^{3+} ions. Although Nd^{3+} has an excitation wavelength in the first biological window (650-900 nm), which is ideal for biological applications, the resulting emission bands in the first (650-1000 nm) and second (1000-1350 nm) biological windows limit direct energy transfer from Nd^{3+} ions to emitter ions, hindering efficient upconversion/downshifting [57].

However, co-doping Yb^{3+} ions as a bridge between Nd^{3+} ions and emitter ions in rare earth nanoparticles enhances energy transfer efficiency from Nd^{3+} to emitter ions. This approach also significantly reduces overheating effects and improves laser penetration depth. In Nd^{3+}/Yb^{3+} co-doped rare earth nanoparticles, Nd^{3+} absorbs photons from the 808 nm laser and transfers the energy to Yb^{3+} ions. As a result, the Yb^{3+} ions are excited and subsequently transfer energy to the activators or emitters [58].

There are various methods for calculating the energy transfer efficiency (η) between the energy donor and energy acceptor. One commonly used method is the Dexter-Förster formula, which is expressed as:

$$\eta = 1 - I/I_0 \qquad (1.3)$$

where I and I_0 are the luminescent intensities in the presence and absence of acceptors, respectively. These intensities can be measured under 808 nm and 980 nm laser irradiation for energy transfer from Nd^{3+} ions to Yb^{3+} ions, and from Yb^{3+} ions to emitter ions, respectively. Energy transfer efficiency from Nd^{3+} ions to Yb^{3+} ions has been reported to be around 70% [59].

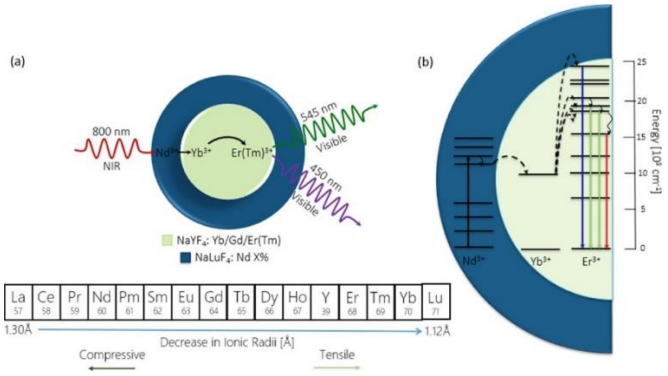

Figure 1.6 Efficient emission relies on effective non-radiative energy transfer from Nd^{3+} to Yb^{3+} ions. The energy transfer mechanism in Nd^{3+} and Yb^{3+} co-doped RENPs involves a two-step process: down-shift followed by upconversion. The energy transfer from Nd^{3+} to Yb^{3+} ions is a downshift process, where one Nd^{3+} ion can transfer phonon-assisted energy to two Yb^{3+} ions due to their 4f energy levels.

The first step, the down-shift mechanism, originates from single-photon absorption, where Nd^{3+} ions transition from the ground state to the higher excited state under 808 nm excitation [60]. Following phonon-assisted relaxation from the ground state to the excited state, the ions in the state drop back to the lower excited state and the ground state, leading to 1060 and 890 nm NIR down-shifting, respectively [61]. The overlap between the emission of Nd^{3+} and the absorption of Yb^{3+} results in resonant energy transfer from the level of Nd^{3+} to the level of Yb^{3+}, populating the Yb^{3+} ions to their excited state and then transitioning back to the ground state, exhibiting 980 nm down-shifting.

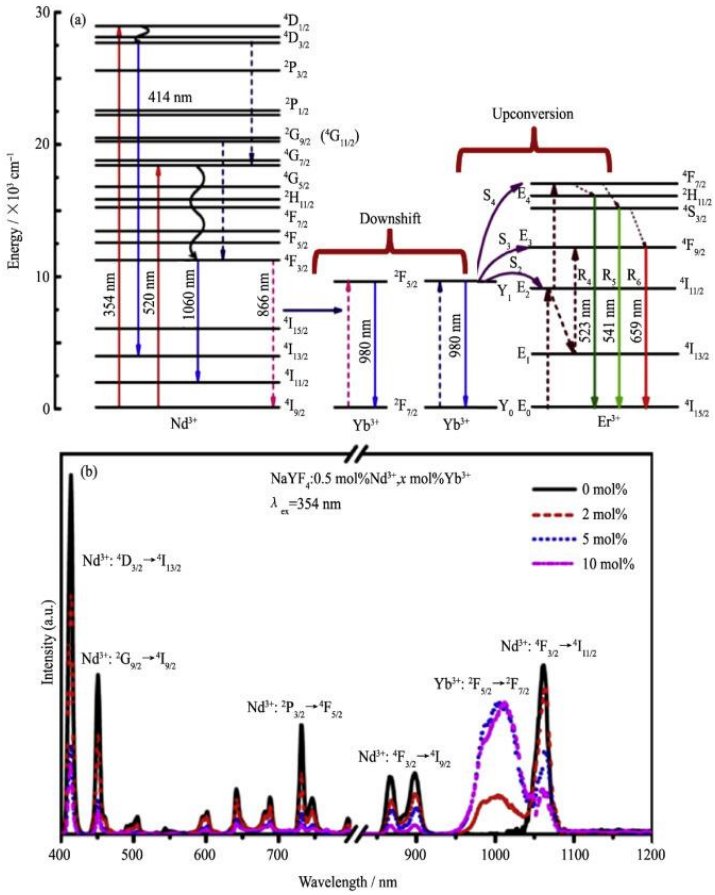

Fig 1.6.1 (a) Schematic illustration of the energy transfer processes diagram and corresponding transitions of Nd^{3+} to Yb^{3+} couple (downshift) and transitions from Yb^{3+} to Er^{3+} (upconversion); (b) Emission spectra of $NaYF_4$:0.5 mol%Nd^{3+}, x mol%Yb^{3+} (where x 0, 2, 5, and 10) in the visible (left) and NIR (right) region under 354 nm excitation

Several studies have investigated the energy transfer from Nd^{3+} to Yb^{3+} ions [62]. For instance [24]You and your group demonstrated this energy transfer by analyzing the emission spectra of $NaYF_4$:0.5 mol% Nd^{3+}, x mol% Yb^{3+} nanoparticles co-doped with various concentrations of Yb^{3+} ions. Their findings showed that the emission bands of Nd^{3+} ions significantly reduced as the Yb^{3+} ion concentration increased, while a Yb^{3+} emission band around 980 nm emerged, indicating energy transfer from Nd^{3+} to Yb^{3+} ions.

1.4 Morphology in RENPs

Different morphologies and nanocomposites significantly affect the properties of rare-earth nanomaterials. Developing novel morphologies and composites is crucial for discovering their potential applications. Additionally, multimodal imaging materials with innovative structures have

been a prominent research focus in recent years. In this section, we will also highlight recent advancements in hybrid materials that combine magnetic properties with luminescence. To date, an increasing number of researchers are dedicated to systematically synthesizing rare-earth nanocrystals with various morphologies (spheres, rods, prisms, tubes, octahedrals, spindles) and particle sizes through different synthetic processes. Zhang et al. have reported a straightforward hydrothermal method for preparing uniform nanostructured arrays of sodium rare-earth fluorides. This method effectively controls the phases, sizes, and morphologies (tubes, disks, or rods) using oleic acid (OA) as a stabilizing agent, $M(NO_3)$, and NaF as precursors within a temperature range of 130 °C to 230 °C. Zeng et al. synthesized highly uniform hexagonal phase $NaReF_4$ nanocrystals with well-defined shapes, including spheres, pills, rods, plates, and tubes, using a facile solution-based hydrothermal method with OA as a stabilizing agent [63]. By adjusting the molar ratio of F/RE and the reaction temperature, they could tune the crystal phase, size, and shape. Additionally, they achieved red, green, and blue luminescence under 980 nm excitation by doping a $NaYbF_4$ host with Er/Ho/Tm. Na et al. reported the systematic synthesis of β-$NaYF_4$, Yb, Er nanocrystals with varied morphologies [64], from spheres (37.9 nm) to rods and hexagonal prisms [65]. They controlled the morphology of β-$NaYF_4$, Er UCNPs through the thermal decomposition of lanthanide precursors by using a surfactant, an additive, and lanthanide doping. For instance, the quantity of the OA ligand, the OA/ODE ratio, and Gd^{3+} doping all contributed to simultaneous changes in size and morphology. Rare-earth nanoparticles (RENPs) exhibit different morphologies, which include nanospheres, nanorods, nanowires, and more complex shapes like core-shell structures. This morphology directly influences their optical behaviour and stability.

Figure removed due to copyrights issues

Figure 1.7 TEM images of the *β*-$NaYF_4$-based UCNPs. (*A*, *D*, *G*, *J*) $NaYF_4$: Yb/Er (20/2 mol%) RENPs. (*B*, *E*, *H*, *K*) $NaYF_4$: Yb/Tm (22/0.2 mol%) RENPs. (*F*, *I*) $NaYF_4$: Yb/Ho (20/2 mol%) RENPs. (C, L) $NaYF_4$: Yb/Ce/Ho (20/11/2 mol%) RENPs. All scale bars represent 100 nm [66]

Li et al. have demonstrated an easy hydrothermal method for synthesizing lutetium fluorides with various crystal phases and morphologies, including β-$NaLuF_4$ hexagonal microprisms, microdisks, microtubes, and spherical particles. Wu et al. reported the synthesis of Gd^{3+} fluorides with different phases (GdF_3, β-$NaGdF_4$) and diverse morphologies via a simple hydrothermal route [67]. The morphologies of these upconversion nanocrystals range from submicrorods, dumbbell-like nanorods, and submicrospheres to cobblestone-like particles and aggregates made from nanoparticles [68]. The mesoporous and hollow structures of these materials are often crucial for drug carriers. Xu et al. detailed the creation of monodisperse core–shell structured $Yb(OH)CO_3$@$YbPO_4$ hollow spheres and thoroughly examined their drug loading and release properties [68].

1.4.1 Morphology of heavily doped rare-earth nanoparticles

Nanoparticles sensitized by Nd^{3+}-sensitized are highly sought after for biomedical applications, such as deep tissue imaging and photodynamic therapy, due to their enhanced biocompatibility. However, the high surface area-to-volume ratio of small-sized upconversion nanoparticles often leads to numerous surface defects, which can increase surface quenching and reduce upconversion luminescence. Doping metal ions into any layer of upconversion nanoparticles can replace lanthanide ions in the host crystal, potentially resolving these issues. If the substituted lanthanide ion and the doped metal ion have different valence electrons, they will induce charge imbalances in the crystal lattice, causing the created ions to diffuse to the nanoparticle surface. Once the diffusion process is saturated, it results in full coverage of the nanoparticles, leading to a uniform morphology with fewer surface defects and enhanced upconversion luminescence intensity [69].

In this context, Zhang et al [70]. fabricated ultra-small, highly emissive Nd^{3+}-sensitized upconversion nanoparticles doped with Ca^{2+} ions ($NaGdF_4$,Tm,Ca@$NaYbF_4$@$NaNdF_4$,Ca) for 808 nm laser-activated drug release. Doping 10 mol% of Ca^{2+} ions into all layers of the nanoparticles resulted in significantly small RENPs with a three-fold increase in luminescence intensity compared to Ca^2-free nanoparticles. This enhancement is attributed to lower crystal field symmetry around Yb^{3+} and Tm^{3+}, improved crystallinity of host materials, and reduced surface quenching due to the replacement of Gd^{3+} with Ca^{2+} ions in the host crystal ($NaGdF_4$), which induced vacancies. These vacancies not only suppressed surface defects but also improved the uniformity of the nanoparticles.

Figure removed due to copyrights issues

Figure 1.8 Effects of high Nd^{3+} shell concentrations. (a) TEM image of $NaYF_4$:Yb/Gd/Er@$NaLuF_4$:60%Nd (left), @$NaLuF_4$:75%Nd (middle), and @$NaNdF_4$ (right). (b) Emission spectra of Er^{3+}-doped CS NPs of high Nd concentrations obtained via a fluorimeter with excitation source set at 0.6 W/cm^2 at 800 nm. (c) Quantification of the area under the curve. Green emission includes peaks at 522 and 545 nm. Red emission includes a peak at 645 nm [71]

Furthermore, doping ions into upconversion nanoparticles can enhance upconversion luminescence intensity and tune the emission spectra color [72, 73]. As an example, Chen et al. [56] reported Ce^{3+}-doped Nd^{3+}-sensitized upconversion nanoparticles (Yb/Ho/Ce_4@Yb/Nd_4), which increased the red-to-green intensity ratio. The enhancement of Ho^{3+} red upconversion emission and reduction of green emission after doping Ce^{3+} ions in the core (Yb/Ho/Ce_4) were attributed to efficient cross-relaxation processes between Ho^{3+} and Ce^{3+}.

1.4.1.1 Effect of the morphology of RENPs in Nanothermometry

It is clear that several nanoparticle properties, such as particle size, charge, and surface characteristics, significantly impact drug delivery. Additionally, nanoparticle shape has proven to be highly useful in developing nanocarriers (NC). While the importance of nanoparticle shape in nanothermometry has been discussed by several authors [74, 75]. The exact role of particle shape remains to be fully understood. The shape of nanoparticles is typically determined by the synthesis methods, with techniques like ab initio used to produce particles with non-spherical geometries [76]. Non-spherical particles may have varying lengths, with one dimension potentially dominating the others.

Regardless of the administration route, particle shape greatly influences the transport and diffusion of nanoparticles. Spherical particles move more easily due to their symmetry, whereas

non-spherical particles tend to tumble with the flow, which is particularly evident in filtering organs like the spleen and liver. For instance, folic acid-targeting folate ligands in the form of spherical and wormlike micelles (75 and 200 nm) using acrylic acid (AA) and PEG methyl-ether acrylate (PEGMEA) were designed for drug delivery [77]. Wormlike micelles showed higher accumulation in the spleen, liver, and kidneys compared to spherical particles. Long filomicelles stretch out when flow velocity exceeds 5 μm/s, a condition common in most blood vessels and the filtering spleen [78].

Studies have shown that the shape, geometry, and orientation of nanoparticles significantly affect cellular uptake [79, 80]. Even non-spherical particles larger than 200 nm can pass through the spleen if one of their dimensions is less than 200 nm [81]. The target-specificity of nanoparticles is also influenced by their shape, which can affect the longevity and internalization of particles. Therefore, it is concluded that the symmetry of nanoparticles is crucial for effective drug delivery.

1.4.2 Impact on Optical Properties

The morphology of RENPs, including their size, shape, and surface characteristics, critically influences their optical properties [2]. The efficiency of the luminescence is highly dependent on these morphological parameters [6] . Nanoparticle applications are largely dictated by their properties, with particle size and size distribution being particularly critical. These factors significantly impact drug loading, release, toxicity, in vivo distribution, and particle stability. A major limitation in nanoparticle-assisted drug delivery is clearance by the reticuloendothelial system (RES) through opsonization, where size plays a key role in both clearance and distribution. When particle size exceeds 100 nm, pharmacokinetic and biodistribution properties change considerably, with nanoparticles being detected in blood and organs such as the spleen, lungs, liver, and kidneys [82]. Positively charged nanoparticles are taken up more effectively by direct permeation compared to neutral and negatively charged nanoparticles [83].

Nanoparticle size, or particle diameter, can be controlled through fabrication methods or by adjusting physical properties, especially the concentration of the polymer or surfactant. For brain-targeted drug delivery systems, treating brain tumors is facilitated by shrinking endothelial cells and opening endothelial tight junctions to allow chemotherapeutics to cross the blood-brain barrier (BBB)[84]. To enhance paracellular transport, tight junctions can be selectively opened, allowing particles smaller than 20 nm to penetrate the brain via the BBB [84]. Hyper-osmotic mannitol's BBB-disrupting properties enable effective nanoparticle penetration across the BBB [84]. For optimal penetration, particle diameters should ideally range from 10 to 150 nm to ensure longer

circulation times and increased accumulation at the target site [85]. The rate of drug release can be tuned by particle size; larger particles can accommodate more drug molecules for slow release [86]. Conversely, smaller nanoparticles have a high surface-volume ratio, which can lead to quick aggregation and rapid drug release due to adhesion to the particle surface. Smaller nanoparticles typically exhibit higher surface-to-volume ratios, which can enhance the luminescence process[5]. Uniformly shaped nanoparticles, such as spheres, tend to provide more consistent and stable luminescence compared to irregularly shaped particles [1].

Figure removed due to copyrights issues

Figure 1.9 Schematic illustration of proposed energy transfer mechanisms of core-shell rare-earth nanoparticles under 808 nm laser irradiation (a) and a rare-earth nanoparticle with a different composition of core-shell structure under 808 nm laser irradiation (b). TEM images of core ($NaYF_4$: Yb,Er,Nd) (c) and core-shell ($NaYF_4$:Yb,Er,Nd@$NaYF_4$:$Yb_{0.1}Nd_{0.2}$) nanoparticles (d), and emission spectra of RENPs with different compositions and structure under 808 nm excitation (power density, 2 W/cm^2) (e). Inset demonstrates the photographs of $NaYF_4$:Yb,Er,Nd@$NaYF_4$:$Yb_{0.1}Nd_{0.2}$ nanoparticles under the excitation of 808 and 980 nm laser (power density, 2 W/cm^2). (Adopted from Ref. 52).

1.4.3 Biological Interactions

Nanoscale materials are being increasingly utilized in the medical sector to enhance the targeting efficiency of medications. Nanoparticles are extensively utilized in drug delivery and bioimaging due to their tunable size, shape, and surface properties, which can be tailored for targeting specific diseases [87, 88]. The surfaces of these nanoparticles can be modified with various targeting

molecules, such as antibodies, peptides, and aptamers, to enhance their efficiency in reaching disease sites.

Recently, researchers have begun exploring how variations in size, shape, and surface chemistry impact endocytosis, toxicity, and gene regulation [89, 90]. However, the formation of aggregates (strongly bonded nanoparticles) and agglomerates (loosely bonded nanoparticles or aggregates due to weak forces like van der Waals forces) in biological media has not been fully considered for optimizing their physicochemical properties for biological applications. It has been suggested that aggregates or agglomerates form when van der Waals attractive forces between nanoparticles surpass the electrostatic repulsive forces [91]. During studies of nanoparticle endocytosis and exocytosis, cells are exposed to nanoparticles in a culture medium containing various serum proteins. Most nanoparticles first become coated with these serum proteins before interacting with the cell plasma membrane. If nanoparticles are aggregated or agglomerated before binding to the membrane, their endocytosis patterns would differ from those of individual nanoparticles. The extent of nanoparticle aggregation or agglomeration can be assessed by measuring the time-dependent changes in size and surface charge of nanoparticles in the culture medium. Techniques such as transmission electron microscopy (TEM) and dynamic light scattering (DLS) are used to analyze the (hydrodynamic) size, while zeta potential measurements determine surface charge.

The cellular uptake of nanoparticles is extensively studied across various cell lines due to the significant role that nanoparticle size plays in determining uptake pathways. Key in vivo functions of nanoparticles, including circulation time, targeting, internalization, and clearance, are influenced by their size. Therefore, the cellular uptake of nanoparticles of different sizes[92]. Significant interest has been directed toward understanding size-dependent nanoparticle internalization in cancer cells and fibroblasts. For instance, [89, 93, 94]studies on human cervical cancer cells revealed that gold nanoparticles of 50 nm size exhibited the most efficient cellular uptake compared to other sizes. Similarly, experiments on a human colon adenocarcinoma cell line [95] with polystyrene (PS) nanoparticles of various sizes found that 100 nm PS nanoparticles were internalized more effectively than those of 50, 200, 500, and 1,000 nm sizes, with 50 nm PS nanoparticles showing the least efficient uptake. These studies indicate that cellular uptake patterns may also vary according to the nanoparticle material type. Furthermore, despite using different cancer cell lines, these experiments suggest that the stiffness of nanoparticles could influence their cellular uptake, with stiffer nanoparticles interacting more tightly with the plasma membrane and undergoing rapid endocytosis [92].

The morphology of RENPs also affects their interactions with biological systems. Size and shape determine how nanoparticles are internalized by cells and distributed within tissues [5]. Nanoparticles with diameters between 10-100 nm are generally more efficiently taken up by cells through endocytosis [1] . Additionally, surface characteristics influence the biocompatibility of RENPs, their dispersibility in biological media, and their ability to evade the immune system [6] .

Figure removed due to copyrights issues

Figure 2.0 Schematic representation of gold nanoparticles. (B) Transmission electron microscope images of citrate-coated gold nanoparticles with various sizes. (C) Transmission electron microscope images of the gold nanoparticles entrapped in cellular vesicles. Graph showing the number of gold nanoparticles per vesicle diameter.[89]

1.4.4 Relevance to Cancer Therapy

In cancer therapy, the morphology of RENPs is crucial for ensuring effective treatment. Well-defined and uniformly shaped nanoparticles can improve the delivery and activation of therapeutic agents, enhancing treatment efficacy [1] . In photodynamic therapy (PDT) and photothermal therapy (PTT), optimal morphology ensures efficient light absorption and conversion, which is vital for generating reactive oxygen species (ROS) or heat to kill cancer [2].

Figure removed due to copyrights issues

Fig 2.1 (a) Fluorescence top-image of the CD1 mouse (delimited by the dashed line) where the subcutaneous injection of $LaF_3:Nd^{3+}@LaF_3:Yb^{3+}$ NPs is evidenced by the bright fluorescence spot. (b) Digital picture of the CD1 mouse during in vivo thermal relaxation experiments. (c) Schematic representation of the subcutaneous thermal relaxation experiments. Thermal infrared images of the CD1 mouse before (d) and at the end (e) of the heating stimulus. (f) Time evolution of the temperatures measured by the subcutaneous luminescent thermometer (grey) and the IR thermal camera (orange). Dots are experimental subcutaneous (circles) and skin (squares) temperatures, whereas the solid line is the best fit [96]

PDT broadly refers to a biochemical alteration of cell functions triggered by light-induced generation of reactive oxygen species (ROS). Despite the longstanding use of light for therapeutic purposes across various cultures, interest in utilizing PDT for tumor treatment has notably increased in recent years[97]. The mechanism of PDT involves inducing cell death by damaging essential components such as DNA, proteins, and cellular membranes [98]. For PDT to be effective, it must meet specific criteria: lack of dark toxicity, highly selective spatial treatment, and combined treatment and imaging capabilities [98].

NIR irradiation of nanoparticles (NPs) characterized by localized surface plasmon resonance (LSPR) can generate a photoacoustic (PA) signal, which can be utilized for tumor imaging[99]. The increase in local temperature due to laser irradiation of the NPs increases pressure, as described by the following equation:

$$p_0=\beta\cdot\Delta T/\kappa \quad (1.4)$$

where β is the coefficient of thermal expansion and κ is the isothermal compressibility [100]. The pressure waves induced by laser irradiation are collected by an ultrasound transducer and processed to generate PA images. Metal NPs serve as excellent contrast agents for photoacoustic imaging (PAI) because they resist photobleaching. However, prolonged laser irradiation can alter their morphology, reducing the overall signal and contrast compared to the background [100]. The size and shape of the nanosystems influence the intensity of the recorded PA signal [101]. Despite this, a comprehensive model linking dimensions with photothermal and PA signals is still lacking, hindering the rational development of NP-assisted PAI for tumors. Semiconductor and transition metal nanosystems, such as copper selenide, offer advantages over noble metal particles. These systems can shift the absorption peak to the second NIR window (1000 to 1700nm), where background interference primarily comes from water rather than tissue [102]. However, a drawback of PAI is its limited penetration depth (approximately 5 cm), necessitating the development of probes for both the laser and transducer when the target tissue is not at the surface of the body [99, 100].

1.5 Strategies for Controlling Morphology

1.5.1 Synthesis of Rare-earth Nanoparticles

To achieve high luminescence efficiency, synthesizing high-quality RENPs (Rare-earth Nanoparticles) is essential. There are three common methods for synthesizing RENPs: thermal decomposition, hydrothermal synthesis, and ionic liquids-based synthesis.

1.5.1.1 Thermal Decomposition Method

Thermal decomposition is one of the most popular methods, producing well-shaped particles with good size control in a relatively short reaction time. This method typically involves dissolving organic precursors in high-boiling organic solvents with the aid of surfactants. Common organic precursors include trifluoroacetate compounds, while typical surfactants have polar capping groups and long hydrocarbon chains, such as oleic acid (OA), oleylamine (OM), and 1-octadecene (ODE). Mai et al. systematically investigated the growth mechanism of nanocrystals, identifying a unique delayed nucleation pathway for trifluoroacetate precursors in hot surfactant solutions [103]. The

synthesis process is divided into four stages: nucleation after a delay, particle growth through monomer supply, size reduction by dissolution, and aggregation. The figure below illustrates the synthesis of lanthanide-based rare-earth nanoparticles.

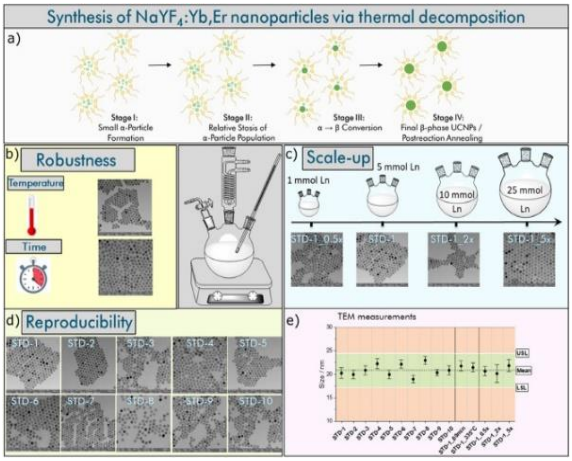

Figure 2.2 (a) Schematic illustration of the formation and growth of RENPs by the thermal decomposition method according to Refs [104, 105]. The Ln precursor thermally decomposes at a higher temperature to initially yield small cubic α-phase particles, which are then transformed into larger thermodynamically favored hexagonal β-phase particles via a thermodynamically driven dissolution–recrystallization process. (b–e) Reproducibility, robustness, and up-scalability of the basic synthetic procedure that yields 20 nm β-Yb,Er-co-doped $NaYF_4$ RENPs. TEM images of the RENPs obtained from (b) a reaction performed with an increased temperature (335 °C instead of 325 °C) and a prolongated reaction time (60 min instead of 30 min); (c) different batch sizes (1–25 mmol RE precursors) to assess the robustness of the synthesis, and (d) ten independent reactions performed under the same reaction condition (STD 1–STD 10) to explore the reproducibility of the synthesis. (e) Size distribution of the obtained RENPs as determined by TEM.

1.5.1.2 Hydrothermal Synthesis Method

Hydrothermal synthesis is a solution-based method typically employed under high temperatures and pressures [13, 106, 107]. In contrast to thermal decomposition, which uses only organic solvents, hydrothermal synthesis can occur in a water-based system at lower temperatures (160–220 °C), making it a more environmentally friendly approach. This method is effective and convenient for preparing inorganic materials with various controllable morphologies and architectures.

For example, using hydrothermal synthesis, various shapes of hexagonal $NaYF_4$ crystals, such as prism, disk, tube, rod, and octadecahedral shapes, have been produced [108, 109]. Recently, Lin's group systematically investigated the mechanism of synthesizing different shapes of rare earth (RE) fluoride nano-/microcrystals[109]. They reported that the organic additive trisodium citrate, the fluoride source, and the pH value significantly impact the resulting crystal shapes.

Figure removed due to copyrights issues

Figure 2.3 Different shapes of RE fluoride nano-/microcrystals by the hydrothermal method [110]

1.5.1.3 Ionic liquid-based synthesis method

Compared to the other two methods, ionic liquid-based synthesis is considered more environmentally friendly because it doesn't require organic solvents, operates at a lower reaction temperature, and has a shorter reaction time. Nanomaterials are synthesized in ionic liquid media, which are referred to as “green solvents” due to their chemical stability, low vapor pressure, and non-flammability. However, the resulting nanomaterials often have lower quality, with a broader size distribution, reduced monodispersity, and less uniformity compared to the other methods. This limitation restricts their applications [111]. Therefore, thermal decomposition and hydrothermal synthesis methods remain the most widely used and preferred techniques for producing RE fluoride nanomaterials with well-controlled shapes and sizes.

Different methods of synthesizing nanoparticles are needed for different purposes. Table 1 shows some of the advantages and disadvantages of different synthesis methods:

Table 1. Advantages and disadvantages of different synthesis methods

Method	Advantages	Disadvantages
Co-precipitation method	• Quick synthesis • Low-cost • No need for expensive equipment or harsh reaction conditions • Simple procedures	• Requires post-heat treatment • Lack of control over particle size • Significant aggregation • Typically requires high-temperature calcination • Not suitable for large-scale synthesis of UCNPs
Sol-gel processing	• Inexpensive precursors. • Suitable for large-scale production. • High luminescence intensity due to high crystallinity achieved at high annealing temperatures	• Often requires post-heat treatment • Significant particle aggregation • Broad particle size distribution. • Irregular morphology, Insoluble in water
Thermal decomposition	• Produces high-quality, monodispersed nanocrystals with strong upconversion emission	• Requires temperatures usually exceeding 300°C • Uses expensive and air-sensitive metal precursors • Generates toxic by-products

		• Needs an anaerobic and water-free reaction environment
Hydro/solvothermal method	• Produces high-quality crystals with controllable particle size, shape, and dopant ion concentrations • Does not require stringent operational conditions • Operates at lower reaction temperatures	• Difficult to observe nanocrystal growth processes • Challenging to determine optimal experimental conditions (e.g., reaction temperature, surfactant type and concentration, reactant concentration, solvent composition, and reaction time) • Typically results in a large size distribution
Microemulsion method	• Low-cost equipment • Easy operation • Produces small UCNPs with controlled morphology by adjusting surfactant dosage, solvent, and aging time	• Generally, yields a small amount of product • Difficult sample separation • Limited synthesis scope

1.5.2 Core/shell structure

One widely used approach to improve rare-earth emission involves adding a shell to a luminescent core. This method helps to reduce nonradiative decay caused by surface defects. Typically, the shell is inert and serves to protect the luminescent ions in the core from surface defects and vibrational deactivation by the solvent and surface-bound ligands [112].

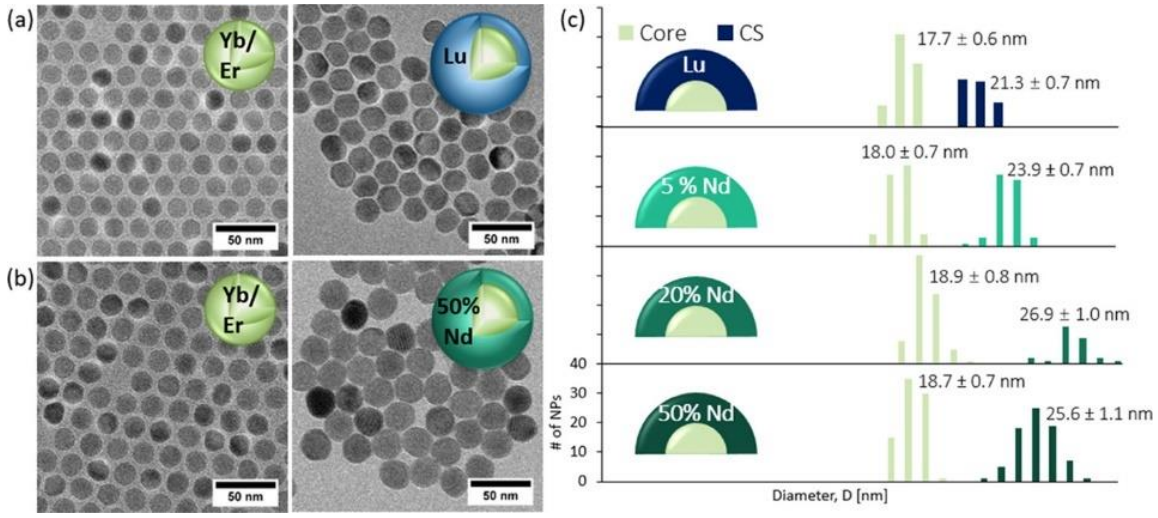

Figure 2.4 Characterization of CS NP morphology. TEM images of Er^{3+}-doped cores and an epitaxially grown shell. (a) As-synthesized $NaYF_4$:Yb/Gd/Er cores (left) and $NaLuF_4$ shell grown onto the core (right). (b) As-synthesized $NaYF_4$:Yb/Gd/Er cores (left) and $NaLuF_4$:50 mol % Nd shell grown onto the core (right). (c) A histogram displaying the size distribution of NPs

Rare-earth nanoparticles (RENPs) synthesized by wet chemical methods often suffer from surface defects and the vibrations of capping ligands, which negatively impact their emissions. Boyer and van Veggel [113] noted a significant reduction in the quantum yield of RENPs as particle size decreased, attributing this to the increased presence of surface defects in smaller particles. Capobianco and colleagues [114] examined the influence of hydroxyl groups on the emissions of Er^{3+} ions. They found that removing the original oleate ligands from RENPs led to an enhanced red-to-green emission ratio in the spectra. One effective method to mitigate surface effects is the creation of core/shell structures. Liu and collaborators [115] explored the surface quenching effect by comparing the blue-to-NIR emission intensity ratio of Tm^{3+} ions and the overall emission intensity before and after the growth of a shell. Van Veggel and team [116] demonstrated a novel approach involving the epitaxial layer-by-layer growth of $NaYF_4$, Er RENPs using Ostwald ripening dynamics. The results from spectral analysis showed a consistent increase in emission intensity with the growing thickness of the shell [117] layer, and the emission intensity was observed to increase linearly with shell thickness.

Figure removed due to copyrights issues

.

Figure 2.5 (a) Schematic design of the active-core/active-shell nanoparticle architecture for photon upconversion upon 808 nm laser excitation. Nd^{3+} and Yb^{3+} ions are simultaneously co-doped in both the core and shell layers, and act as co-sensitizers to absorb the excitation energy and subsequently transfer it to the Ln^{3+} activator ions, giving rise to upconverted emissions. (b) Schematic illustration of the energy transfer mechanism in the active-core/active-shell nanoparticles [118]

Several research efforts have focused on minimizing surface quenching and energy back transfer by systematically isolating the luminescent center from interactions with solvents and surface defects. Optimizing the distance between the activator and sensitizer using core-single shell or core-multishell designs of rare-earth nanoparticles has been a widely utilized strategy. For example, Liu et al. [119] introduced core-multishell rare-earth nanoparticles ($NaYF_4$,Er@$NaYF_4$@$NaNdF_4$@$NaYF_4$), abbreviated as Er@Y@Nd@Y, which exhibited a quantum yield of 0.18% and a 12.8-fold enhancement in luminescence intensity compared to Er@Y@Nd nanoparticles under 808 nm excitation for biological imaging. The $NaYF_4$, Er core, doped with 20 mol% Yb^{3+} and 2 mol% Er^{3+}, served as the luminescence center. The first shell ($NaYF_4$), doped with 10 mol% Yb^{3+}, functioned as the energy transfer layer. The second shell ($NaNdF_4$), doped with 90 mol% Nd^{3+} and 10 mol% Yb^{3+}, acted as the photon energy harvesting layer. The third shell ($NaYF_4$), doped with 10 mol% Yb^{3+}, was used for both energy transfer and surface quenching reduction. The optimal core size ($NaYF_4$, Er) for maximum upconversion luminescence intensity in the designed core-multishell nanoparticle was determined to be 30nm.

More recently, Liu et al [120] designed a core-active shell structure ($NaYF_4$, Er,Nd@$NaYF_{40.1}Nd_{0.2}$). The active shell significantly suppressed surface quenching and reduced

energy back transfer from Er^{3+} to Nd^{3+} due to co-doped Yb^{3+} ions, which promoted energy transfer from Nd^{3+} to Er^{3+} and prevented energy back transfer. This design achieved a 21.28-fold enhancement in luminescent intensity compared to the bare core by doping 10 mol% Yb^{3+} ions into the active shell. Xie et al. [121] reported a similar enhancement in luminescence intensity using a core-active shell architecture ($NaYF_4$/Tm/Nd (18%/0.5%/1%)@$NaYF_4$(20%)). The active shell ($NaYF_4$) coated core exhibited much stronger luminescence intensity than the inert shell ($NaYF_4$) coated counterpart, although the lifetime of nanoparticles modified with both active and inert shells was found to be similar.

Recently, Zhou et al. [122] developed an interfacial energy transfer (IET) strategy to reduce non-radiative energy decay caused by back energy transfer using core-shell-shell structures. In this method, the energy donor (sensitizer ions) and the luminescent energy acceptor (activator ions) were doped into separate layers of a core-shell-shell structure. Unlike conventional donor-acceptor co-doping (doping into the same layer), doping donors and acceptors into separate layers minimized deleterious interactions and enhanced luminescence. The IET strategy also allowed manipulation of various activators to design rare-earth nanoparticles with multicolor capabilities.

In my group, we recently checked the emission intensity of heavily doped lithium-based rare-earth nanoparticles ignited at 808 nm to see their compatibility for applications in cancer therapy [123]

1.6 Applications

Interest in rare-earth phenomenon has been on the rise since it was first identified in the mid-1960s. It has found widespread use in solid-state lasers, particularly those emitting blue light [124], as well as in solar cells [125, 126] and waveguide amplifiers [127, 128]. The biological applications of rare-earth nanomaterials were not considered until significant advancements in nanotechnology occurred over the past decade. The successful synthesis of high-quality, lanthanide-doped rare-earth nanomaterials (RENs) has expanded their range of applications. Recently, RENPs have been developed for non-destructive optical memory [129] and rewritable optical storage applications [130]. Due to their controllable sizes and unique luminescence properties, RENs have emerged as promising alternatives to traditional organic dyes and quantum dots (QDs) in the biological field. Compared to organic dyes and QDs, RENs offer high quantum yields, long lifetimes, excellent photostability, narrow emission peaks, and crucially, low optical background noise due to the absence of autofluorescence under near-infrared (NIR)

radiation. Multiple analytes can be detected simultaneously using different RENs excited by the same IR laser [124]. Additionally, RENs have been extensively studied for applications in bio-labeling [14, 18, 131, 132], homogeneous assays [19, 133, 134], and as reporters in DNA microarrays.

1.6.1 Applications in Optical Imaging

Optical imaging is a vital tool in biological research and clinical applications, enabling the visualization of morphological details in tissue. Traditional optical imaging, despite its widespread use in both in vivo and in vitro studies with various functional nanoparticles, faces several inherent challenges. These include significant autofluorescence from biological tissues, limited penetration depth, and the potential for causing DNA damage or cell death [6, 135-139]. These limitations arise because many traditional methods rely on downshifting phenomena, where high-energy light (typically UV or visible light) excites materials to emit low-energy fluorescence. Therefore, identifying an alternative imaging method with low background signals and deep tissue penetration is crucial. Lanthanide-doped materials were first used in tissue imaging in 1999, when Zijlmans et al observed minimal autofluorescence and no photobleaching even after prolonged exposure to high excitation energy levels [124]. However, the submicron size of the particles used at the time limited their applications. Recent advancements in synthesis techniques have made it possible to produce smaller, high-quality rare-earth nanoparticles (RENPs). RENPs-based imaging techniques have since been explored and widely applied in cell, tissue, and animal imaging [20, 124, 140-144]. Wu et al. demonstrated that UCNs could be used for single-molecule imaging, with individual UCNs bright enough to be observed using a low-power continuous-wave (CW) laser. They also noted the high photostability of UCNs, maintaining brightness even after more than an hour of continuous laser illumination, making them suitable for long-term cell observation. RENPs offer additional advantages for bioimaging, including low background fluorescence and a high signal-to-noise ratio. Lim et al [30, 145] conducted in vivo imaging and scanning electron microscopy studies of RENPs in *Caenorhabditis elegans* (C. elegans), chosen for its short life cycle, rapid growth, and suitable size for optical microscopy. In their study, *C. elegans* were fed RENPs and imaged at regular intervals to track the movement of the phosphors through their digestive system. No significant changes in the phosphors were observed up to 24 hours, and the phosphors were excreted within two hours after feeding. This demonstrated that RENPs are nonbleaching, biocompatible, and nontoxic, making them ideal candidates for use in biological systems.

The ability to control the color output of nanomaterials significantly enhances their potential applications, particularly in multiplexed biological labeling and imaging. Various methods, such as those based on surface plasmon resonance [146-149] or utilizing multicolor-encoded microbeads and nanoparticles [150, 151]have been employed to achieve multicolor output. However, these approaches often require high-energy UV excitation sources, which can limit their use in bioimaging due to significant background autofluorescence and potential photodamage to samples. Rare-earth nanoparticle (RENP)-based methods offer a promising solution to these challenges, and recent research has demonstrated the possibility of achieving multicolor emission. This can be done by adjusting factors such as reaction temperature and time, crystal structure, and phase, or by altering the combinations and concentrations of lanthanide dopants [6, 152-154].

Figure removed due to copyrights issues

Figure 2.6 Room temperature upconversion emission spectra of (a) NaYF:Yb/Er (18/2 mol%), (b) NaYF:Yb/Tm (20/0.2 mol%), (c) NaYF:Yb/Er (25–60/2 mol%), and (d) NaYF:Yb/Tm/Er (20/0.2/0.2–1.5 mol%) particles in ethanolsolutions. The spectra in (c) and (d) were normalized to Er 650 nm and Tm 480 emissions, respectively.Compiled luminescent photos showing corresponding colloidal solutions of (e) NaYF:Yb/Tm (20/0.2 mol%),(f–j) NaYF:Yb/Tm/Er (20/0.2/0.2–1.5 mol%), and (k–n) NaYF:Yb/Er (18–60/2 mol%). The samples were ex-cited at 980 nm with a 600 mW diode laser [6]

Ehlert et al showed that four different colors of UCNs could be spectrally separated under multiplexing conditions using a single 980 nm excitation source [155]. Additionally, Li and co-workers achieved multicolor output by encapsulating organic dyes or quantum dots (QDs) into a silica shell, with upconversion fluorescence generated through Forster resonance energy transfer

(FRET) from the UCN cores to the organic dyes or QDs [156]. The emission efficiency of upconversion nanoparticles (UCNs) can be further improved through various methods, such as integrating other metal nanoparticles [20, 157], surface modification [158], and incorporating multiple lanthanide ions[159]. Chen and colleagues recently discovered that by increasing the concentration of doped Yb^{3+} ions from 20% to 100%, the NIR-to-NIR upconversion photoluminescence intensity increased approximately 8.6 times per unit of Yb concentration and 43 times per nanoparticle [160].

1.6.2 Applications in Sensors

DNA/RNA analysis plays a crucial role in molecular biology, genetics, and molecular medicine. Significant efforts have been devoted to developing precise concentration detection methods, including those based on metal nanoparticles[161-164]. In recent years, rare-earth nanoparticles (RENPs) have also been utilized for the sensitive detection of oligonucleotides. For instance, van de Rijke et al. [165] and Corstjens et al. [166] used RENPs as direct labeling reagents to detect single-stranded nucleic acids. A novel design for a nucleotide sensor by Zhang et al. [167] employed RENPs as energy donors and another fluorophore as an energy acceptor in a sandwich assay format. When UCNs are irradiated with IR light, they transfer energy to the fluorophore, causing it to emit light. The presence of target oligonucleotides can be detected by monitoring the emission from the fluorophore. This sensor demonstrated high sensitivity (1.3nM), high specificity, and self-calibration capability. Recently, Liu et al. [168] reported a general apt sensor for detecting various target molecules, based on UCNs-graphene oxide FRET. This design can potentially be extended to sense other types of molecules and induce structural conformations in ssDNA, showing significant promise for clinical diagnostics and biosensing applications.

Figure removed due to copyrights issues

Figure 2.7 The schematic of the nucleotide sensor design[167].

Rare-earth nanoparticle (RENP)-based sensors are utilized in both biological and chemical fields. Mader et al.[169] developed an ammonia sensor using RENPs and the pH indicator phenol red, immobilized in a polystyrene matrix. In the presence of ammonia, the 560 nm absorption of the pH indicator increased significantly, which reduced the visibility of the green emission from the RENPs, while the red emission remained unaffected. The ratio of the intensities of the green and red emissions from the RENPs served as the detection signal. Achatz et al. were the first to create an oxygen sensor using RENPs as nanolamps. In their method, RENPs acted as a light source to photoexcite an iridium(III) complex, whose fluorescence was quenched dynamically by oxygen.

More recently, Li et al. [170] described a highly selective and sensitive cyanide (CN^-) sensor using UCNs coated with a chromophoric iridium(III) complex. This was the first instance where such a sensor could be used both for bioimaging an anion in living cells and for detection, offering a very low detection limit of 0.18μM in aqueous solution. Additionally, Li's group [171] developed a sensor for mercury ions (Hg^{2+}) using a chromophoric ruthenium complex-assembled RENP. This Hg^{2+} nanoprobe demonstrated its ability not only to monitor Hg^{2+} concentration but also to track changes in Hg^{2+} distribution within living cells through luminescence bioimaging.

1.6.3 Application in cancer therapy

Cancer has become the leading cause of death worldwide, posing a significant barrier to increasing life expectancy, and is projected to be the primary cause of premature death (before 70 years old) globally in this century [172]. According to the International Agency for Research on Cancer, nearly 10 million people died from cancer in 2020, accounting for almost one in six deaths. The global cancer burden is estimated to reach 28.4 million cases by 2040, a 47% increase from 2020 [172], and is predicted to double by 2070 based on recent trends [173]. Modern photothermal (PT) therapy has been used for cancer treatment since shortly after trials on retinal detachment in the 1960s [174]. In the early stages, lasers were directly used to thermally ablate tumor tissue through irradiation-induced heating [175, 176], a process known as cancer thermal therapy (TT), which is considered a precursor to cancer photothermal therapy (PTT) [174]. However, laser-based cancer TT faced significant limitations, such as accurately targeting malignant cells to selectively heat the tumor without affecting surrounding healthy tissues, limited laser penetration depth, and interference from endogenous substances like chromophores or water. Additionally, the high-power density of the laser raised safety concerns [174, 177].

To address these issues and improve the efficiency of cancer PT, the use of exogenous photosensitive agents was introduced [42, 178-180]. These agents absorb light energy and

convert it into another form of energy for therapeutic effects, thereby reducing the required power density of the light source. The targeting and selectivity of the treatment can also be enhanced if the photosensitive agents provide imaging guidance. Depending on the agents' functions and treatment routes, cancer PT primarily includes photothermal therapy (PTT) [181, 182] and photodynamic therapy (PDT) [183, 184].

Light-based therapies have been used for over 3,000 years in various cultures, including Ancient Egypt, India, and China [185, 186]. A significant development occurred over 100 years ago when Oscar Raab, a German medical student, discovered that a combination of light and acridine could induce cell death, a phenomenon later termed "photodynamic action" [187]. Photodynamic therapy (PDT), which leverages this principle, was officially approved in 1993 in Canada, using Photofrin as a photosensitizer for bladder cancer treatment. PDT involves three key components: light, a photosensitizer, and oxygen. The process begins with the photosensitizer being excited from its ground state to an excited state under specific wavelengths of light. As the photosensitizer returns to its ground state, the energy released is transferred to nearby oxygen molecules, generating reactive oxygen species (ROS) like singlet oxygen (O_2). These ROS can induce oxidative damage to adjacent cells, ultimately leading to cell death [188, 189]. PDT has gained popularity as a cancer therapy due to its high selectivity for tumor cells and lower systemic toxicity [190, 191], resulting in fewer side effects compared to traditional treatments like radiation therapy and chemotherapy[192, 193]. While various nanomaterials, such as gold nanomaterials [194-196]Quantum dots (QDs) [197-201], and polymers [202] have been employed in PDT, they often rely on downshifting luminescence, which requires high-energy light to activate the photosensitizers. This limitation, along with restricted light penetration depth and potential cytotoxicity (as seen with QDs), poses challenges for broader biomedical applications.

Rare-earth nanoparticles (RENPs) offer a promising alternative, meeting the requirements for effective PDT: deeper tissue penetration, lower toxicity, higher stability, and ease of surface modification. RENPs can convert near-infrared (NIR) light into visible light, allowing deeper tissue penetration with less damage to normal cells. In PDT applications, RENPs are typically coated with a shell that serves multiple functions: acting as a matrix for photosensitizers, targeting specific tumor cells, and stabilizing the RENPs. The $NaYF_4$/Er RENP is particularly popular in PDT due to its high efficiency [27, 203-205].

Figure 2.8 Schematic of the design of the versatile photosensitizer based on UCNs [206].

A notable example of RENP-based PDT was demonstrated by Zhang et al [205], who developed a novel approach for treating bladder cancer cells. They coated RENPs with a mesoporous silica shell doped with photosensitizers. An antibody specific to antigens expressed on the target cell surface was covalently attached to the silica shell. This design exploits the spectral overlap between the absorbance of the photosensitizers and the emission of the RENPs, allowing the generation of singlet oxygen (O_2) under NIR irradiation, which in turn kills the target cells.

Photothermal therapy (PTT) harnesses photon energy, converting it into heat to induce irreversible cellular damage, making it an effective treatment for various diseases, particularly cancer tumors [207-209]. In recent years, nanoparticle (NP)-based PTT has garnered significant attention due to its use of nanoheaters (NHs), which are nanoparticles with high light-to-heat conversion efficiencies [108, 210, 211]. The selective incorporation of NHs into cancer cells or tumors enables targeted optical excitation, resulting in localized temperature increases that specifically affect the intended tissues. The efficacy of PTT on cancer tumors is influenced by both the degree of heating and the duration of the treatment [212-215]. Therefore, accurate temperature monitoring during NP-based PTT is crucial to optimize treatment and minimize collateral damage. This has led to a growing interest in developing multifunctional luminescent NPs capable of simultaneous heating and thermal sensing under a single power excitation, which are essential for achieving controlled PTT and subcutaneous studies[96]. Despite the expanding list of systems that can function as both NHs and nanothermometers (NThs), including polymeric NPs, quantum dots, nanodiamonds, metallic NPs, and rare earth-doped NPs, only a few have shown potential for subcutaneous use [216-218]. This limitation arises because most systems operate in the visible spectrum, where tissue penetration is minimal. To overcome this, it is necessary to shift their operational spectral range to the infrared region, within the so-called biological windows (BWs), where tissue absorption and scattering are reduced, allowing for

deeper tissue penetration [219, 220]. Recent studies on the heating effects and light-induced cytotoxicity during in vitro imaging have identified 808 nm as an optimal excitation wavelength. This wavelength minimizes both laser-induced thermal loading of the tissue and intracellular photochemical damage [221, 222]. Additionally, the availability of high-power, cost-effective laser diodes operating at 808 nm enhances their technical feasibility.

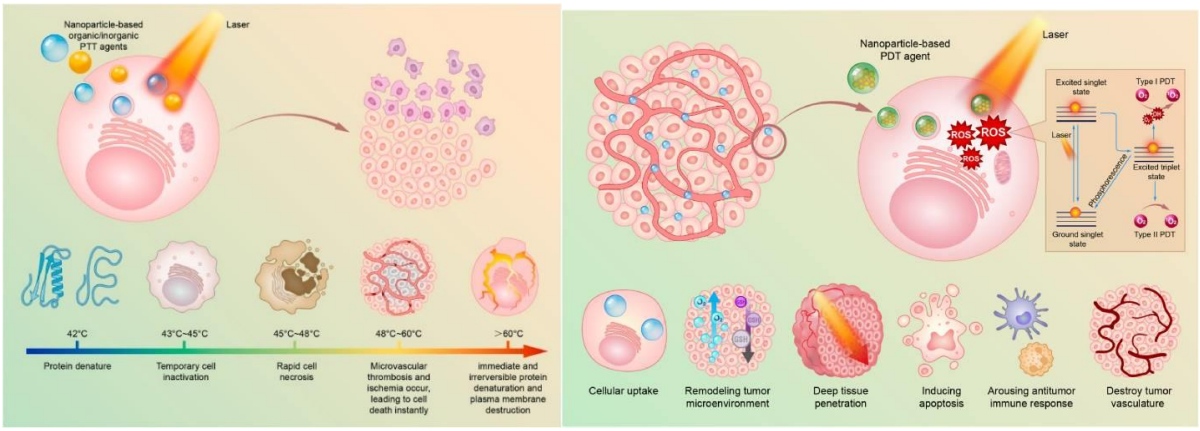

Figure 2.9 Schematic illustration of NPs-based cancer PTT and PDT [223]

Photothermal therapy (PTT) relies on the controlled conversion of light into heat to destroy diseased tissues, such as cancerous cells [179]. During PTT, laser light interacts with photothermal coupling agents, generating heat that is localized to areas where these agents and the laser light intersect. This method offers superior spatial control compared to traditional cancer treatments like surgery, radiotherapy, and chemotherapy, thereby minimizing off-target damage. Current PTT coupling agents include metal nanoparticles (e.g., Au, Ag, Pd, Ge) [224-231], semiconductor nanoparticles (e.g., CuS, CuSe)[231-234]carbon-based nanomaterials (e.g., carbon nanotubes, graphenes), and polymeric nanoparticles (e.g., polyaniline, polypyrrole, poly[3,4-ethylenedioxythiophene]).. Nonetheless, further research is required to integrate diagnostic and imaging functionalities into a single nanosystem for more precise therapy.

1.7 Biological application of Nd^{3+}

Owing to their distinctive properties, including minimized overheating effects and enhanced penetration depth Nd^{3+}-sensitized rare-earth nanoparticles (RENPs), Nd^{3+}-sensitized rare-earth nanoparticles (RENPs) show significant promise for practical applications, especially in biological fields. These applications include tissue sensing, imaging, and cancer therapy. This section will explore the uses of Nd^{3+}-sensitized RENPs, focusing on their roles in downshifting/upconversion

photoluminescence for bioimaging, high-resolution microscopy, deep tissue imaging, and tumor diagnosis and therapy.

Figure removed due to copyrights issues

Figure 3.0 Neodymium excited rare earth nanoparticles [235]

1.7.1 Downshifiting and upconversion photoluminescence for bioimaging

In recent years, photoluminescence imaging has become a crucial technique in biomedical research, divided into downshifting and upconversion imaging. The Nd^{3+} ion is considered an excellent candidate for both types due to its abundant ladder-like energy states and large absorption cross-section around 800 nm. This dual capability allows for the simultaneous achievement of downshifting and upconversion bioimaging.

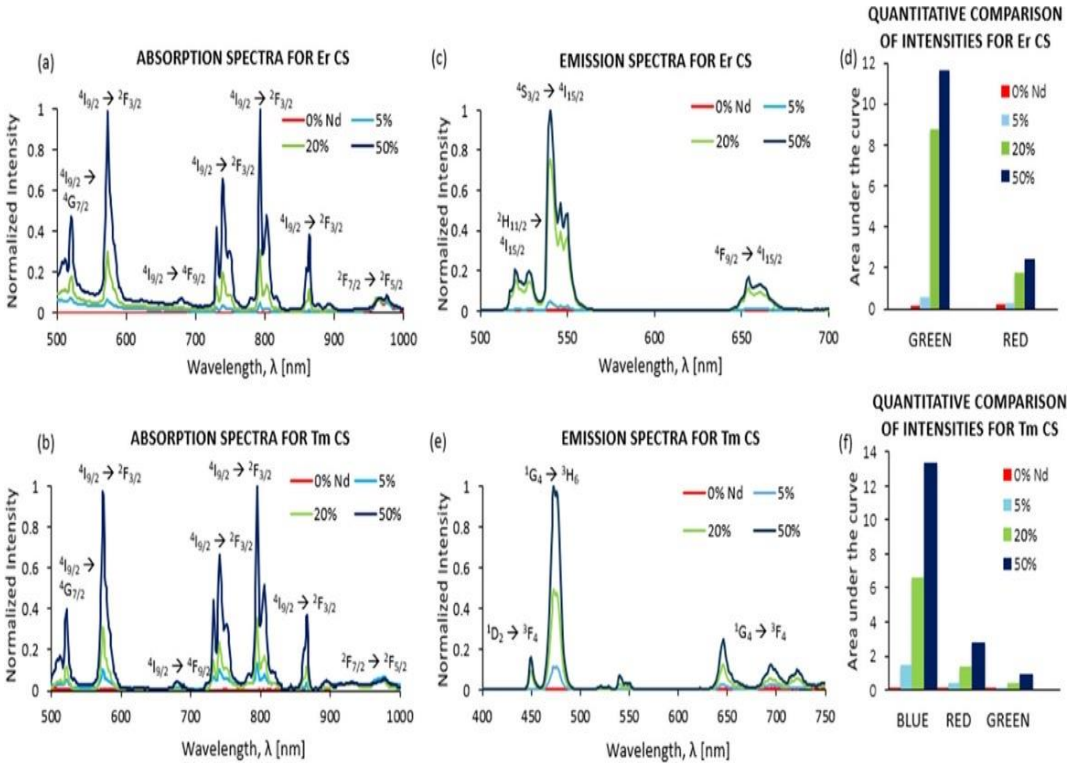

Fig 3.1 Absorption and emission of Er^{3+}- and Tm^{3+}-doped CS NPs with varying concentrations of Nd^{3+} in the shell. Absorption spectra of Er^{3+}-doped CS NPs (a) and Tm^{3+}-doped CS NPs (b) obtained via UV–Vis. (c) Emission spectra of Er^{3+}-doped CS NPs obtained via a fluorimeter equipped with a continuous wave laser at 800 nm and 0.6 W/cm^2. (d) Quantification of the area under the curve. Green emission includes peaks at 522 and 545 nm. Red emission includes a peak at 645 nm. (e) Emission spectra of Tm^{3+}-doped CS NPs. (f) Quantification of the area under the curve. Blue emission includes peaks at 450 and 474 nm. Red emission includes a peak at 650 nm [236]

Although Nd^{3+}-Nd^{3}-sensitized RENPs have been used for imaging since around 2013, earlier studies also explored Nd^{3}-based downshifting imaging [237-239]. For example, Chen et al. demonstrated NIR-to-NIR downshifting photoluminescence peaking at approximately 900, 1050, and 1300 nm using synthesized core@shell $NaGdF_4^{3+}$/$NaGdF_4$ nanocrystals[239]. In their study, in vitro and in vivo NIR-to-NIR PL bioimaging was performed by visualizing the NIR-to-NIR PL at ~900 nm under 740 nm excitation. This method was tested by injecting a nude mouse subcutaneously with 200 µL of 2 mg/mL core@shell $NaGdF_4^{3+}$/$NaGdF_4$ nanoparticles at a depth of about 3mm. The fact that both excitation and PL are within the biological window of optical transparency, along with high quantum efficiency, spectral sharpness, and photostability, makes these nanocrystals highly promising as optical bioimaging probes.

The imaging technique has also gained significant interest due to its potential for background-free imaging and its applications in vitro and in vivo, benefiting from the deep tissue penetration of near-infrared excitation light. Nd^{3+} ions have been used as sensitizers in imaging [59, 240], offering advantages over Yb^{3+}-sensitized UCNPs in bioimaging. For instance, Wang et al. incorporated Nd^{3+} ions as sensitizers to achieve imaging in vivo, creating a core@shell structure to facilitate efficient Nd^{3+}-Yb^{3+}-activator energy transfer [59]. Their experiments involved injecting Nd^{3+}-sensitized RENPs into a nude mouse (20 mg/mL, 50 µL) and demonstrated that these RENPs are effective for in vivo imaging with minimal laser-induced overheating under 808 nm laser excitation. Images from these experiments showed that both 808 nm and 980 nm laser excitations[59] produced comparable photon emissions, confirming the efficiency of 808 nm excitation for in vivo applications.

$$\text{Energy Transfer (ET) efficiency } (\eta) = \frac{nR_0^6}{nR_0^6 + r^6} \quad (1.5)$$

where r is the distance between donor and acceptor, R_0 the Forster radius, and n the number of acceptors. The Förster radius (R_0) can be defined as the distance at which the energy transfer probability is equal to the probability of spontaneous deactivation of the donor (D) (the dyes in this case).

With advancements in nanoscience, intense up- and down-conversion luminescence has been achieved in well-designed core/shell structured Nd^{3+}-sensitized nanoparticles under 808 nm continuous-wave laser excitation, as reported by Zhang's group [241]. Therefore, Nd^{3+}-sensitized RENPs are likely to play an increasingly significant role in in vivo upconversion and downshifting imaging.

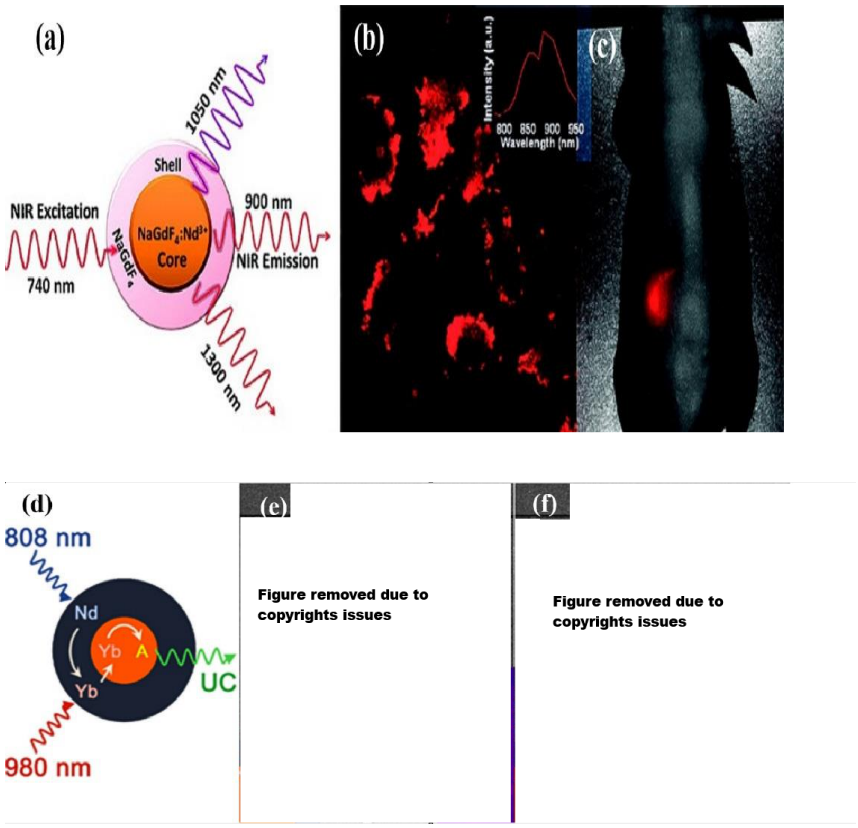

Figure 3.2 (a) The schematic diagram of core@shell $NaGdF_4:Nd^{3+}/NaGdF_4$ nanocrystals under 740 nm excitation, (b) PL images of HeLa cells treated with ligand-free ($NaGdF_4$:3% Nd^{3+})/$NaGdF_4$ nanoparticles. Inset shows localized PL spectra taken from cells (red) and background (black), (c) superimposed image (bright field nude mouse image and spectrally unmixed PL image) [40]. (d) The schematic diagram of Nd^{3+}/Yb^{3+} co-doped shell, (e) and (f) UC imaging of a nude mouse subcutaneously injected with Er@Nd NPs in vivo. The images were obtained with 980 nm laser (e) and 808nm laser (f) irradiation, both with a power density of 200 mW/cm^2. ROIs are denoted in black dot circles. Insert images were infrared thermal image of a nude mouse during continuous (e) 980 nm laser irradiation for 50 s and (f) 808 nm laser irradiation for 300 s [59, 238]

1.7.2 Deep tissue and high-resolution imaging

Nd^{3+}-sensitized rare-earth nanoparticles (RENPs) have shown significant promise for deep tissue imaging, addressing some of the limitations associated with Yb^{3+}-sensitized RENPs. Yb^{3+}-sensitized RENPs are typically excited at 975 nm, a wavelength that experiences relatively high

absorption in biological tissues. This high absorption leads to significant attenuation of the laser beam's intensity as it penetrates deeper into tissues, thereby limiting the effective imaging depth. In contrast, Nd^{3+}-sensitized RENPs are excited at a wavelength of 800 nm, which corresponds to a lower absorption in tissues. This characteristic allows for better penetration and less signal loss at greater depths. The Andersson-Engels group conducted both experimental and theoretical studies to quantify the increased signal depth achieved with Nd^{3+}-sensitized RENPs compared to conventional 975 nm excited Yb^{3+}-sensitized RENPs [242].

Their research involved plotting the signal intensity as a function of sample depth for both types of RENPs. The data were presented on both linear and semilogarithmic scales to illustrate the gain in signal depth for Nd^{3+}-sensitized RENPs, highlighting their superior performance in penetrating biological tissues and providing clearer imaging at greater depths.

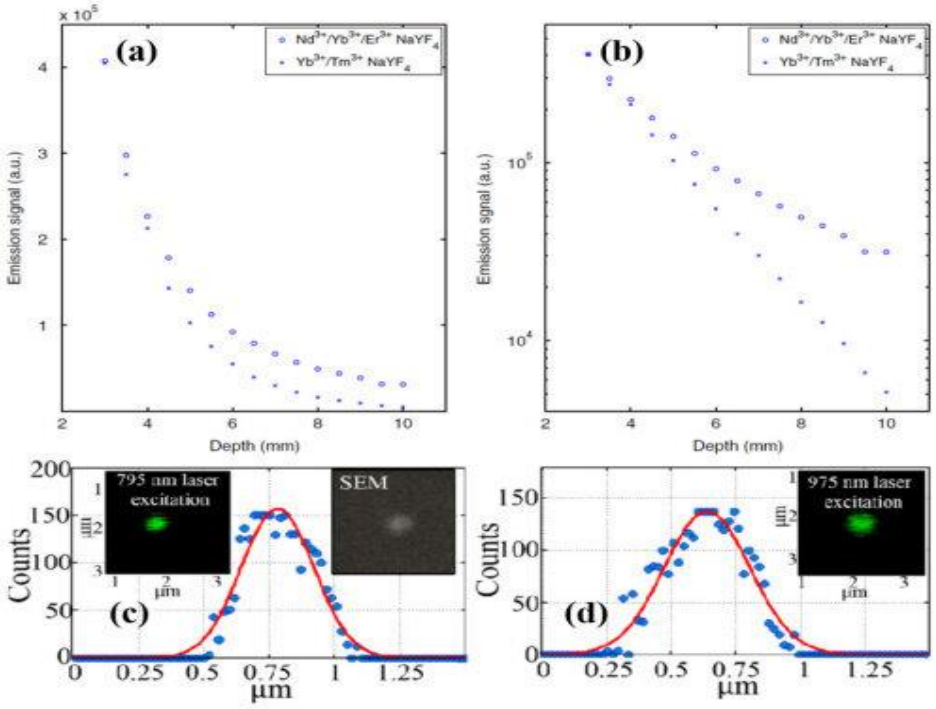

Figure 3.3 (a)-(b) Depth measurements of Yb^{3+}/Tm^{3+} and $Nd^{3+}/Yb^{3+}/Er^{3+}$: (a) a linear scale, and (c) a plot in semilogarithmic scale [44], (c)-(d) Multiphoton imaging of (c) 795 nm-excited RENP (Inset: the SEM image of single RENP on the coverslip) and (d) 975 nm-excited RENP [25], (Reprinted with permission from [242, 243]

Recent advancements in the use of rare-earth nanoparticles (RENPs) as luminescent probes have significantly enhanced spatial resolution in biological imaging. This improvement is particularly notable in multiphoton microscopy (MPM), where the resolution is dependent on the wavelength of the excitation light and the numerical aperture (NA) of the imaging system, as described by the equation:

$$\Delta x \Delta y \approx 1.22\lambda / 2NA(n)^{1/2}. \quad (1.6)$$

Compared to Yb^{3+}-Yb^{3}-sensitized RENPs, which are typically excited at 975 nm, Nd^{3+}-sensitized RENPs, when excited at 800 nm, can offer better resolution in MPM. This is due to the shorter excitation wavelength, which corresponds to improved spatial resolution. Specifically, our group demonstrated that using 795 nm excitation light for Nd^{3+}-sensitized RENPs can enhance the resolution. The full width at half maximums (FWHMs) of the emission profiles were experimentally measured and found to be 345 nm and 425 nm for 795 nm and 975 nm excitations, respectively. These measurements align closely with the theoretical predictions of 342 nm and 420 nm, respectively, indicating a 20% improvement in resolution with 795 nm excitation [243].

1.7.2.1 Nanothermometry

Temperature is one of the most essential state functions widely utilized and studied thermodynamic parameters [244, 245]. An increase in temperature can speed up many chemical reactions, as well as biological and physical processes, both in nature and under laboratory conditions. This makes precise and accurate temperature monitoring crucial in various industrial, scientific, environmental, and biological applications [211, 246, 247]. This is particularly important in modern biomedicine, where continuous and online temperature regulation is employed in medical diagnostics, disease treatment, and general healthcare [248-250]. Temperature measurement has been accomplished in various ways over the centuries. Today, the most common thermometers operate using: (I) liquid solvents or mercury, which rely on thermal expansion properties; (II) the thermoelectric effect in thermocouples; (III) resistance thermometers that measure electrical resistivity changes with temperature; and (IV) pyrometers, which detect infrared radiation emitted by an object and correlate it with temperature [244, 245, 251]. However, most of these methods require a physical or electrical connection with the object being measured, which complicates remote or non-invasive temperature detection, such as within the human body, inside closed mechanical systems, or in microscopic or nanoscale areas [244, 245, 251]. Pyrometers, while not needing direct contact, only measure surface temperature and

are generally less accurate with lower spatial resolution, often providing only rough temperature estimates for larger objects [244-246].

The challenges associated with traditional methods can be addressed through luminescence (nano)thermometry, a technique that enables remote and invasive temperature detection by monitoring temperature-induced changes in certain luminescence properties of optically active probes. This technique allows temperature monitoring in microscopic and nanoscale areas [217, 251-255] by using temperature-dependent steady-state or time-resolved spectroscopic features. These features include the luminescence/fluorescence intensity ratio (LIR/FIR), signal intensity, spectral position of the emission line, full-width-at-half maximum (FWHM) of the band, or luminescence decay/rise times [217, 236, 251-253, 256-258]. Each of these factors can be used as a "thermometric parameter," which can be calibrated to correlate with the temperature of the system [236, 251, 257]. The most used thermometric parameters are LIR/FIR and emission decay time. While LIR/FIR is relatively easy to monitor using standard detection systems, it can be influenced by reabsorption/scattering effects and variations in the on-target excitation power density during real-system measurements, such as in vitro or in vivo experiments [251, 259, 260]. In contrast, emission decay time is less affected by these factors and can provide accurate temperature readings in various environments, although it requires more complex, time-resolved experiments involving pulse excitation sources and fast detection systems [251, 261].

Figure removed due to copyrights issues

Fig 3.4 (A)Absorption spectrum of human skin showing the 1st, 2nd, and 3rd biological windows. (B) Zoom in on the first two optical windows in some biological tissues and fluids. These plots of effective attenuation coefficient (on a logarithmic scale) vs. wavelength show the quantitative relevance of different body substances (oxygenated blood, deoxygenated blood, skin, and fatty tissue) when aiming for deep sub-skin imaging. [261]

Currently, researchers are exploring the combination of different sensing strategies in multi-modal and multi-parameter temperature detection to enhance sensing reliability [251, 262-264]. Luminescent thermometers, or optical temperature probes [236, 251, 262, 264], are typically made from inorganic luminescent materials such as lanthanide (Ln^{3+}) ions, d-block metal ions, quantum dots, or other optically active nanoparticles. Among these, Ln^{3+} doped materials are particularly prominent due to their unique optical properties, including broad-spectrum luminescence from UV to visible and NIR, narrow absorption and emission lines, a rich structure of ladder-like energy levels, and long luminescence decay times. Additionally, Ln^{3+}-doped inorganic materials and nanoparticles can exhibit not only classical down-shifting emission upon UV-visible excitation (Stokes-type process) but also upconversion (UC) emission (anti-Stokes) when excited with low-energy near-infrared (NIR) lasers [251, 252, 265, 266].

One of the most thoroughly explored areas within optical sensing is the detection of temperature within biological systems. This involves remotely monitoring temperature gradients in cells, tissues, and the entire human or animal body, either within a living organism (in vivo) or in laboratory settings (in vitro and ex vivo) [247-249]. Such research is conducted to investigate temperature distribution within tissues, track temperature increases associated with certain

disease conditions (such as tumor growth), and analyze optical heating during laser-induced cell damage, photodynamic therapy, hyperthermia, and controlled drug release therapies [217, 248, 249].

The equation most applied in luminescence thermometry relates to the Boltzmann distribution of electrons in thermal equilibrium, typically occupying excited states separated by a relatively small energy difference (ΔE). This equation is used to fit the measured luminescence intensity ratio (LIR) values and establish a correlation with temperature. It is usually expressed in the following form [251]:

$$LIR = I_2/I_1 = B \exp(-\Delta E/k_{BT}) \quad \text{.....1.7}$$

To quantitatively assess the sensing performance of a luminescent thermometer, both the absolute (S_a) and relative (S_r) temperature sensitivities are typically calculated. These sensitivities are determined using the following equations [251]:

$$S_a = dSP/dT \quad \text{.....1.8}$$

$$S_r = 100\% * 1/SP\ dSP/dT \quad \text{.....1.9}$$

Another crucial parameter in luminescence thermometry is temperature resolution (dT), which refers to the uncertainty in temperature measurement. This uncertainty depends on the precision with which the spectroscopic parameter (dSP) is determined, which is influenced by the signal-to-noise ratio. The temperature resolution can be theoretically estimated using the following general formula [251]:

$$\delta T = 1/S_r\ \Delta SP/SP \quad \text{.....2.0}$$

One of the most effective ions for nanothermometry utilizing down-shifted luminescence is Nd^{3+}. Due to the spectral overlap of their emission bands with the transparency windows of human tissues, nanoparticles (NPs) doped with Nd^{3+} ions are emerging as significant sub-tissue optical probes. In most studies, an excitation wavelength of 808 nm is used, and the intensity ratio between Stark levels (crystal-field components) within the 880–1060 nm range is commonly employed. Additionally, Nd^{3+} ions can emit longer wavelength near-infrared (NIR) light, particularly around 1320 nm. Unlike upconversion nanoparticles (UCNPs), both excitation and emission for Nd^{3+} ions fall within the NIR spectral region's highest transparency window. Furthermore, the Stokes emission quantum yield (QY) of Nd^{3+} is at least an order of magnitude higher than that of upconversion, making Nd^{3+}-doped NPs highly promising for biomedical applications. These NPs facilitate temperature sensing and bioimaging in the NIR range through simultaneous excitation

within the first biological window (BW) around 808 nm. Experimental studies by Savchuk et al., Quintanilla et al., and Cantarano et al. have demonstrated such applications.

Figure removed due to copyrights issues

Fig 3.5 Luminescence spectra of $LiLuF_4:Nd^{3+}@LiLuF_4$ at 20 and 45 °C with close-ups on the Nd^{3+} emission bands corresponding to A – $^4F_{3/2}$-$^4I_{9/2}$, B –$^4F_{3/2}$-$^4I_{11/2}$, and C – $^4F_{3/2}$-$^4I_{13/2}$ radiative transitions. Shaded areas represent integration ranges from which intensity values In and Im (n, m 1, 2, and 3) can be used for calculations of thermometric parameters Dk (k = 1, or 2) [267]

1.7.3 Cancer Therapy

RENPs have demonstrated significant potential in bioimaging, tumor diagnosis, and therapy, particularly through applications like photodynamic therapy (PDT). Traditional RENP-based PDT systems often use 980 nm excitation, which is absorbed by water, potentially causing overheating. In contrast, Nd^{3+}-sensitized RENPs, which operate under 800 nm excitation, offer a safer and more efficient alternative. For instance, Wang et al. designed a core@shell@shell nanostructure, $NaYF_4$/Ho@$NaYF_4$@$NaYF_4$, optimized for PDT and fluorescence imaging using 808 nm light. This configuration minimized heating and enhanced PDT efficacy, as demonstrated in Hela cells[268]. Zhu et al. developed a similar platform using $NaYbF_4$@$NaGdF_4$/Er@$NaGdF_4$ nanoparticles, loaded with chlorin and folic acid, also for imaging and PDT under 808 nm excitation[269]. Beyond PDT, Nd^{3+}-sensitized RENPs have applications in photothermal therapy [270, 271] and tumor diagnosis [272, 273]. Xu et al. proposed multifunctional nanoparticles, co-doped with Nd^{3+}/Yb^{3+}, capable of acting as luminescent nanothermometers and nanoheaters, suggesting their use in photothermal therapy [271]. In tumor diagnosis and drug delivery, Lin's group synthesized core@shell Nd^{3+}-sensitized $NaYF_4$/Nd/Er@$NaYF_4$@$mSiO_2$ nanoparticles

[272]. These nanoparticles, loaded with the anticancer drug doxorubicin (DOX), showed enhanced therapeutic efficacy compared to pure DOX. In vivo studies demonstrated that tumors treated with DOX-loaded nanoparticles were significantly smaller than those in control groups, underscoring the potential of this approach for effective cancer treatment [272].

Figures removed due to copyrights issues

Figure 3.6 (a) Scheme of core-shell nanoparticle modified with Rose Bengal (RB); (b) Proposed energy transfer mechanisms of nanoparticles with a high concentration of Nd_3þ ions in the thin active layer; (c) NIR emission spectra of $NaYF_4$:Yb/Ho(8 mol%/1 mol%) nanoparticles and $NaYF_4$:Yb/Ho(8 mol%/1 mol%)@$NaYF_4$:Nd (20 mol%) nanoparticles under excitation at 808 nm; (d) Room-temperature upconversion emission spectra of $NaYF_4$: Yb/Ho (8 mol%/1 mol%) nanoparticles and $NaYF_4$:Yb/Ho(8 mol%/1 mol%)@$NaYF_4$:Nd (20 mol%)@$NaYF_4$ nanoparticles under excitation at 808 nm. The inset shows digital photographs of the emission of the final core-shell-shell nanoparticles (Adopted from Ref. 51).

1.7.4 Challenges

Significant advancements in the control of size, shape, and phase of RENPs have been made using various synthesis methods, greatly expanding their applications in the biological field. Besides their successful use in biological labeling and fluorescence imaging, RENPs have garnered increasing interest in nanothermometers because of their use in high-resolution temperature sensing in biological and material science applications.

However, several challenges remain. Firstly, because of the low thermal sensitivity RENPs display, small temperature changes will bring about only a small difference in photoluminescence properties. This can limit their application in biological tissues. Secondly, RENPs are typically not water-dispersible, and one-pot synthesis methods for water-soluble RENPs often result in broad size distributions and poor shapes. Although surface modification can improve water solubility and biocompatibility, these procedures are time-consuming and may reduce luminescence efficiency. Also, extended exposure to high-intensity lasers can cause photobleaching, which could affect long-term temperature monitoring applications. Nonetheless, we believe that RENP-

based techniques will be widely utilized and will address some of today's most challenging problems [8]

Although Nd^{3+}-sensitized RENPs have garnered significant attention across various fields due to their unique optical and chemical properties, several challenges remain in their development. Firstly, the emission intensity and spectra of Nd^{3+}-sensitized RENPs are still inadequate, necessitating improvements in quantum yield and emission wavelength tuning through careful design and optimization of their structure. As the complexity of Nd^{3+}-sensitized RENP structures, particularly core/shell structures, increases, traditional synthesis methods are becoming insufficient to meet practical needs. Therefore, new synthesis methods are required to prepare complex multi-layered Nd^{3+}-sensitized RENPs. Additionally, while notable advances have been made in the synthesis and multifunctionalization of these nanoparticles, understanding the complex interactions in biological systems, such as non-specific binding and loss of biological activity at the bio/nano interface under physiological conditions, remains challenging. Lastly, despite reports of low toxicity of rare-earth nanoparticles in both in vitro and in vivo experiments, the potential toxicity of fluoride ions at higher doses cannot be overlooked [274-276].

1.8 Thesis objectives and contribution

Achieving a bio benign wavelength excitation is possible by introducing Neodymium (Nd^{3+}) into Ytterbium (Yb^{3+}) doped rare-earth nanoparticles. Neodymium (Nd^{3+}) is an effective dopant because of its strong absorption in the NIR region, deep tissue penetration, reduced autofluorescence, and its great application in accurate temperature monitoring (Nanothermometry), photothermal, and photodynamic therapy. By using Neodymium (Nd^{3+}) together with Ytterbium (Yb^{3+}) in lanthanide-based RENPs, it's possible to shift the absorption from 980 nm to 800 nm, a range where water does not absorb light. High concentrations of Nd^{3+} are advantageous because they enhance both absorption and emission. In biological applications, heavily doped RENPs can efficiently convert NIR light to visible light, activating photosensitizers to generate reactive oxygen species (ROS) that kill cancer cells. The enhanced emission and functional capabilities of these heavily doped RENPs ensure effective temperature sensing while reducing the damage to healthy cells. From the literature review, most of the published work focused on doping levels below 10 mol%, with a few studies reporting up to 30 mol% [277-280]. The difficulty in getting good morphology for heavily doped rare-earth nanoparticles (RENPs) is due to increased nucleation/growth rates, lattice strain/defects, non-

homogeneous dopant distribution and temperature sensitivity. This has resulted in non uniform shape and sizes which in return affects its application in cancer therapy amongst others.

Hence the objectives of my thesis are stated below:

1. Optimized synthesis procedure

In the first part of this project, we focused on the design and optimized synthesis of heavily doped $LiYbF_4$: Nd^{3+} (60%) 2.5 mmol rare-earth nanoparticles. The objective is to get good morphology for heavily doped rare-earth nanoparticles by optimizing different parameters such as the reaction time, temperature and concentration of the ligands used for their application in cancer therapy. Good morphology enhances downshifting efficiency and effective treatment of cancerous tissues while minimizing damage to healthy cells.

2. Enhanced optical properties

Going further, we tried enhancing the optical efficiency by creating a core/ inert shell structure, which is composed of no dopants in the shell of the heavily doped $LiYbF_4$:Nd^{3+}(60%)@$LiYF_4$. The objective is to reduce surface defects and impurities, improve energy transfer between the sensitizer and activator ions, while reducing concentration quenching to improve the overall luminescence efficiency. The optical properties were measured and recorded.

1.9 Thesis organization

There are five parts to this thesis, and the organization is outlined below:

Chapter 1 introduces the background of the study, research problems, motivation, aims & objectives of this work.

Chapter 2 describes the materials used in the synthesis and the characterization techniques employed to check the morphology and luminescence properties of $LiYbF_4$:Nd^{3+} (60 mol%), 2.5 mmol core, and $LiYbF_4$@$LiYF_4$ (2 mmol).

Chapter 3 discusses the experimental details of the synthesis method used (thermal decomposition method via hot injection), stabilization techniques, and results obtained for the core $LiYbF_4$:Nd^{3+} (60%) 2.5 mmol. It also discusses the experimental details of optimizing the luminescence properties by creating a core-shell structure $LiYbF_4$@$LiYF_4$ (2 mmol), stabilization, and results obtained.

Chapter 4 discusses the results obtained from characterization and luminescence properties.

Chapter 5 briefly summarizes the findings of this work, its application, challenges, and outlook.

2 MATERIALS AND CHARACTERIZATION

In this chapter, we will highlight the general synthesis method used for synthesizing $LiYbF_4$: Nd^{3+} (60%) 2.5 mmol and $LiYbF_4$@$LiYF_4$ and the characterization technique employed.

2.1 Materials

Y_2O_3 (REacton, 99.999%), Yb_2O_3 (REacton, 99.998%), Tm_2O_3 (REacton, 99.997%), Nd_2O_3 (REacton, 99.997%) trifluoroacetic acid (99%), 1-octadecene (ODE, 90%), and oleic acid (OA, 90%) were purchased from Alfa Aesar (USA). Lithium trifluoroacetate (98%) and oleylamine (OM, 70%) were obtained from Sigma-Aldrich (USA). All chemicals were used as received.

2.1.1 1-Octadecene (ODE)

1-Octadecene was used as a solvent in the synthesis of $LiYbF_4$ and $LiYF_4$. It is used because of its ability to produce high-quality, monodisperse nanoparticles with controlled size and morphology. It has a high boiling point that allows for better control over the reaction temperature which is important for the thermal decomposition of precursors and formation of nanoparticles.

2.1.2 Oleic acid (OA)

Oleic acid acts as a surfactant, stabilizer, and ligand, that collectively contribute to producing high-quality, monodisperse nanoparticles with controlled size and shape. It acts as a surfactant preventing the nanoparticles from aggregating which leads to uniform particle size and shape. It also acts as a ligand that protects the surface of the nanoparticles from oxidation and other chemical reactions. It influences the nucleation and growth rates of nanoparticles during the synthesis process.

2.1.3 Oleylamine (OM)

Oleylamine acts as a co-surfactant alongside oleic acid, providing additional stabilization to the nanoparticles preventing aggregation which leads to better control of the nanoparticle size and shape. It also acts as a mild reducing agent in the synthesis process which helps in the reduction of metal precursors to their metallic state that aids the formation of certain types of nanoparticles.

2.1.4 Trifluoroacetic (TFA) Acid

TFA helps to solubilize metal precursors, particularly rare-earth metal salts, which are often used in the synthesis process ensuring a more uniform distribution of reactants. It serves as a coordinating ligand for achieving uniform nucleation and growth of nanoparticles. It acts as a capping agent preventing agglomeration. It influences the pH and overall reaction environment.

2.1.5 Ytterbium oxide (Yb_20_3)

Ytterbium acts as the sensitizer. The Yb^{3+} ions efficiently absorb near-infrared (NIR) light due to their high absorption cross-section at a particular wavelength. Once they have been excited, they transfer their energy to activator ions present in the host lattice.

2.1.6 Lithuim trifluoroacetate (LiF_3)

Lithium is the host lattice in the synthesis. It is the crystalline structure in which the sensitizer and activator ions are embedded. The small size and high charge density of Lithium ions helps in the creating a stable and robust lattice that can host the Yb^{3+} sensitizer and activator ions.

2.1.7 Neodymium oxide (Nd_2O_3)

Neodymium acts as the dopants because of suitable energy level. Neodymium helps in producing nanoparticles that can emit light in a specific color range that is useful in bioimaging, displays and sensors.

2.1.8 Yttrium oxide (Y_2O_3)

Yttrium forms a protective shell around the core of the UCNPs. It acts as a barrier to prevent energy transfer from the core dopants to quenchers in the surrounding environment, thus maintaining high luminescence efficiency. The presence of a yttrium shell helps in controlling the overall size and morphology of the nanoparticles. The thickness of the shell is important for optimizing the optical properties and ensuring uniformity in particle size.

2.2 Characterization Technique

2.2.1 Transmission Electron Microscopy (TEM)

Rare-earth Nanoparticles (RENPs) were suspended and diluted with 4 mL of hexane. The resulting mixture was drop-cast onto carbon-coated copper grids and left to dry. Cross-sectional images of the synthesized RENPs were captured using an FEI Tecnai G2 Sphera microscope operating at 120 kV. The size of the NPs was analyzed by measuring the diameters at 100,000× magnification using ImageJ. The measurements were then exported to Origin Pro to calculate the average size and standard deviation.

Transmission Electron Microscopy (TEM) is a powerful imaging technique that uses a beam of electrons to create an image of a specimen. The electrons pass through the sample and are scattered depending on the density and composition of the material. TEM can achieve very high resolution, allowing researchers to see fine details at the atomic or molecular level.

TEM can achieve resolutions below 1 nm, allowing for the visualization of atomic structures. It also offers magnification ranges from tens to hundreds of thousands of times, far exceeding that of light microscopes. Various contrast mechanisms, such as diffraction contrast, phase contrast, and mass-thickness contrast, help in differentiating features within the specimen.

TEM Workflow

1. **Sample Preparation**: The specimen is prepared as an ultra-thin section (typically less than 100nm thick) to allow electrons to pass through.
2. **Loading the Sample**: The specimen is mounted on the sample holder and inserted into the TEM column.
3. **Creating the Electron Beam**: The electron gun generates a focused electron beam directed towards the sample.
4. **Imaging**: Electrons interact with the sample and are transmitted through it, with the transmitted electrons forming an image that is magnified by the objective and projector lenses.
5. **Image Detection**: The transmitted electron image is captured by the detector system, and the data is analyzed and recorded.

2.2.1.1 X-ray Diffractometer (XRD)

The qualitative and quantitative phase analysis of the sample was performed with a method known as X-ray powder diffraction. The x-rays that are produced help illuminate the sample, and then are diffracted by the sample phase, moving further into the detector. The intensity and diffraction data are measured by shifting the sample and detector to change the angle (2θ), which is the angle between the incident and diffracted beams**.**

2.2.1.2 Scanning Electron Microscope (SEM)

The structural composition of the sample was also measured using an SEM machine. The beams of electrons from the machine were used to create images of the surface of the sample revealing its crystalline structure, composition and texture.

2.2.1.3 Energy Dispersive X-ray Analysis (EDX)

The elemental information about the samples was analysed using an EDX together with an SEM. EDX uses electron beams hitting the inner shell of an atom and displacing the electron from the shell, releasing X-rays that measure the signal and identifies each element that are present in the sample using a software.

2.2.2 Photoluminescence (PL) Spectroscopy

Photoluminescence spectroscopy (PL spectroscopy) is an optical technique used to study the electronic and structural properties of materials by analyzing the light emitted from a sample after it has absorbed photons. In my experiment, steady state PL spectroscopy of samples was taken at an excitation wavelength of 808 nm.

2.2.2.1 Principles of Photoluminescence Spectroscopy

1. **Excitation**: When a material is exposed to light (usually from a laser or a lamp) of sufficient energy, it absorbs photons, and electrons in the material are excited from the ground state to higher energy states (excited states).
2. **Relaxation**: The excited electrons are not stable and will relax back to the ground state. During this process, they may lose some energy through non-radiative processes (e.g., heat) before returning to the ground state.
3. **Emission**: When the excited electrons return to the ground state, they emit photons. The energy (and hence the wavelength) of these emitted photons is characteristic of the difference in energy levels between the excited state and the ground state.

2.2.2.2 Functioning principle of Photoluminescence Spectroscopy

1. **Illumination**: The sample is illuminated with light from the excitation source. The photons from the light source excite electrons in the material to higher energy states.
2. **Emission Collection**: As the electrons relax back to their ground state, they emit photons. The emitted light is collected and directed towards the emission monochromator.
3. **Spectrum Analysis**: The emission monochromator disperses the emitted light into its constituent wavelengths. The detector measures the intensity of light at each wavelength, producing a photoluminescence spectrum.

4. **Data Interpretation**: The resulting spectrum provides information about the electronic structure, energy levels, and other properties of the material. Peaks in the spectrum correspond to specific electronic transitions within the material.

3 METHODOLOGY

3.1 Core $LiYbF_4:Nd^{3+}$ (60% and 2%) 2.5 mmol

3.1.1 Precursor Preparation

For the synthesis of the core using first nuclei synthesis method, 2.5 mmol of rare earth (RE) trifluoroacetate precursors were made by mixing stoichiometric quantities of RE_2O_3 with (RE = Yb, Nd) with 5 ml of trifluoroacetic acid and 5 ml distilled water in a 100 ml three-neck round-bottom flask.

In the precursor preparation of $LiYbF_4:Nd^{3+}$ (60%):

Yb_2O_3 (40%): 0.5 mmol (197.04 mg), Nd_2O_3 (60%): 0.75 mmol (252.36 mg) were used. The slurry was refluxed under vigorous conditions at 80 °C until clear. The temperature was lowered to 60 °C to evaporate the solvent overnight. The obtained solid dried product was used as a precursor for the synthesis.

In the precursor preparation of $LiYbF_4:Nd^{3+}$ (2%)

Yb_2O_3 (98%): 1.23 mmol (482.75 mg), Nd_2O_3 (2%): 0.025 mmol (8.41 mg) were used. The slurry was refluxed under vigorous conditions at 80 °C until clear. The temperature was lowered to 60 °C to evaporate the solvent overnight. The obtained solid dried product was used as a precursor for the synthesis.

3.1.2 Size-Controlled Synthesis of $LiYbF_4:Nd^{3+}$ RENPs (60% and 2%)

$LiYbF_4:Nd^{3+}$ (60% and 2%) RENPs were synthesized using the thermal decomposition method that has been discussed in the literature review. The size of the RENPs was controlled by mixing different volumetric ratios of oleic acid/oleylamine (OA/OM). Two different synthesis approaches were used for the synthesis and stabilization of the RENPs they are hot injection and one-pot synthesis.

3.1.3 Synthesis of $LiYbF_4:Nd^{3+}$ (60% and 2%) Core RENPs via Hot-injection Method

For the hot-injection method, two distinct solutions were prepared separately. In a 100 mL three-neck round-bottom flask, Solution A was created by combining 14 mL of a selected OA/OM mixture with 14 mL of ODE. Solution B was prepared by mixing 2.5 mmol of lithium trifluoroacetate, pre-dried RE precursors, 6 mL of the OA/OM mixture, and 6 mL of ODE. OM was added to Solution B only after the precursors were fully dissolved under vacuum in a pure

OA/ODE mixture. Both solutions, A and B, maintained the same OA/OM/ODE composition. Each solution was stirred and degassed under vacuum at 110 °C and 125 °C, respectively, for 30 min. Under an Ar atmosphere, the temperature of Solution A was then increased to 315 °C. When Solution A stabilized at the desired temperature, Solution B was introduced into Solution A using a pump-syringe system at an injection rate of 1.5 mL/min. After the injection, the synthesis procedure continued as in the one-pot method: a reaction time of 1 h was maintained. The solution was then allowed to cool to room temperature while maintaining magnetic stirring under an Ar atmosphere.

3.1.4 Stabilization of $LiREF_4:RE^{3+}$ Core

To stabilize the core, we use one pot synthesis method. In a 100 ml three-neck round bottom flask, half of the synthesized core was measured and topped up with equal amounts of OA and ODE to make a total volume of 50 ml. The solution was stirred and degassed under vacuum at 110 °C for 30 min. Under Ar atmosphere, the temperature of the solution was raised to 330 °C for different reaction times of 2 h, 2 h 15min, and 2 h 30 min for 60% Nd and 1 h for 2% Nd. The solution was then allowed to cool to room temperature while maintaining magnetic stirring under Ar atmosphere. The oleate-capped RENPs were precipitated by adding ethanol and collected by centrifugation at 5400 RCF for 15 min. The RENPs were then washed twice with a hexane/ethanol mixture in a 1:4 volume ratio, followed by another round of precipitation via centrifugation. Finally, the oleate-capped RENPs were redispersed in hexane for storage and further characterization.

3.2 Core/Shell $LiYbF_4:Nd^{3+}@LiYF_4$ (60% and 2%)

3.2.1 Precursor Preparation

For the synthesis of the core/shell using the first nuclei synthesis method, 2 mmol of rare earth (RE) trifluoroacetate precursors were made by mixing stoichiometric quantities of RE_2O_3 (RE = Y) with 5 ml of trifluoroacetic acid and 5 ml of distilled water in a 100 ml three-neck round-bottom flask.

In the precursor preparation of $LiYF_4$ Shell:

Y_2O_3:1mmol (225.8 mg) used. The slurry was refluxed under vigorous conditions at 80 °C until clear. The temperature was lowered to 60 °C to evaporate the solvent overnight. The obtained solid dried product was used as the precursor for the synthesis.

3.2.2 Synthesis of Core/Shell $LiYbF_4:Nd^{3+}/LiYF_4$ (60% and 2%)

Core/shell RENPs were synthesized by epitaxially growing the shell layer, with appropriate precursors injected into the pre-formed core solution using a pump-syringe system. Solution A was prepared in a 100 mL flask by dissolving 0.5 mmol of core material in an OA/ODE solution, with equal volumes of OA and ODE making up a total of 20 mL. Solution B consisted of 2 mmol of shell precursors mixed with 10 mL of OA and 10 mL of ODE. Both solutions were stirred and degassed under vacuum at 110 °C for 30 min. Under an Ar atmosphere, the temperature of Solution A was increased to 315 °C, and 7 mL of Solution B was injected at a rate of 1.5 mL/min at a time interval of 40 min. After the injection was completed, the subsequent steps, cooling, washing, and storage, followed the previously described procedures.

3.2.3 Surface Modification (Ligand Stripping)

25 mg (5 ml) of the nanoparticle was dispersed in 5 ml of hexane. Then, 5 mL 0.01 mol/L N_0BF was added to the dispersed sample. The mixture was then stirred for 20 min at room temperature. After 20 min, the mixture was centrifuged for 10 min at 7500 RPM. It was washed once with hexane/toluene in a ratio of 1:1. It was redispersed in 2 mL of de-ionized water. Ligand stripping was carried out to make the nanoparticles dispersible in water for biomedical applications.

3.2.4 Nanothermometry Calculations

The nanothermometer parameters were calculated using the Brites et al method [216]. Photoluminescence Intensity (PL) ratio (Δ) was calculated by taking the ratio between the integrated intensities I_1 and I_2 at each temperature value. The relative thermal sensitivity (S_r) was also calculated. All formulas in the calculation have been explained in the literature review.

4 RESULT AND DISCUSSION

4.1 Structure, morphology, and composition of the core $LiYbF_4:Nd^{3+}$ (60% and 2%) for different reaction times and temperatures.

We carried out TEM, SEM, and XRD at different reaction times and doping concentrations of Nd^{3+}. This was done to obtain the optimal temperature and reaction time while carrying out the first nuclei synthesis. The report in the literature states that increasing the temperature and reaction time of heavily doped rare-earth nanoparticles (RENPs) can result in uniformly shaped and evenly distributed nanoparticles[281, 282]. From the results obtained, we observe that increasing the temperature beyond a particular time resulted in lattice distortion for heavily doped $LiYbF_4:Nd^{3+}$ (60%) RENPs.

For $LiYbF_4:Nd^{3+}$ (2%), **Figure 4.1** reaction time was 1 h, and reaction temperature was 330 ^oC

For $LiYbF_4:Nd^{3+}$ (60%), **Figure 4.2** reaction time was 2 h, and reaction temperature was 330 ^oC

For $LiYbF_4:Nd^{3+}$ (60%), **Figure 4.3** reaction time was 3 h, and temperature was 315 ^oC

For $LiYbF_4:Nd^{3+}$ (60%), **Figure 4.5** reaction time was 2 h and 15 min, and temperature was 315^oC

For $LiYbF_4:Nd^{3+}$ (60%), **Figure 4.4** reaction time was 2 h and 30 min, and temperature was 315^oC

The standard reaction time of 1 h for 2% Nd yielded a uniform morphology with a tetragonal shape. Increasing the reaction time from 1 h to 2 h for 60% Nd resulted in uniform morphology with a hexagonal shape. Further increasing the reaction time from 2 h – 2 h 15 min and 2 h 30 min and reducing the reaction temperature from 330 ^oC to 315 ^oC resulted in a non-uniform morphology for 60% Nd, and the particle size became smaller as seen in the figures below. Table 2 summarizes the different diameters for the core and shell for different doping percentages.

Figure 4.1 shows the TEM images and size distribution graph of $LiYbF_4:Nd^{3+}$ (2%) for a reaction time of 1 h.

TEM imaging was used to verify the morphology of the core $LiYbF_4:Nd^{3+}$(2%) RENPs. The diameter of the core is approximately 24 nm, and we observe that the mean particle size has become smaller, and the RENPs are evenly distributed with a tetragonal structure.

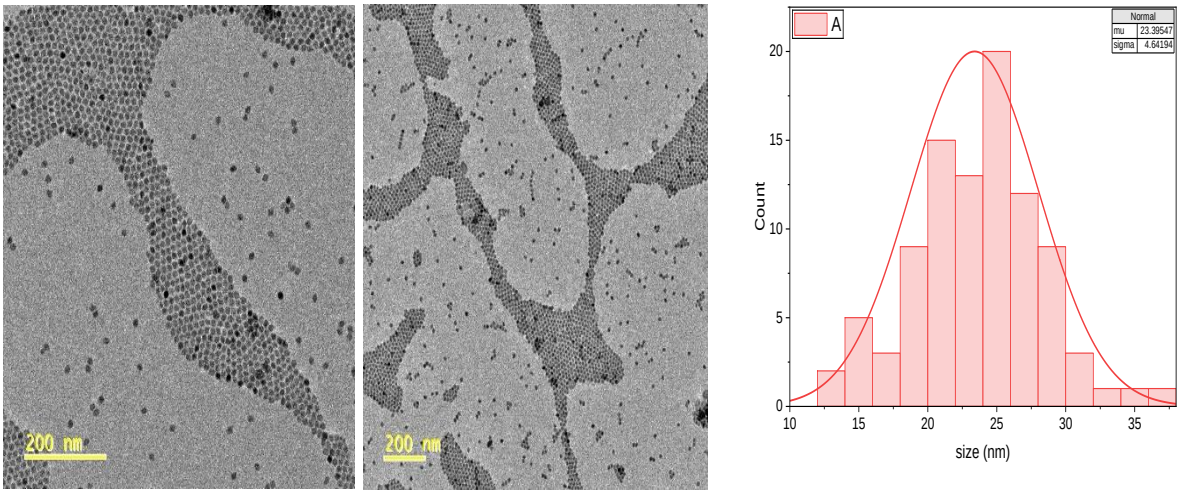

Figure 4.1 TEM images and size distribution graph of LiYbF4:Nd^{3+} (2%) for a reaction time of 1 h.

Figure 4.2 shows the TEM images at different magnifications and the size distribution graph of $LiYbF_4:Nd^{3+}$ (60%) for a reaction time of 2 h.

As with the 2% sample, TEM imaging was used to verify both the morphology of the core $LiYbF_4:Nd^{3+}$ (60%) RENPs and their particle size distribution. The diameter of the core is approximately 28 nm. We observe that the particles are evenly distributed with a hexagonal structure. The TEM images and size distribution graph can be seen in figure below.

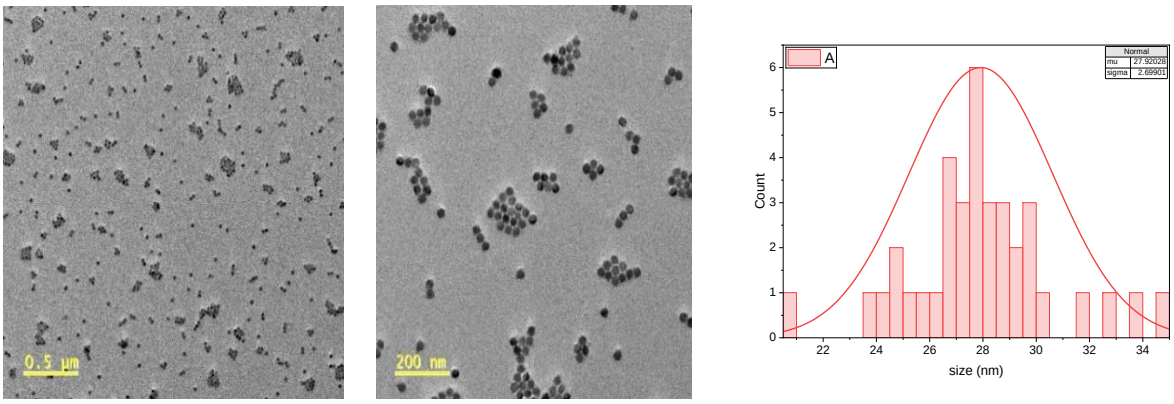

Figure 4.2 TEM image and size distribution graph of $LiYbF_4:Nd^{3+}$ (60%) for a reaction time of 2 h

4.1.1 Structure, morphology, and composition of the core $LiYbF_4:Nd^{3+}$ (60%) for reaction time above 2 h.

We opted to change the reaction parameters by increasing the reaction time and reducing the reaction temperature to see the effect it would have on the structure of the core. TEM imaging was used to verify the morphology of the core $LiYbF_4:Nd^{3+}$ (60%) RENPs. We observe that the RENPs are not uniformly shaped and evenly distributed. On the other hand, their sizes are much smaller, at approximately 8 nm, as compared to maintaining a reaction time of 2 h. Thus, we concluded that increasing reaction time above 2 h would not result in uniformly shaped and well-dispersed RENPs but it would result in smaller sizes. This could be due to lattice strain as a result of the heavy doping of Nd^{3+}. It is known that Nd^{3+} has a very large ionic radius compared to other lanthanides, especially Yb^{3+}, which is part of the RENP matrix. We opted to forego shelling process and focus only on $LiYbF_4:Nd^{3+}$ (2%) and $LiYbF_4:Nd^{3+}$ (60%) prepared within the 2 h reaction time. Only these two core samples were used to grow undoped $LiYF_4$ shells. Figures 4.4 – 4.6 show the TEM images (at different magnifications) and the particle size distributions of the core only $LiYbF_4:Nd^{3+}$ (60%) RENPs prepared at a reaction times of 3 h, 2 h 30 min, and 2 h 15 min, respectively.

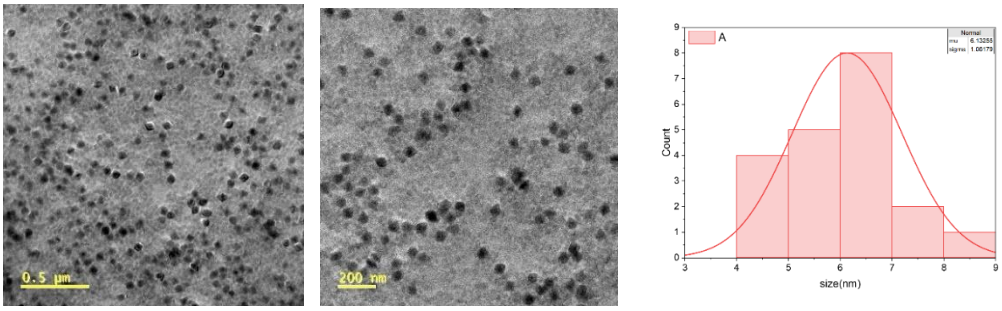

Figure 4.3 TEM images and size distribution graph of $LiYbF_4:Nd^{3+}$ (60%) for a reaction time of 3 h

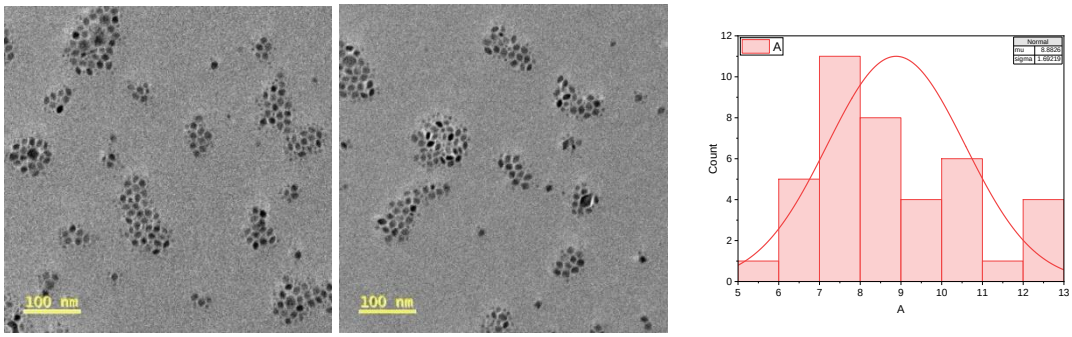

Figure 4.4 TEM images and size distribution graph of $LiYbF_4:Nd^{3+}$ (60%) for a reaction time of 2 h 30 min

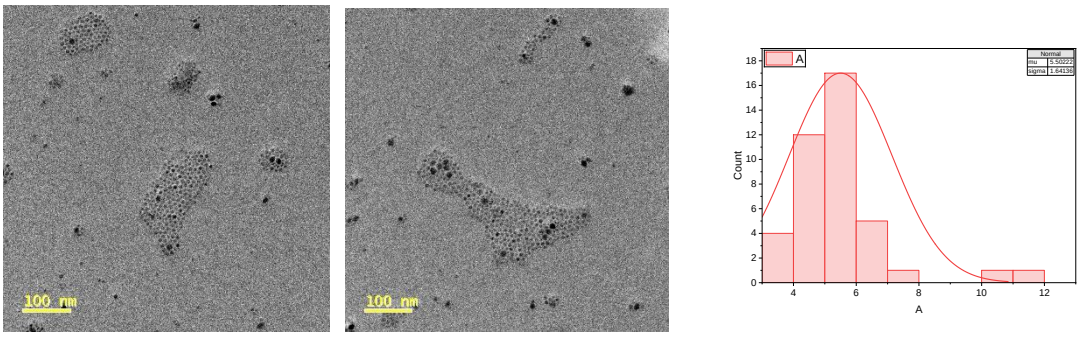

Figure 4.5 TEM image and size distribution graph of $LiYbF_4:Nd^{3+}$ (60%) for a reaction time of 2 h 15 min

4.2 Morphology characterization of the core/shell $LiYbF_4:Nd^{3+}@LiYF_4$ (60% and 2%)

TEM imaging was used to observe the morphology of core/shell $LiYbF_4:Nd^{3+}@LiYF_4$ (60%) RENPs as well as the average particle size distribution. Figure 4.7 shows the TEM images and particle size distribution of $LiYbF_4:Nd^{3+}@LiYF_4$ (60%) at different magnification for a reaction time of 2 h. We observe that the average particle diameter of the core/shell RENPs (60%) is approximately 34 nm indicating that the shell growth is between 6 nm. The RENPs are evenly distributed with a hexagonal structure given the controlled synthesis.

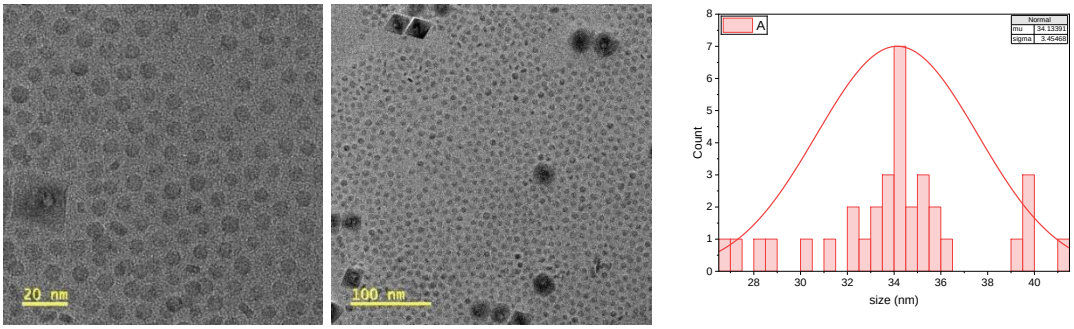

Figure 4.6 TEM images and size distribution graph of $LiYbF_4:Nd^{3+}@LiYF_4$ (60%) for a reaction time of 2 h

We investigated the composition of the surface of $LiYbF_4:Nd^{3+}@LiYF_4$ (60%) RENPs at different magnifications (Figure 4.8) with a scanning electron microscope (SEM) and we observed uniformity with the TEM images.

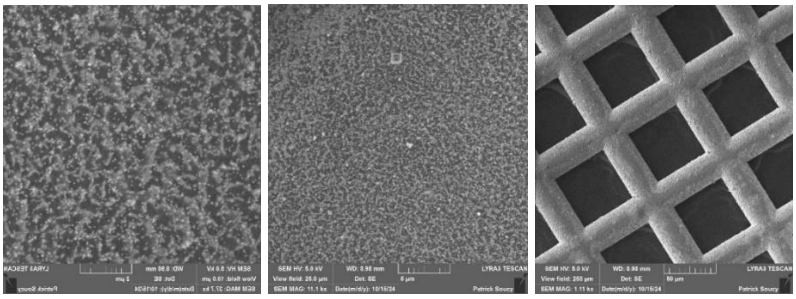

Figure 4.7 SEM image of $LiYbF_4:Nd^{3+}@LiYF_4$ (60%) for a reaction time of 2 h

Similar as above, TEM imaging was used to investigate the morphology of core/shell $LiYbF_4:Nd^{3+}@LiYF_4$ (2%) RENPs as well as their size distribution. We observed a narrow size distribution with a particle size of approximately 27 nm (with a shell approximately 1-3 nm) with a hexagonal structure.

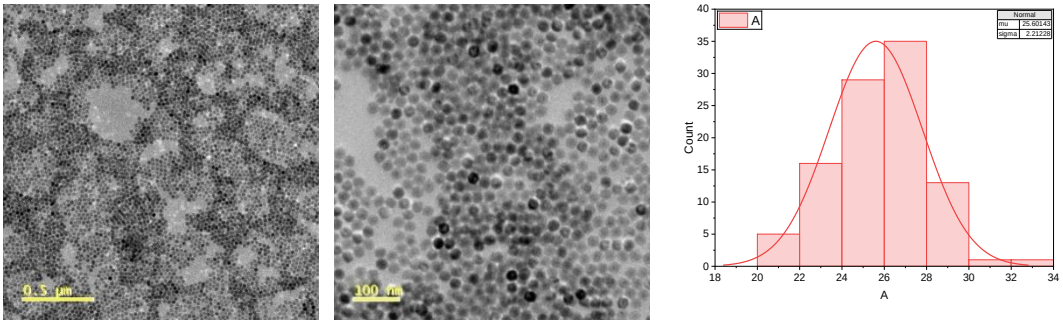

Figure 4.8 TEM image and size distribution graph of $LiYbF_4:Nd^{3+}@LiYF_4$ (2%) for a reaction time of 1 h

Furthermore, the 3D morphological structure and composition of the surface of $LiYbF_4:Nd^{3+}@LiYF_4$ (2%) RENPs at different magnifications (Figure 4.9) was investigated with a scanning electron microscope (SEM).

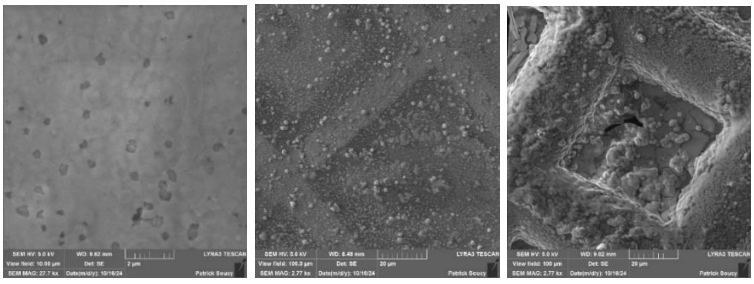

Figure 4.9 SEM image of $LiYbF_4:Nd^{3+}@LiYF_4$ (2%) for a reaction time of 1 h

The overall RENPs diameter (d_{total}), core diameter (d_{core}), $LiYF_4$ shell thickness (d_{shell}) and Photoluminescence peak are shown in **Table 2** below:

Table 2 Dimensions and optical properties of core and core@shell RENPs investigated in this study. The overall size of $LiYbF_4:Nd^{3+}@LiYF_4$ determined from TEM observations, an estimate of the core size is obtained from the position of the peak seen in the distribution graph while the shell thickness is estimated by dividing the diameter by 2 of the core@shell and core.

Number	Sample	Diameter (nm)	Core/ Shell Diameter (nm)	Shell Thickness (nm)	PL max (nm)
1	$LiYbF_4:Nd^{3+}$ (2%)	23.3 ± 4.6	24	0	
2	$LiYbF_4:Nd^{3+}$ (60%)	27.9 ± 2.7	28	0	
3	$LiYbF_4:Nd^{3+}$ (60%, 3 h)	6.1 ± 1.0	6	0	
4	$LiYbF_4:Nd^{3+}$ (60%, 2 h 15 min)	8.8 ± 1.7	9	0	
5	$LiYbF_4:Nd^{3+}$ (60%, 2 h 30 min)	5.5 ± 1.6	5	0	
6	$LiYbF_4:Nd^{3+}@LiYF_4$ (2%)	25.6 ± 2.2	27	3	
7	$LiYbF_4:Nd^{3+}@LiYF_4$ (60%)	34.1 ± 4.6	34	6	1050

Subsequently, the morphological characteristics of the RENPs was analyzed using an X-ray diffractometer and EDX. The XRD diffractogram was analyzed, and it matched well with the reference diffraction pattern of tetragonal $LiYF_4$ crystal (Figure 4.10).

The presence of Nd^{3+} ions in the $LiYbF_4:Nd^{3+}@LiYF_4$ (2% and 60%) RENPs was confirmed by EDX. From Figure 4.11, we observe the presence of Nd^{3+} in the 60% sample. It should be noted that for the 2% sample, the intensity of the peaks was much lower, as expected due to the significantly lower doping concentrations. Moreover, the presence of other elements in the $LiYbF_4:Nd^{3+}@LiYF_4$ matrix, namely Y^{3+}, Yb^{3+}, and Li, was confirmed by the EDX mapping.

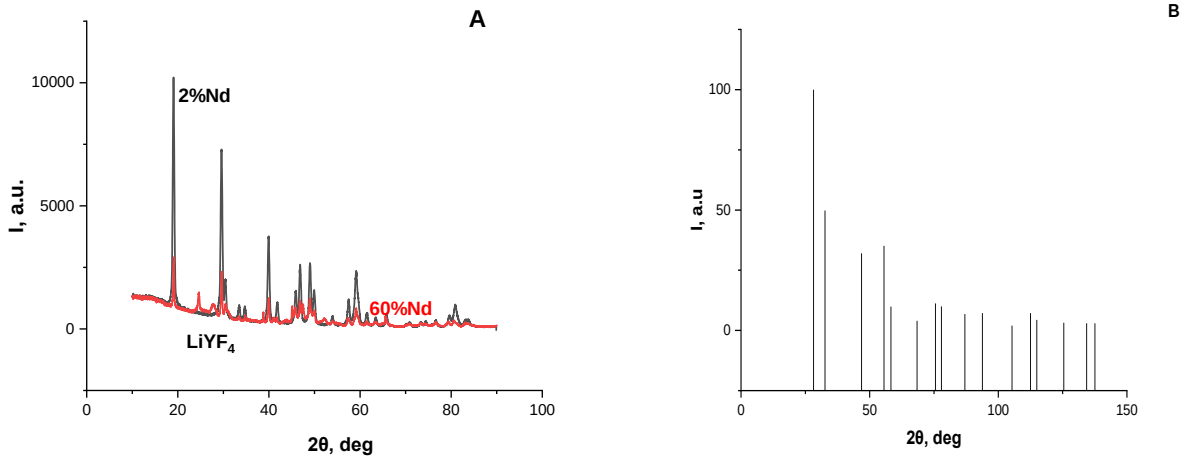

Figure 4.10 (A) XRD pattern of $LiYbF_4:Nd^{3+}@LiYF_4$ (2% and 60%) and (B) Reference pattern of $LiYF_4$ (01-090-0951 ICSD)

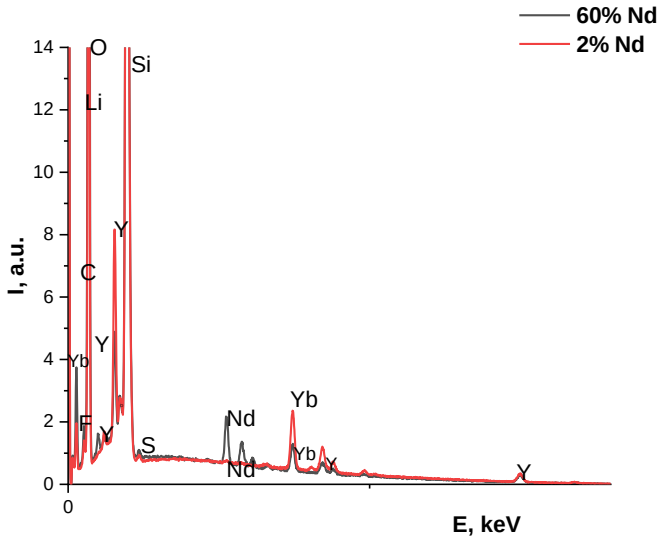

Figure 4.11 EDX spectrum of $LiYbF_4:Nd^{3+}@LiYF_4$ RENPs (60% and 2%)

4.3 Optical characterization of the core/shell $LiYbF_4:Nd^{3+}@LiYF_4$ (60% and 2% Nd)

We characterized the photoluminescence properties of the synthesized core/shell $LiYbF_4:Nd^{3+}@LiYF_4$ (60% and 2%) samples to assess the effect of heavily doped Nd^{3+} ion. The photoluminescence of RENPS in the spectral range of 400-1100 nm was measured under 808 nm excitation. Initially, we investigated the upconversion photoluminescence of $LiYbF_4:Nd^{3+}@LiYF_4$ (60%) sample (dispersed in hexane) following 808 nm excitation. We observed several upconverted emission peaks ascribed to the following transitions in the 400-700 nm spectral range. Specifically, 450 nm ($^2H_{9/2}\rightarrow{}^4I_{15/2}$), 530-550 nm ($^2H_{11/2,}\ ^4S_{3/2}\rightarrow{}^4I_{15/2}$), 600-610 nm ($^4I_{11/2}\rightarrow{}^4G_{7/2}$), 660-670 nm ($^4F_{9/2}\rightarrow{}^4I_{15/2}$).

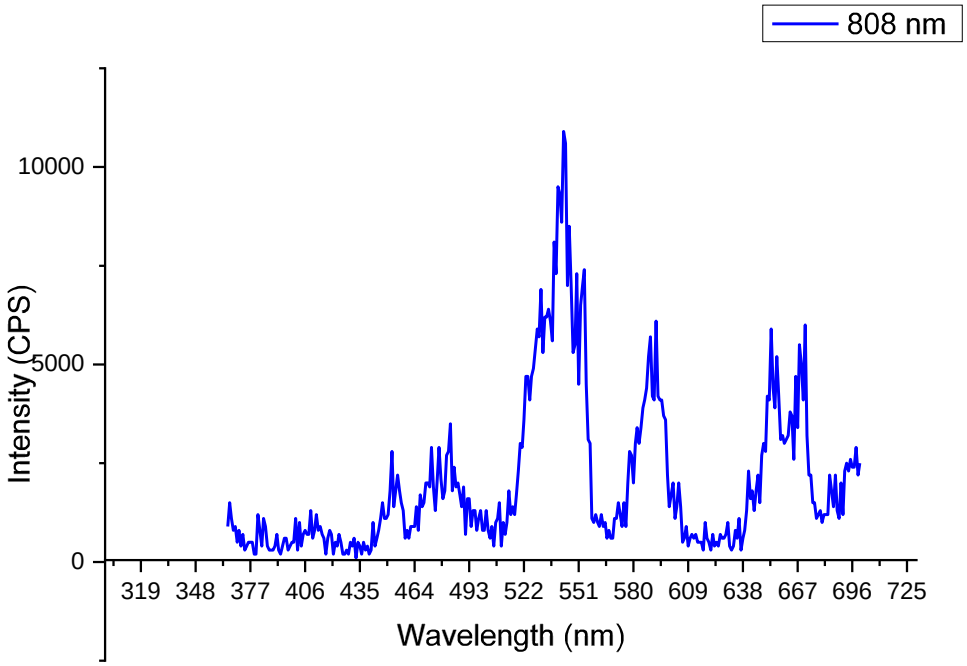

Figure 4.12 Upconversion photoluminescence spectrum of $LiYbF_4:Nd^{3+}@LiYF_4$ (60%)

No downshifting photoluminescence was observed from the core only samples when doped with 2% and 60% Nd^{3+} RENPs following 808 nm as seen in Figure 4.13A (left image). However, after shelling, downshifting photoluminescence was in fact observed as can be seen in Figure 4.13B

(right image) when irradiated with 808 nm. The downshifting emission bands are observed at approximately 920 nm, 1050 nm and 1100 nm, corresponding with transition from $^4F_{3/2}$ excited states to the stark sublevels of the $^4I_{9/2,}$ and $^4I_{11/2,}$ manifolds.

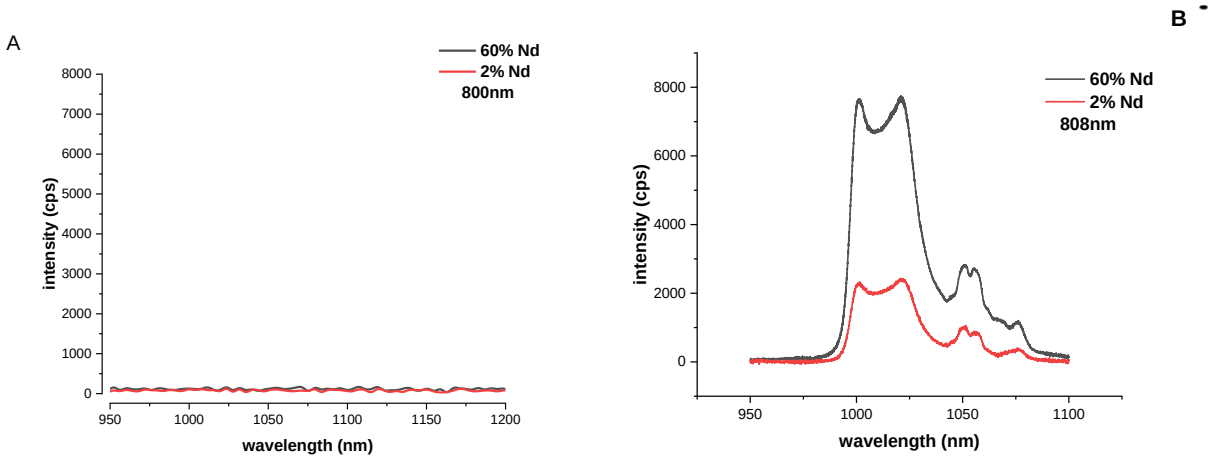

Figure 4.13 (A) Downshifting photoluminescence spectrum of $LiYbF_4:Nd^{3+}$ core (60%) 808 nm and (B) of the $LiYbF_4:Nd^{3+}@LiYF_4$ core/shell following 808 nm excitation (power density =~140W/cm^2)

The synthesized RENPs can only be dispersed in non-polar solvents, hence the dispersion in hexane. We attempted to strip the oleate ligands from the RENP surface as discussed above to obtain water dispersibility for potential application in biomedicine. We used nitrosonium tetrafluoroborate ($NOBF_4$) as the oxidizing and ligand stripping agent for the RENPs to render the RENPs dispersible in water. Unfortunately, no downshifting emission was observed under 808 nm excitation for both the core and core/shell samples. Further studies will focus on other surface modification methods like encapsulation in phospholipid micelles using non-PEGylated unsaturated phospholipids.

4.4 Nanothermometry

Apart from NIR imaging, downshifting emissions can spectrally provide information about temperatures of the RENP environment, as discussed in the literature review. This will enable real-time temperature monitoring while trying to avoid overheating and damage to tissues. A temperature-controlled cuvette holder was used to monitor the temperature change. At different temperatures, it was observed that the intensity of Nd^{3+} remained nearly constant with a few

changes in intensity (Figure 4.14A and Figure 4.14B). We also calculated the luminescent intensity ratio (LIR) Δ between the 2 Stark components. Δ (= I_1(1000.7-1015.5 nm)/ I_2 (1019.9 nm-1022.6 nm) integration ranges were used in plotting the thermometric parameter Δ as a function of temperature. Nd^{3+} emission band showed high thermal sensitivity around 1050 nm, making it suitable for remote photoluminescence thermometry. The LIR Δ showed a linear progression when plotted against temperature change in the range of 25-45 ^{O}C at a temperature increase of 5 ^{o}C. (Figure 4.14B)

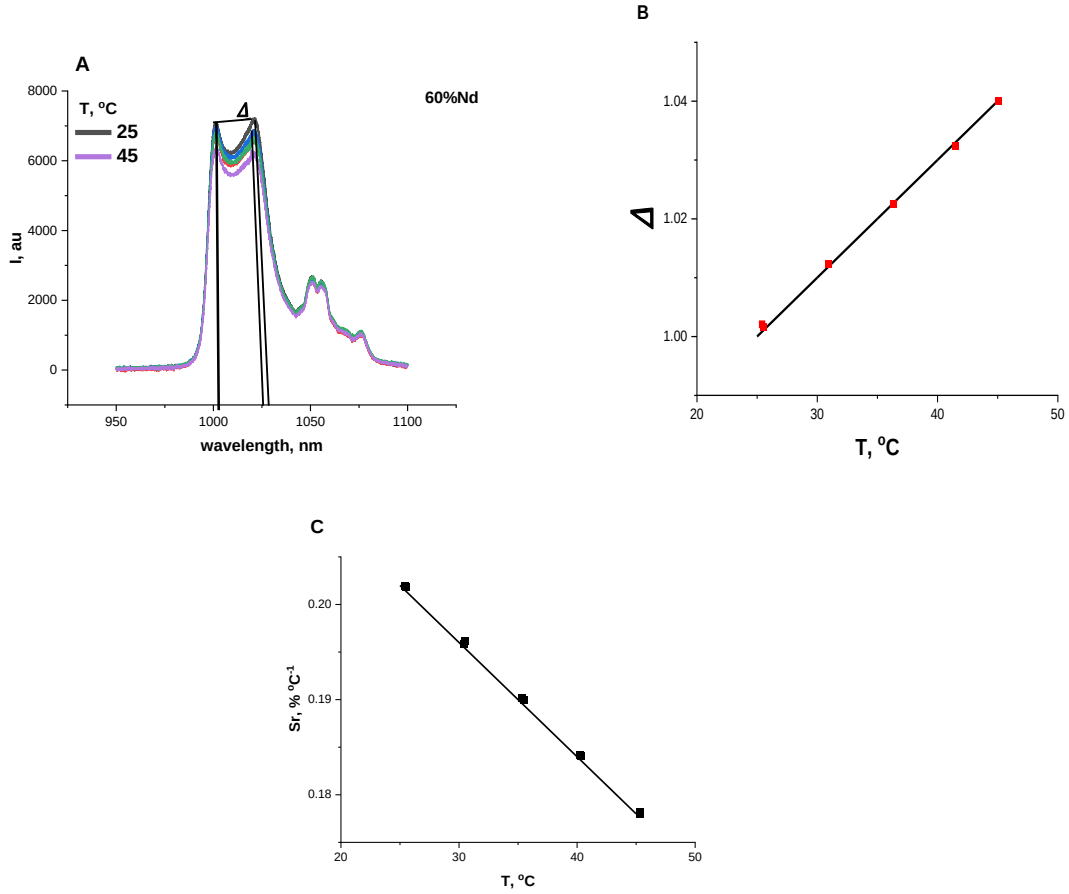

Figure 4.14 Downshifting NIR nanothermometry

A- Downshifting emission spectra of Nd^{3+} RENPs under 808 nm excitation at different temperatures. The values under the curve are used to calculate the LIR Δ thermometric parameter. B- Graph of LIR Δ thermometric parameter against temperature. C- Relative temperature sensitivity (S_r) as a function of temperature.

It can be observed that the relative thermal sensitivity decreases slightly as the temperature increases.

The core/shell sample $LiYbF_4:Nd^{3+}@LiYF_4$ (60%) was excited at an excitation wavelength of 808 nm for 50 min, and the temperature was monitored using a thermal camera. This was done to determine if the heavily doped Nd^{3+} sample would generate heat following 808 nm excitation. It was observed that no temperature change of the sample was recorded even after 50 min excitation.

Also, we investigated the change in the downshifting photoluminescence spectra under continuous laser irradiation for 20 min, however, no change was noticed.

5 CONCLUSION and FUTURE PERSPECTIVES

5.1 Conclusion

In summary, we carried out the controlled synthesis of heavily doped $LiYbF_4:Nd^{3+}$ (60 mol%) RENPs by optimizing different parameters, which could affect the lattice strain. We went further to improve the optical properties and reduce surface quenching by creating a core/inert shell structure $LiYbF_4:Nd^{3+}@LiYF_4$. We determined that by increasing the reaction time to above 2 h, and reducing the reaction temperature from 330 ^oC to 315 ^oC, and controlling concentration, we were able to obtain a uniformly shaped and well dispersed RENPs. These uniformly shaped particles are important when applied in PTT or PDT for cancer treatment as different sized nanoparticles can behave differently in the body. Hence, monodispersibility is very important when considering future biomedical applications.

Also, we investigated the photoluminescence properties of $LiYbF_4:Nd^{3+}@LiYF_4$ RENPs. The downshifting photoluminesence spectrum of Nd^{3+} doped RENPs under 808 nm excitation showed distinct emission peaks at approximately 920 nm, 1050 nm, and 1100 nm. The most dominant emission peak is seen at approximately 1050 nm. The strong NIR emission peak, makes the RENPs suitable for bioimaging and optical sensors. The upconversion photoluminescence spectrum shows a strong green emission at approximately 530 nm and 550 nm, red emissions in the range of approximately 660- 670 nm, and minor peaks in the blue region at approximately 450 nm. The dominant green and red emission indicates efficient upconversion. These emissions are ideal for biomedical applications due to their penetration depth in biological tissues. The luminescence intensity ratio (LIR) obtained from nanothermometry measurements showed a linear progression with increasing temperature, demonstrating these RENPs as temperature sensors. However, the relative sensitivity (S_r) decreases as temperature increases, this can be associated with thermal quenching effects commonly observed in RENPs. $LiYbF_4:Nd^{3+}@LiYF_4$ RENPs showed significant potential for future temperature-sensitive biomedical applications.

5.2 Future Perspective

Heavily doped Nd^{3+}-sensitized rare-earth nanoparticles (RENPs), which can be stimulated using an 800 nm laser, have demonstrated promising applications in areas like photodynamic therapy, deep tissue imaging, and biosensing[283]. Particle size, shape, and surface characteristics of the RENPs can influence their optical, photothermal, and biocompatibility. Different areas still need attention in future research to fully realize the clinical potential of Nd^3-doped RENPs.

An advanced synthesis method to achieve both uniform and controllable morphology in heavily doped RENPs should be explored. Strategies such as core modification with single or multiple shells, dye incorporation into RENPs for broader light absorption, co-doping with metal ions, and leveraging surface plasmon resonance [284, 285] have shown promise in enhancing morphological control. Optimizing these parameters can enhance photonic efficiency and minimize energy loss for better photodynamic therapy and imaging.

Further studies could also aim at exploring functionalization techniques to improve dispersion in the biological environment and reduce cytotoxicity. Tailoring surface texture and coatings of RENPs can improve their interaction with cancer cells.

Developing scalable and cost-effective synthesis methods for RENPs, while maintaining the consistency of their morphology and properties, will be crucial for their widespread use in cancer therapy. The evaluation of long-term biocompatibility to ensure safety and efficacy in vivo should be investigated. Additionally, future work should emphasize regulatory approval processes, clinical trials, and the development of standardized protocols for RENP-based cancer treatments.

By addressing these challenges, morphological control of heavily doped Nd^{3+} RENPs can unlock new possibilities in the world of nanomedicine.

6 BIBLIOGRAPHY

1. Chen, G., et al., *Upconversion nanoparticles: design, nanochemistry, and applications in theranostics.* Chemical reviews, 2014. **114**(10): p. 5161-5214.
2. Haase, M. and H. Schäfer, *Upconverting nanoparticles.* Angewandte Chemie International Edition, 2011. **50**(26): p. 5808-5829.
3. Doane, T.L. and C. Burda, *The unique role of nanoparticles in nanomedicine: imaging, drug delivery and therapy.* Chemical Society Reviews, 2012. **41**(7): p. 2885-2911.
4. Pu, X., et al., *Mesoporous silica nanoparticles as a prospective and promising approach for drug delivery and biomedical applications.* Current cancer drug targets, 2019. **19**(4): p. 285-295.
5. Zhou, J., Z. Liu, and F. Li, *Upconversion nanophosphors for small-animal imaging.* Chemical Society Reviews, 2012. **41**(3): p. 1323-1349.
6. Wang, F. and X. Liu, *Upconversion multicolor fine-tuning: visible to near-infrared emission from lanthanide-doped NaYF4 nanoparticles.* Journal of the American Chemical Society, 2008. **130**(17): p. 5642-5643.
7. Cheng, L., C. Wang, and Z. Liu, *Upconversion nanoparticles and their composite nanostructures for biomedical imaging and cancer therapy.* Nanoscale, 2013. **5**(1): p. 23-37.
8. Chen, J. and J.X. Zhao, *Upconversion nanomaterials: synthesis, mechanism, and applications in sensing.* Sensors, 2012. **12**(3): p. 2414-2435.
9. Auzel, F., *Upconversion and anti-stokes processes with f and d ions in solids.* Chemical reviews, 2004. **104**(1): p. 139-174.
10. Egger, P., et al., *Ba2ErCl7—a new near IR to near UV upconversion material.* Advanced Materials, 1996. **8**(8): p. 668-672.
11. Yang, J., et al., *Mesoporous silica encapsulating upconversion luminescence rare-earth fluoride nanorods for secondary excitation.* Langmuir, 2010. **26**(11): p. 8850-8856.
12. Zhou, J., et al., *Dual-modality in vivo imaging using rare-earth nanocrystals with near-infrared to near-infrared (NIR-to-NIR) upconversion luminescence and magnetic resonance properties.* Biomaterials, 2010. **31**(12): p. 3287-3295.
13. Cao, T., et al., *High-quality water-soluble and surface-functionalized upconversion nanocrystals as luminescent probes for bioimaging.* Biomaterials, 2011. **32**(11): p. 2959-2968.
14. Hu, H., et al., *Facile epoxidation strategy for producing amphiphilic up-converting rare-earth nanophosphors as biological labels.* Chemistry of Materials, 2008. **20**(22): p. 7003-7009.
15. Naccache, R., et al., *Controlled synthesis and water dispersibility of hexagonal phase NaGdF4: Ho3+/Yb3+ nanoparticles.* Chemistry of Materials, 2009. **21**(4): p. 717-723.
16. Yi, G.-S. and G.-M. Chow, *Water-soluble NaYF4: Yb, Er (Tm)/NaYF4/polymer core/shell/shell nanoparticles with significant enhancement of upconversion fluorescence.* Chemistry of Materials, 2007. **19**(3): p. 341-343.

17. Hu, H., et al., *Multimodal-luminescence core–shell nanocomposites for targeted imaging of tumor cells.* Chemistry–A European Journal, 2009. **15**(14): p. 3577-3584.

18. Jiang, S., et al., *NIR-to-visible upconversion nanoparticles for fluorescent labeling and targeted delivery of siRNA.* Nanotechnology, 2009. **20**(15): p. 155101.

19. Jiang, S. and Y. Zhang, *Upconversion nanoparticle-based FRET system for study of siRNA in live cells.* Langmuir, 2010. **26**(9): p. 6689-6694.

20. Zhang, F., et al., *Fabrication of Ag@ SiO2@ Y2O3: Er nanostructures for bioimaging: tuning of the upconversion fluorescence with silver nanoparticles.* Journal of the American Chemical Society, 2010. **132**(9): p. 2850-2851.

21. Li, Z. and Y. Zhang, *Monodisperse silica-coated polyvinyl-pyrrolidone/NaYF4 nanocrystals with multicolor upconversion fluorescence emission.* Angewandte Chemie-International Edition, 2006. **45**(46): p. 7732-7735.

22. Liu, Q., et al., *"Drawing" upconversion nanophosphors into water through host–guest interaction.* Chemical communications, 2010. **46**(30): p. 5551-5553.

23. Liu, Q., et al., *Multifunctional rare-earth self-assembled nanosystem for tri-modal upconversion luminescence/fluorescence/positron emission tomography imaging.* Biomaterials, 2011. **32**(32): p. 8243-8253.

24. Liu, Q., et al., *18F-labeled magnetic-upconversion nanophosphors via rare-earth cation-assisted ligand assembly.* Acs Nano, 2011. **5**(4): p. 3146-3157.

25. Wang, X., et al., *A general strategy for nanocrystal synthesis.* Nature, 2005. **437**(7055): p. 121-124.

26. Jalil, R.A. and Y. Zhang, *Biocompatibility of silica coated NaYF4 upconversion fluorescent nanocrystals.* Biomaterials, 2008. **29**(30): p. 4122-4128.

27. Guo, H., et al., *Singlet oxygen-induced apoptosis of cancer cells using upconversion fluorescent nanoparticles as a carrier of photosensitizer.* Nanomedicine: Nanotechnology, Biology and Medicine, 2010. **6**(3): p. 486-495.

28. Li, Z., et al., *Modification of NaYF4: Yb, Er@ SiO2 nanoparticles with gold nanocrystals for tunable green-to-red upconversion emissions.* The Journal of Physical Chemistry C, 2011. **115**(8): p. 3291-3296.

29. Liu, Q., et al., *Sub-10 nm hexagonal lanthanide-doped NaLuF4 upconversion nanocrystals for sensitive bioimaging in vivo.* Journal of the American Chemical Society, 2011. **133**(43): p. 17122-17125.

30. Lim, S.F., et al., *In vivo and scanning electron microscopy imaging of upconverting nanophosphors in Caenorhabditis elegans.* Nano Letters, 2006. **6**(2): p. 169-174.

31. Xiong, L., et al., *High contrast upconversion luminescence targeted imaging in vivo using peptide-labeled nanophosphors.* Analytical chemistry, 2009. **81**(21): p. 8687-8694.

32. Liu, X., C.-H. Yan, and J.A. Capobianco, *Photon upconversion nanomaterials.* Chemical Society Reviews, 2015. **44**(6): p. 1299-1301.

33. Ye, C., et al., *Photon upconversion: from two-photon absorption (TPA) to triplet–triplet annihilation (TTA).* Physical Chemistry Chemical Physics, 2016. **18**(16): p. 10818-10835.

34. Sun, Q.-C., et al., *Photon upconversion towards applications in energy conversion and bioimaging.* Progress in Surface Science, 2017. **92**(4): p. 281-316.

35. Yadav, R., S. Dhoble, and S. Rai, *Improved photon upconversion photoluminescence and intrinsic optical bistability from a rare earth co-doped lanthanum oxide phosphor via Bi 3+ doping.* New Journal of Chemistry, 2018. **42**(9): p. 7272-7282.

36. Du, P. and J.S. Yu, *Upconversion emission and cathodoluminescence of Yb3+ ions activated BiOCl: Ho3+ phosphors.* Materials Letters, 2016. **169**: p. 135-139.

37. Savel'ev, E., et al., *Luminescence of Yb3+ ions in silica-based glasses synthesized by SPCVD.* Optical Materials, 2017. **64**: p. 427-435.

38. Rivera-Lopez, F. and V. Lavin, *Upconversion/back-transfer losses and emission dynamics in Nd3+-Yb3+ co-doped phosphate glasses for multiple pump channel laser.* Journal of Non-Crystalline Solids, 2018. **489**: p. 84-90.

39. Chan, M.H., et al., *Minimizing the heat effect of photodynamic therapy based on inorganic nanocomposites mediated by 808 nm near-infrared light.* Small, 2017. **13**(21): p. 1700038.

40. Li, X., F. Zhang, and D. Zhao, *Lab on upconversion nanoparticles: optical properties and applications engineering via designed nanostructure.* Chemical Society Reviews, 2015. **44**(6): p. 1346-1378.

41. Jethva, P., et al., *Lanthanide-Doped Upconversion Luminescent Nanoparticles—Evolving Role in Bioimaging, Biosensing, and Drug Delivery.* Materials, 2022. **15**(7): p. 2374.

42. Gao, D., et al., *Multifunctional phototheranostic nanomedicine for cancer imaging and treatment.* Materials Today Bio, 2020. **5**: p. 100035.

43. Liu, B., et al., *Multifunctional UCNPs@ PDA-ICG nanocomposites for upconversion imaging and combined photothermal/photodynamic therapy with enhanced antitumor efficacy.* Journal of materials chemistry B, 2016. **4**(28): p. 4884-4894.

44. Zhou, B., et al., *Controlling upconversion nanocrystals for emerging applications.* Nature nanotechnology, 2015. **10**(11): p. 924-936.

45. Wang, F. and X. Liu, *Recent advances in the chemistry of lanthanide-doped upconversion nanocrystals.* Chemical Society Reviews, 2009. **38**(4): p. 976-989.

46. Cheng, X., et al., *Design for brighter photon upconversion emissions via energy level overlap of lanthanide ions.* ACS nano, 2018. **12**(11): p. 10992-10999.

47. Wang, Z. and A. Meijerink, *Concentration quenching in upconversion nanocrystals.* The Journal of Physical Chemistry C, 2018. **122**(45): p. 26298-26306.

48. Eliseeva, S.V. and J.-C.G. Bünzli, *Lanthanide luminescence for functional materials and bio-sciences.* Chemical Society Reviews, 2010. **39**(1): p. 189-227.

49. Vu, D.T., et al., *A synergy approach to enhance upconversion luminescence emission of rare earth nanophosphors with million-fold enhancement factor.* Crystals, 2021. **11**(10): p. 1187.

50. Suk, J.S., et al., *PEGylation as a strategy for improving nanoparticle-based drug and gene delivery.* Advanced drug delivery reviews, 2016. **99**: p. 28-51.

51. Ding, H., et al., *Fe3O4@ SiO2 core/shell nanoparticles: the silica coating regulations with a single core for different core sizes and shell thicknesses.* Chemistry of Materials, 2012. **24**(23): p. 4572-4580.

52. Hatakeyama, M., et al., *A two-step ligand exchange reaction generates highly water-dispersed magnetic nanoparticles for biomedical applications.* Journal of Materials Chemistry, 2011. **21**(16): p. 5959-5966.

53. Jain, A., et al., *Functionalized rare earth-doped nanoparticles for breast cancer nanodiagnostic using fluorescence and CT imaging.* Journal of Nanobiotechnology, 2018. **16**: p. 1-18.

54. Hong, E., et al., *Control synthesis, subtle surface modification of rare-earth-doped upconversion nanoparticles and their applications in cancer diagnosis and treatment.* Materials Science and Engineering: C, 2019. **105**: p. 110097.

55. Karthi, S., et al., *Synthesis and characterization of Nd3+: Yb3+ co-doped near infrared sensitive fluorapatite nanoparticles as a bioimaging probe.* Optical Materials, 2018. **77**: p. 39-47.

56. Chen, D., et al., *Nd3+-sensitized Ho3+ single-band red upconversion luminescence in core–shell nanoarchitecture.* The journal of physical chemistry letters, 2015. **6**(14): p. 2833-2840.

57. Huang, X., *Giant enhancement of upconversion emission in (NaYF 4: Nd 3+/Yb 3+/Ho 3+)/(NaYF 4: Nd 3+/Yb 3+) core/shell nanoparticles excited at 808 nm.* Optics letters, 2015. **40**(15): p. 3599-3602.

58. Qin, Y., et al., *Modification on populating paths of β-NaYF 4: Nd/Yb/Ho@ SiO 2@ Ag core/double-shell nanocomposites with plasmon enhanced upconversion emission.* Optical Materials Express, 2016. **6**(6): p. 1942-1955.

59. Wang, Y.-F., et al., *Nd3+-sensitized upconversion nanophosphors: efficient in vivo bioimaging probes with minimized heating effect.* ACS nano, 2013. **7**(8): p. 7200-7206.

60. Wang, Y., et al., *Upconversion emission enhancement mechanisms of Nd 3+-sensitized NaYF 4: Yb 3+, Er 3+ nanoparticles using tunable plasmonic Au films: plasmonic-induced excitation, radiative decay rate and energy-transfer enhancement.* Journal of Materials Chemistry C, 2017. **5**(33): p. 8535-8544.

61. Cao, C., et al., *Energy transfer highway in Nd3+-sensitized nanoparticles for efficient near-infrared bioimaging.* ACS Applied Materials & Interfaces, 2017. **9**(22): p. 18540-18548.

62. Xiaobin, D., et al., *Ultraviolet to near-infrared energy transfer in NaYF4: Nd3+, Yb3+ crystals.* Journal of Rare Earths, 2016. **34**(9): p. 863-867.

63. Zhang, F., et al., *Uniform nanostructured arrays of sodium rare-earth fluorides for highly efficient multicolor upconversion luminescence.* Angewandte Chemie, 2007. **119**(42): p. 8122-8125.

64. Zeng, S., et al., *High uniformity and monodispersity of sodium rare-earth fluoride nanocrystals: controllable synthesis, shape evolution and optical properties.* CrystEngComm, 2011. **13**(5): p. 1384-1390.

65. Na, H., et al., *Rational morphology control of β-NaYF 4: Yb, Er/Tm upconversion nanophosphors using a ligand, an additive, and lanthanide doping.* Nanoscale, 2013. **5**(10): p. 4242-4251.

66. Ye, X., et al., *Morphologically controlled synthesis of colloidal upconversion nanophosphors and their shape-directed self-assembly.* Proceedings of the National Academy of Sciences, 2010. **107**(52): p. 22430-22435.

67. Li, C., et al., *Shape-controllable synthesis and upconversion properties of lutetium fluoride (doped with Yb3+/Er3+) microcrystals by hydrothermal process.* The Journal of Physical Chemistry C, 2008. **112**(35): p. 13395-13404.

68. Wu, Y., et al., *Rare earth β-NaGdF4 fluorides with multiform morphologies: hydrothermal synthesis and luminescent properties.* Journal of colloid and interface science, 2011. **354**(2): p. 429-436.

69. Cong, T., et al., *Synthesis and optical properties of Zn2+ doped NaYF4: Yb3+, Er3+ upconversion nanoparticles.* Materials Letters, 2016. **165**: p. 59-62.

70. Zhang, Y., et al., *Ultrasmall-superbright neodymium-upconversion nanoparticles via energy migration manipulation and lattice modification: 808 nm-activated drug release.* ACS nano, 2017. **11**(3): p. 2846-2857.

71. Arboleda, C., et al., *High Nd (III)-Sensitizer Concentrations for 800 nm Wavelength Excitation Using Isotropic Core–Shell Upconversion Nanoparticles.* Chemistry of Materials, 2019. **31**(9): p. 3103-3110.

72. Li, J., et al., *Up-conversion emission color tuning in NaLa (MoO4) 2: Nd3+/Yb3+/Ho3+ excited at 808 nm.* Ceramics International, 2017. **43**(8): p. 6333-6339.

73. Mingbin, D., et al., *Trivalent Yb/Ho/Ce tri-doped core/shell NaYF4 nanoparticles for tunable upconversion luminescence from green to red.* Journal of Rare Earths, 2017. **35**(7): p. 629-636.

74. Champion, J.A., Y.K. Katare, and S. Mitragotri, *Particle shape: a new design parameter for micro-and nanoscale drug delivery carriers.* Journal of controlled release, 2007. **121**(1-2): p. 3-9.

75. Liu, Y., et al., *The shape of things to come: importance of design in nanotechnology for drug delivery.* Therapeutic delivery, 2012. **3**(2): p. 181-194.

76. Mathaes, R., et al., *Non-spherical micro-and nanoparticles: fabrication, characterization and drug delivery applications.* Expert opinion on drug delivery, 2015. **12**(3): p. 481-492.

77. Eliezar, J., et al., *In vivo evaluation of folate decorated cross-linked micelles for the delivery of platinum anticancer drugs.* Biomacromolecules, 2015. **16**(2): p. 515-523.

78. MacDonald, I., E. Schmidt, and A. Groom, *The high splenic hematocrit: a rheological consequence of red cell flow through the reticular meshwork.* Microvascular research, 1991. **42**(1): p. 60-76.

79. Canelas, D.A., K.P. Herlihy, and J.M. DeSimone, *Top-down particle fabrication: control of size and shape for diagnostic imaging and drug delivery.* Wiley Interdisciplinary Reviews: Nanomedicine and Nanobiotechnology, 2009. **1**(4): p. 391-404.

80. Decuzzi, P., et al., *Intravascular delivery of particulate systems: does geometry really matter?* Pharmaceutical research, 2009. **26**: p. 235-243.

81. Yoo, J.-W., N. Doshi, and S. Mitragotri, *Adaptive micro and nanoparticles: temporal control over carrier properties to facilitate drug delivery.* Advanced drug delivery reviews, 2011. **63**(14-15): p. 1247-1256.

82. De Jong, W.H., et al., *Particle size-dependent organ distribution of gold nanoparticles after intravenous administration.* Biomaterials, 2008. **29**(12): p. 1912-1919.

83. Nakamura, H. and S. Watano, *Direct permeation of nanoparticles across cell membrane: a review.* KONA Powder and Particle Journal, 2018. **35**: p. 49-65.

84. Bruce, J.N., *Improving drug delivery to Intracerebral tumor and surrounding brain in a rodent model: a comparison of osmotic versus Bradykinin modification of the blood-brain and/or blood-tumor barriers.* Neurosurgery, 1998. **43**(4): p. 889.

85. Steichen, S.D., M. Caldorera-Moore, and N.A. Peppas, *A review of current nanoparticle and targeting moieties for the delivery of cancer therapeutics.* European journal of pharmaceutical sciences, 2013. **48**(3): p. 416-427.

86. Redhead, H., S. Davis, and L. Illum, *Drug delivery in poly (lactide-co-glycolide) nanoparticles surface modified with poloxamer 407 and poloxamine 908: in vitro characterisation and in vivo evaluation.* Journal of Controlled Release, 2001. **70**(3): p. 353-363.

87. Niikura, K., et al., *Sub-100 nm gold nanoparticle vesicles as a drug delivery carrier enabling rapid drug release upon light irradiation.* ACS applied materials & interfaces, 2013. **5**(9): p. 3900-3907.

88. Yu, X., et al., *High-resolution MRI characterization of human thrombus using a novel fibrin-targeted paramagnetic nanoparticle contrast agent.* Magnetic Resonance in Medicine: An Official Journal of the International Society for Magnetic Resonance in Medicine, 2000. **44**(6): p. 867-872.

89. Chithrani, B.D., A.A. Ghazani, and W.C. Chan, *Determining the size and shape dependence of gold nanoparticle uptake into mammalian cells.* Nano letters, 2006. **6**(4): p. 662-668.

90. Cho, E.C., et al., *Understanding the role of surface charges in cellular adsorption versus internalization by selectively removing gold nanoparticles on the cell surface with a I2/KI etchant.* Nano letters, 2009. **9**(3): p. 1080-1084.

91. Albanese, A. and W.C. Chan, *Effect of gold nanoparticle aggregation on cell uptake and toxicity.* ACS nano, 2011. **5**(7): p. 5478-5489.

92. Oh, N. and J.-H. Park, *Endocytosis and exocytosis of nanoparticles in mammalian cells.* International journal of nanomedicine, 2014. **9**(sup1): p. 51-63.

93. Chithrani, B.D. and W.C. Chan, *Elucidating the mechanism of cellular uptake and removal of protein-coated gold nanoparticles of different sizes and shapes.* Nano letters, 2007. **7**(6): p. 1542-1550.

94. Jiang, W., et al., *Nanoparticle-mediated cellular response is size-dependent.* Nature nanotechnology, 2008. **3**(3): p. 145-150.

95. Win, K.Y. and S.-S. Feng, *Effects of particle size and surface coating on cellular uptake of polymeric nanoparticles for oral delivery of anticancer drugs.* Biomaterials, 2005. **26**(15): p. 2713-2722.

96. Ximendes, E.C., et al., *Unveiling in vivo subcutaneous thermal dynamics by infrared luminescent nanothermometers.* Nano letters, 2016. **16**(3): p. 1695-1703.

97. Celli, J.P., et al., *Imaging and photodynamic therapy: mechanisms, monitoring, and optimization.* Chemical reviews, 2010. **110**(5): p. 2795-2838.

98. Andrews, D., G. Scholes, and G. Wiederrecht, *Comprehensive nanoscience and technology*. 2010: Academic Press.

99. Jiang, Y. and K. Pu, *Advanced photoacoustic imaging applications of near-infrared absorbing organic nanoparticles.* Small, 2017. **13**(30): p. 1700710.

100. Lemaster, J.E. and J.V. Jokerst, *What is new in nanoparticle-based photoacoustic imaging?* Wiley Interdisciplinary Reviews: Nanomedicine and Nanobiotechnology, 2017. **9**(1): p. e1404.

101. Mantri, Y. and J.V. Jokerst, *Engineering plasmonic nanoparticles for enhanced photoacoustic imaging.* ACS nano, 2020. **14**(8): p. 9408-9422.

102. Ai, K., et al., *Localized surface plasmon resonance properties and biomedical applications of copper selenide nanomaterials.* Materials Today Chemistry, 2021. **20**: p. 100402.

103. Mai, H.-X., et al., *Size-and phase-controlled synthesis of monodisperse NaYF4: Yb, Er nanocrystals from a unique delayed nucleation pathway monitored with upconversion spectroscopy.* The Journal of Physical Chemistry C, 2007. **111**(37): p. 13730-13739.

104. May, P.B., et al., *The dynamics of nanoparticle growth and phase change during synthesis of β-NaYF4.* The Journal of Physical Chemistry C, 2016. **120**(17): p. 9482-9489.

105. Radunz, S., et al., *Evolution of size and optical properties of upconverting nanoparticles during high-temperature synthesis.* The Journal of Physical Chemistry C, 2018. **122**(50): p. 28958-28967.

106. Yi, G., et al., *Synthesis and characterization of high-efficiency nanocrystal up-conversion phosphors: Ytterbium and erbium codoped lanthanum molybdate.* Chemistry of materials, 2002. **14**(7): p. 2910-2914.

107. Zeng, J.H., et al., *Synthesis and upconversion luminescence of hexagonal-Phase NaYF4: Yb, Er3+ phosphors of controlled size and morphology.* Advanced Materials, 2005. **17**(17): p. 2119-2123.

108. Tong, L., et al., *Gold nanorods as contrast agents for biological imaging: optical properties, surface conjugation and photothermal effects.* Photochemistry and photobiology, 2009. **85**(1): p. 21-32.

109. Li, C., et al., *Highly Uniform and Monodisperse β-NaYF4:Ln3+ (Ln = Eu, Tb, Yb/Er, and Yb/Tm) Hexagonal Microprism Crystals: Hydrothermal Synthesis and Luminescent Properties.* Inorganic Chemistry, 2007. **46**(16): p. 6329-6337.

110. Li, C., et al., *Different microstructures of β-NaYF4 fabricated by hydrothermal process: effects of pH values and fluoride sources.* Chemistry of Materials, 2007. **19**(20): p. 4933-4942.

111. Liu, X., et al., *Ionothermal synthesis of hexagonal-phase NaYF4: Yb 3+, Er 3+/Tm 3+ upconversion nanophosphors.* Chemical Communications, 2009(43): p. 6628-6630.

112. Vetrone, F., et al., *Upconverting Nanoparticles: The Active-Core/Active-Shell Approach: A Strategy to Enhance the Upconversion Luminescence in Lanthanide-Doped Nanoparticles (Adv. Funct. Mater. 18/2009).* Advanced Functional Materials, 2009. **19**(18).

113. Boyer, J.-C. and F.C. Van Veggel, *Absolute quantum yield measurements of colloidal NaYF 4: Er3+, Yb3+ upconverting nanoparticles.* Nanoscale, 2010. **2**(8): p. 1417-1419.

114. Bogdan, N., et al., *Synthesis of ligand-free colloidally stable water dispersible brightly luminescent lanthanide-doped upconverting nanoparticles.* Nano letters, 2011. **11**(2): p. 835-840.

115. Wang, F., J. Wang, and X. Liu, *Direct evidence of a surface quenching effect on size-dependent luminescence of upconversion nanoparticles.* Angew. Chem. Int. Ed, 2010. **49**(41): p. 7456-7460.

116. Johnson, N.J., et al., *Self-focusing by Ostwald ripening: a strategy for layer-by-layer epitaxial growth on upconverting nanocrystals.* Journal of the American Chemical Society, 2012. **134**(27): p. 11068-11071.

117. Zhang, F., et al., *Direct imaging the upconversion nanocrystal core/shell structure at the subnanometer level: shell thickness dependence in upconverting optical properties.* Nano letters, 2012. **12**(6): p. 2852-2858.

118. Huang, X. and J. Lin, *Active-core/active-shell nanostructured design: an effective strategy to enhance Nd 3+/Yb 3+ cascade sensitized upconversion luminescence in lanthanide-doped nanoparticles.* Journal of Materials Chemistry C, 2015. **3**(29): p. 7652-7657.

119. Liu, B., et al., *Poly (Acrylic acid) modification of Nd3+-sensitized upconversion nanophosphors for highly efficient UCL imaging and pH-responsive drug delivery.* Advanced Functional Materials, 2015. **25**(29): p. 4717-4729.

120. Tian, L., et al., *The upconversion luminescence of Er3+/Yb3+/Nd3+ triply-doped β-NaYF4 nanocrystals under 808-nm excitation.* Materials, 2014. **7**(11): p. 7289-7303.

121. Xie, X., et al., *Mechanistic investigation of photon upconversion in Nd3+-sensitized core–shell nanoparticles.* Journal of the American Chemical Society, 2013. **135**(34): p. 12608-12611.

122. Zhou, B., et al., *Enabling photon upconversion and precise control of donor–acceptor interaction through interfacial energy transfer.* Advanced science, 2018. **5**(3): p. 1700667.

123. Zhan, Q., et al., *Controlling the excitation of upconverting luminescence for biomedical theranostics: neodymium sensitizing.* Optical Materials Express, 2016. **6**(4): p. 1011-1023.

124. Zijlmans, H., et al., *Detection of cell and tissue surface antigens using up-converting phosphors: a new reporter technology.* Analytical biochemistry, 1999. **267**(1): p. 30-36.

125. Shalav, A., et al., *Application of NaYF4: Er3+ up-converting phosphors for enhanced near-infrared silicon solar cell response.* Applied Physics Letters, 2005. **86**(1).

126. Ivanova, S. and F. Pellé, *Evaluating upconversion materials developed to improve the efficiency of solar cells: reply to comment.* JOSA B, 2010. **27**(7): p. 1356-1358.

127. Kik, P. and A. Polman, *Cooperative upconversion as the gain-limiting factor in Er doped miniature Al2O3 optical waveguide amplifiers.* Journal of Applied Physics, 2003. **93**(9): p. 5008-5012.

128. Polman, C.S.A., *Relationship between gain and Yb 3+ concentration in Er 3+− Yb 3+ doped waveguide amplifiers.* J. Appl. Phys., 2001. **90**: p. 4314-4320.

129. Zhou, Z., et al., *Up-conversion luminescent switch based on photochromic diarylethene and rare-earth nanophosphors.* Chemical communications, 2008(39): p. 4786-4788.

130. Zhang, C., et al., *Luminescence modulation of ordered upconversion nanopatterns by a photochromic diarylethene: rewritable optical storage with nondestructive readout.* Advanced Materials, 2010. **5**(22): p. 633-637.

131. Yi, G., et al., *Synthesis, characterization, and biological application of size-controlled nanocrystalline NaYF4: Yb, Er infrared-to-visible up-conversion phosphors.* Nano letters, 2004. **4**(11): p. 2191-2196.

132. Kuningas, K., et al., *Simultaneous use of time-resolved fluorescence and anti-stokes photoluminescence in a bioaffinity assay.* Analytical chemistry, 2005. **77**(9): p. 2826-2834.

133. Rantanen, T., et al., *Fluorescence-quenching-based enzyme-activity assay by using photon upconversion.* Angewandte Chemie International Edition, 2008. **47**(20): p. 3811-3813.

134. Rantanen, T., et al., *Tandem dye acceptor used to enhance upconversion fluorescence resonance energy transfer in homogeneous assays.* Analytical chemistry, 2007. **79**(16): p. 6312-6318.

135. Taylor, J.R., M.M. Fang, and S. Nie, *Probing specific sequences on single DNA molecules with bioconjugated fluorescent nanoparticles.* Analytical chemistry, 2000. **72**(9): p. 1979-1986.

136. Medintz, I.L., et al., *Quantum dot bioconjugates for imaging, labelling and sensing.* Nature materials, 2005. **4**(6): p. 435-446.

137. Michalet, X., et al., *Quantum dots for live cells, in vivo imaging, and diagnostics.* science, 2005. **307**(5709): p. 538-544.

138. Ow, H., et al., *Bright and stable core− shell fluorescent silica nanoparticles.* Nano letters, 2005. **5**(1): p. 113-117.

139. O'connell, M.J., et al., *Band gap fluorescence from individual single-walled carbon nanotubes.* Science, 2002. **297**(5581): p. 593-596.

140. Xiong, L.-Q., et al., *Synthesis, characterization, and in vivo targeted imaging of amine-functionalized rare-earth up-converting nanophosphors.* Biomaterials, 2009. **30**(29): p. 5592-5600.

141. Zhou, J.-C., et al., *Bioimaging and toxicity assessments of near-infrared upconversion luminescent NaYF4: Yb, Tm nanocrystals.* Biomaterials, 2011. **32**(34): p. 9059-9067.

142. Cheng, L., et al., *Multicolor in vivo imaging of upconversion nanoparticles with emissions tuned by luminescence resonance energy transfer.* The Journal of Physical Chemistry C, 2011. **115**(6): p. 2686-2692.

143. Ryu, J., et al., *Facile synthesis of ultrasmall and hexagonal NaGdF4: Yb3+, Er3+ nanoparticles with magnetic and upconversion imaging properties.* The Journal of Physical Chemistry C, 2010. **114**(49): p. 21077-21082.

144. Yu, M., et al., *Laser scanning up-conversion luminescence microscopy for imaging cells labeled with rare-earth nanophosphors.* Analytical Chemistry, 2009. **81**(3): p. 930-935.

145. Lim, S.F., et al., *Upconverting nanophosphors for bioimaging.* Nanotechnology, 2009. **20**(40): p. 405701.

146. Kim, F., J.H. Song, and P. Yang, *Photochemical synthesis of gold nanorods.* Journal of the American Chemical Society, 2002. **124**(48): p. 14316-14317.

147. Schwartzberg, A.M., et al., *Synthesis, characterization, and tunable optical properties of hollow gold nanospheres.* The Journal of Physical Chemistry B, 2006. **110**(40): p. 19935-19944.

148. Wiley, B.J., et al., *Synthesis and optical properties of silver nanobars and nanorice.* Nano letters, 2007. **7**(4): p. 1032-1036.

149. Tao, A., P. Sinsermsuksakul, and P. Yang, *Tunable plasmonic lattices of silver nanocrystals.* Nature nanotechnology, 2007. **2**(7): p. 435-440.

150. Wang, L. and W. Tan, *Multicolor FRET silica nanoparticles by single wavelength excitation.* Nano letters, 2006. **6**(1): p. 84-88.

151. Han, M., et al., *Quantum-dot-tagged microbeads for multiplexed optical coding of biomolecules.* Nature biotechnology, 2001. **19**(7): p. 631-635.

152. Heer, S., et al., *Highly efficient multicolour upconversion emission in transparent colloids of lanthanide-doped NaYF4 nanocrystals.* Advanced Materials, 2004.

153. Wang, L. and Y. Li, *Na (Y1. 5Na0. 5) F6 single-crystal nanorods as multicolor luminescent materials.* Nano letters, 2006. **6**(8): p. 1645-1649.

154. Niu, W., et al., *Multicolor output and shape controlled synthesis of lanthanide-ion doped fluorides upconversion nanoparticles.* Dalton Transactions, 2011. **40**(13): p. 3305-3314.

155. Ehlert, O., et al., *A four-color colloidal multiplexing nanoparticle system.* ACS nano, 2008. **2**(1): p. 120-124.

156. Li, Z., Y. Zhang, and S. Jiang, *Multicolor core/shell-structured upconversion fluorescent nanoparticles.* Advanced Materials, 2008. **20**(24): p. 4765-4769.

157. Zhang, H., et al., *Plasmonic modulation of the upconversion fluorescence in NaYF4: Yb/Tm hexaplate nanocrystals using gold nanoparticles or nanoshells.* Angewandte Chemie (International ed. in English), 2010. **49**(16): p. 2865.

158. Li, D., et al., *Influence of the TGA modification on upconversion luminescence of hexagonal-phase NaYF4: Yb3+, Er3+ nanoparticles.* The Journal of Physical Chemistry C, 2010. **114**(18): p. 8219-8226.

159. Huang, Q., et al., *Synthesis and characterization of highly efficient near-infrared upconversion Sc3+/Er3+/Yb3+ tridoped NaYF4.* The Journal of Physical Chemistry C, 2010. **114**(10): p. 4719-4724.

160. Chen, G., et al., *Ultrasmall monodisperse NaYF4: Yb3+/Tm3+ nanocrystals with enhanced near-infrared to near-infrared upconversion photoluminescence.* ACS nano, 2010. **4**(6): p. 3163-3168.

161. Bi, S., J. Zhang, and S. Zhang, *Ultrasensitive and selective DNA detection based on nicking endonuclease assisted signal amplification and its application in cancer cell detection.* Chemical communications, 2010. **46**(30): p. 5509-5511.

162. Song, J., et al., *Self-aggregation of oligonucleotide-functionalized gold nanoparticles and its applications for highly sensitive detection of DNA.* Chemical communications, 2010. **46**(30): p. 5548-5550.

163. Li, H. and L.J. Rothberg, *Label-free colorimetric detection of specific sequences in genomic DNA amplified by the polymerase chain reaction.* Journal of the American Chemical Society, 2004. **126**(35): p. 10958-10961.

164. Rho, S., et al., *Colorimetric detection of ssDNA in a solution.* Current Applied Physics, 2009. **9**(2): p. 534-537.

165. Van De Rijke, F., et al., *Up-converting phosphor reporters for nucleic acid microarrays.* Nature biotechnology, 2001. **19**(3): p. 273-276.

166. Corstjens, P.L., et al., *Lateral-flow and up-converting phosphor reporters to detect single-stranded nucleic acids in a sandwich-hybridization assay.* Analytical biochemistry, 2003. **312**(2): p. 191-200.

167. Zhang, P., et al., *Design of a highly sensitive and specific nucleotide sensor based on photon upconverting particles.* Journal of the American Chemical Society, 2006. **128**(38): p. 12410-12411.

168. Liu, C., et al., *Efficient fluorescence resonance energy transfer between upconversion nanophosphors and graphene oxide: a highly sensitive biosensing platform.* Chemical Communications, 2011. **47**(16): p. 4661-4663.

169. Mader, H.S. and O.S. Wolfbeis, *Optical ammonia sensor based on upconverting luminescent nanoparticles.* Analytical chemistry, 2010. **82**(12): p. 5002-5004.

170. Liu, J., et al., *Iridium (III) complex-coated nanosystem for ratiometric upconversion luminescence bioimaging of cyanide anions.* Journal of the American Chemical Society, 2011. **133**(39): p. 15276-15279.

171. Liu, Q., et al., *High-efficiency upconversion luminescent sensing and bioimaging of Hg (II) by chromophoric ruthenium complex-assembled nanophosphors.* ACS nano, 2011. **5**(10): p. 8040-8048.

172. Sung, H., et al., *Global cancer statistics 2020: GLOBOCAN estimates of incidence and mortality worldwide for 36 cancers in 185 countries.* CA: a cancer journal for clinicians, 2021. **71**(3): p. 209-249.

173. Soerjomataram, I. and F. Bray, *Planning for tomorrow: global cancer incidence and the role of prevention 2020–2070.* Nature reviews Clinical oncology, 2021. **18**(10): p. 663-672.

174. Li, X., et al., *Clinical development and potential of photothermal and photodynamic therapies for cancer.* Nature reviews Clinical oncology, 2020. **17**(11): p. 657-674.

175. Brace, C., *Thermal tumor ablation in clinical use.* IEEE pulse, 2011. **2**(5): p. 28-38.

176. Schena, E., P. Saccomandi, and Y. Fong, *Laser ablation for cancer: past, present and future.* Journal of functional biomaterials, 2017. **8**(2): p. 19.

177. Sultan, R., *Tumour ablation by laser in general surgery.* Lasers in Medical Science, 1990. **5**: p. 185-193.

178. Xie, Z., et al., *Emerging combination strategies with phototherapy in cancer nanomedicine.* Chemical Society Reviews, 2020. **49**(22): p. 8065-8087.

179. Cheng, L., et al., *Functional nanomaterials for phototherapies of cancer.* Chemical reviews, 2014. **114**(21): p. 10869-10939.

180. Shi, H. and P.J. Sadler, *How promising is phototherapy for cancer?* British Journal of Cancer, 2020. **123**(6): p. 871-873.

181. Zhi, D., et al., *Photothermal therapy.* Journal of Controlled Release, 2020. **325**: p. 52-71.

182. Wang, K., et al., *Dual-targeted photothermal agents for enhanced cancer therapy.* Chemical science, 2020. **11**(31): p. 8055-8072.

183. Agostinis, P., et al., *Photodynamic therapy of cancer: an update.* CA: a cancer journal for clinicians, 2011. **61**(4): p. 250-281.

184. Dolmans, D.E., D. Fukumura, and R.K. Jain, *Photodynamic therapy for cancer.* Nature reviews cancer, 2003. **3**(5): p. 380-387.

185. Daniell, M. and J. Hill, *A history of photodynamic therapy.* Australian and New Zealand Journal of Surgery, 1991. **61**(5): p. 340-348.

186. Ackroyd, R., et al., *The history of photodetection and photodynamic therapy¶.* Photochemistry and photobiology, 2001. **74**(5): p. 656-669.

187. Raab, O., *Uber die wirkung fluoreszierender stoffe auf infusorien.* Zeitschr Biol, 1900. **39**: p. 524-546.

188. Sharman, W.M., C.M. Allen, and J.E. van Lier, *[35] Role of activated oxygen species in photodynamic therapy.* Methods in enzymology, 2000. **319**: p. 376-400.

189. Oleinick, N.L., R.L. Morris, and I. Belichenko, *The role of apoptosis in response to photodynamic therapy: what, where, why, and how.* Photochemical & Photobiological Sciences, 2002. **1**(1): p. 1-21.

190. Dougherty, T.J., et al., *Photodynamic therapy.* Journal of National Cancer Institute, 1998. **90**(12): p. 889-905.

191. Brown, S.B., E.A. Brown, and I. Walker, *The present and future role of photodynamic therapy in cancer treatment.* The lancet oncology, 2004. **5**(8): p. 497-508.

192. Dougherty, T.J., *An update on photodynamic therapy applications.* Journal of clinical laser medicine & surgery, 2002. **20**(1): p. 3-7.

193. Stummer, W., et al., *Photodynamic therapy within edematous brain tissue: considerations on sensitizer dose and time point of laser irradiation.* Journal of Photochemistry and Photobiology B: Biology, 1996. **36**(2): p. 179-181.

194. Asadishad, B., M. Vossoughi, and I. Alemzadeh, *Folate-receptor-targeted delivery of doxorubicin using polyethylene glycol-functionalized gold nanoparticles.* Industrial & engineering chemistry research, 2010. **49**(4): p. 1958-1963.

195. Brown, S.D., et al., *Gold nanoparticles for the improved anticancer drug delivery of the active component of oxaliplatin.* Journal of the American Chemical Society, 2010. **132**(13): p. 4678-4684.

196. Jang, B., et al., *Gold nanorod− photosensitizer complex for near-infrared fluorescence imaging and photodynamic/photothermal therapy in vivo.* ACS nano, 2011. **5**(2): p. 1086-1094.

197. Ratanatawanate, C., A. Chyao, and K.J. Balkus Jr, *S-nitrosocysteine-decorated PbS QDs/TiO2 nanotubes for enhanced production of singlet oxygen.* Journal of the American Chemical Society, 2011. **133**(10): p. 3492-3497.

198. Hsieh, J.-M., et al., *Iridium-complex modified CdSe/ZnS quantum dots; a conceptual design for bifunctionality toward imaging and photosensitization.* Chemical Communications, 2006(6): p. 615-617.

199. Tsay, J.M., et al., *Singlet oxygen production by peptide-coated quantum dot− photosensitizer conjugates.* Journal of the American Chemical Society, 2007. **129**(21): p. 6865-6871.

200. Samia, A.C., X. Chen, and C. Burda, *Semiconductor quantum dots for photodynamic therapy.* Journal of the American Chemical Society, 2003. **125**(51): p. 15736-15737.

201. Shi, L., B. Hernandez, and M. Selke, *Singlet oxygen generation from water-soluble quantum dot− organic dye nanocomposites.* Journal of the American Chemical Society, 2006. **128**(19): p. 6278-6279.

202. Shen, X., et al., *Enhanced two-photon singlet oxygen generation by photosensitizer-doped conjugated polymer nanoparticles.* Langmuir, 2011. **27**(5): p. 1739-1744.

203. Chen, Z., et al., *Versatile synthesis strategy for carboxylic acid− functionalized upconverting nanophosphors as biological labels.* Journal of the American Chemical Society, 2008. **130**(10): p. 3023-3029.

204. Chatterjee, D.K. and Z. Yong, *Upconverting nanoparticles as nanotransducers for photodynamic therapy in cancer cells.* Nanomedicine, 2008. **3**(1): p. 73-82.

205. Qian, H.S., et al., *Mesoporous-silica-coated up-conversion fluorescent nanoparticles for photodynamic therapy.* small, 2009. **5**(20): p. 2285-2290.

206. Zhang, P., et al., *Versatile photosensitizers for photodynamic therapy at infrared excitation.* Journal of the American Chemical Society, 2007. **129**(15): p. 4526-4527.

207. Gobin, A.M., et al., *Near infrared laser-tissue welding using nanoshells as an exogenous absorber.* Lasers in Surgery and Medicine: The Official Journal of the American Society for Laser Medicine and Surgery, 2005. **37**(2): p. 123-129.

208. Huang, X., et al., *Cancer cell imaging and photothermal therapy in the near-infrared region by using gold nanorods.* Journal of the American Chemical Society, 2006. **128**(6): p. 2115-2120.

209. Carrasco, E., et al., *Intratumoral thermal reading during photo-thermal therapy by multifunctional fluorescent nanoparticles.* Advanced Functional Materials, 2015. **25**(4): p. 615-626.

210. El-Sayed, H.X., *Plasmonic photo-thermal therapy (PPTT).* Alexandria J. Med, 2011. **47**(1): p. 1-9.

211. Jaque, D., et al., *Nanoparticles for photothermal therapies.* nanoscale, 2014. **6**(16): p. 9494-9530.

212. Johannsen, M., et al., *Clinical hyperthermia of prostate cancer using magnetic nanoparticles: presentation of a new interstitial technique.* International journal of hyperthermia, 2005. **21**(7): p. 637-647.

213. Marmor, J.B., et al., *Treatment of superficial human neoplasms by local hyperthermia induced by ultrasound.* Cancer, 1979. **43**(1): p. 188-197.

214. Dewey, W.C., *Arrhenius relationships from the molecule and cell to the clinic.* International journal of hyperthermia, 1994. **10**(4): p. 457-483.

215. Hildebrandt, B., et al., *The cellular and molecular basis of hyperthermia.* Critical reviews in oncology/hematology, 2002. **43**(1): p. 33-56.

216. Brites, C.D., et al., *Thermometry at the nanoscale.* Nanoscale, 2012. **4**(16): p. 4799-4829.

217. Jaque, D. and F. Vetrone, *Luminescence nanothermometry.* Nanoscale, 2012. **4**(15): p. 4301-4326.

218. Huang, S., et al., *Highly fluorescent and bioresorbable polymeric nanoparticles with enhanced photostability for cell imaging.* Nanoscale, 2015. **7**(3): p. 889-895.

219. Smith, A.M., M.C. Mancini, and S. Nie, *Second window for in vivo imaging.* Nature nanotechnology, 2009. **4**(11): p. 710-711.

220. Bashkatov, A.N., et al., *Optical properties of human skin, subcutaneous and mucous tissues in the wavelength range from 400 to 2000 nm.* Journal of Physics D: Applied Physics, 2005. **38**(15): p. 2543.

221. Marciniak, L., et al., *A broadening temperature sensitivity range with a core–shell YbEr@ YbNd double ratiometric optical nanothermometer.* Nanoscale, 2016. **8**(9): p. 5037-5042.

222. Lupo, M.G., et al., *Ultrafast electron− hole dynamics in core/shell CdSe/CdS dot/rod nanocrystals.* Nano letters, 2008. **8**(12): p. 4582-4587.

223. Li, J., et al., *Nanoparticles-based phototherapy systems for cancer treatment: Current status and clinical potential.* Bioactive Materials, 2023. **23**: p. 471-507.

224. Jain, P.K., et al., *Noble metals on the nanoscale: optical and photothermal properties and some applications in imaging, sensing, biology, and medicine.* Accounts of chemical research, 2008. **41**(12): p. 1578-1586.

225. Zhou, Z., et al., *Tungsten oxide nanorods: an efficient nanoplatform for tumor CT imaging and photothermal therapy.* Scientific reports, 2014. **4**(1): p. 3653.

226. Yin, W., et al., *High-throughput synthesis of single-layer MoS2 nanosheets as a near-infrared photothermal-triggered drug delivery for effective cancer therapy.* ACS nano, 2014. **8**(7): p. 6922-6933.

227. Wang, S., et al., *Biocompatible PEGylated MoS2 nanosheets: controllable bottom-up synthesis and highly efficient photothermal regression of tumor.* Biomaterials, 2015. **39**: p. 206-217.

228. Huang, X., et al., *Etching growth under surface confinement: an effective strategy to prepare mesocrystalline Pd nanocorolla.* Journal of the American Chemical Society, 2011. **133**(40): p. 15946-15949.

229. Averitt, R., D. Sarkar, and N. Halas, *Plasmon resonance shifts of Au-coated Au 2 S nanoshells: insight into multicomponent nanoparticle growth.* Physical Review Letters, 1997. **78**(22): p. 4217.

230. Hirsch, L.R., et al., *Nanoshell-mediated near-infrared thermal therapy of tumors under magnetic resonance guidance.* Proceedings of the National Academy of Sciences, 2003. **100**(23): p. 13549-13554.

231. Loo, C., et al., *Immunotargeted nanoshells for integrated cancer imaging and therapy.* Nano letters, 2005. **5**(4): p. 709-711.

232. Song, G., et al., *A low-toxic multifunctional nanoplatform based on Cu9S5@ mSiO2 core-shell nanocomposites: combining photothermal-and chemotherapies with infrared thermal imaging for cancer treatment.* Advanced Functional Materials, 2013. **23**(35): p. 4281-4292.

233. Tian, Q., et al., *Hydrophilic flower-like CuS superstructures as an efficient 980 nm laser-driven photothermal agent for ablation of cancer cells.* Advanced materials, 2011. **31**(23): p. 3542-3547.

234. Yang, D., et al., *Y 2 O 3: Yb, Er@ mSiO 2–Cu x S double-shelled hollow spheres for enhanced chemo-/photothermal anti-cancer therapy and dual-modal imaging.* Nanoscale, 2015. **7**(28): p. 12180-12191.

235. Dibaba, S.T., et al., *Recent progress of energy transfer and luminescence intensity boosting mechanism in Nd3+-sensitized upconversion nanoparticles.* Journal of Rare Earths, 2019. **37**(8): p. 791-805.

236. Marciniak, L., et al., *Luminescence thermometry with transition metal ions. A review.* Coordination Chemistry Reviews, 2022. **469**: p. 214671.

237. Rocha, U., et al., *Neodymium-doped LaF3 nanoparticles for fluorescence bioimaging in the second biological window.* small, 2014. **10**(6): p. 1141-1154.

238. Chen, G., et al., *Core/shell NaGdF4: Nd3+/NaGdF4 nanocrystals with efficient near-infrared to near-infrared downconversion photoluminescence for bioimaging applications.* ACS nano, 2012. **6**(4): p. 2969-2977.

239. Wang, R., et al., *Epitaxial seeded growth of rare-earth nanocrystals with efficient 800 nm near-infrared to 1525 nm short-wavelength infrared downconversion photoluminescence for in vivo bioimaging.* Angewandte Chemie International Edition, 2014. **53**(45): p. 12086-12090.

240. Zou, X., et al., *An Nd 3+-sensitized upconversion nanophosphor modified with a cyanine dye for the ratiometric upconversion luminescence bioimaging of hypochlorite.* Nanoscale, 2015. **7**(9): p. 4105-4113.

241. Wang, Z., et al., *Nd 3+-sensitized NaLuF 4 luminescent nanoparticles for multimodal imaging and temperature sensing under 808 nm excitation.* Nanoscale, 2015. **7**(42): p. 17861-17870.

242. Söderlund, H., et al., *Increasing depth penetration in biological tissue imaging using 808-nm excited Nd3+/Yb3+/Er3+-doped upconverting nanoparticles.* Journal of biomedical optics, 2015. **20**(8): p. 086008-086008.

243. Zhao, Y., et al., *Optically investigating Nd 3+-Yb 3+ cascade sensitized upconversion nanoparticles for high resolution, rapid scanning, deep and damage-free bio-imaging.* Biomedical optics express, 2015. **6**(3): p. 838-848.

244. Childs, P.R., J. Greenwood, and C. Long, *Review of temperature measurement.* Review of scientific instruments, 2000. **71**(8): p. 2959-2978.

245. Moldover, M.R., W.L. Tew, and H.W. Yoon, *Advances in thermometry.* Nature Physics, 2016. **12**(1): p. 7-11.

246. Allison, S.W. and G. Gillies, *Remote thermometry with thermographic phosphors: Instrumentation and applications.* Review of scientific instruments, 1997. **68**(7): p. 2615-2650.

247. Okabe, K., et al., *Intracellular temperature mapping with a fluorescent polymeric thermometer and fluorescence lifetime imaging microscopy.* Nature communications, 2012. **3**(1): p. 705.

248. Park, Y.I., et al., *Theranostic probe based on lanthanide-doped nanoparticles for simultaneous in vivo dual-modal imaging and photodynamic therapy.* Advanced materials, 2012. **24**(42): p. 5755-5761.

249. Xu, J., et al., *Near-infrared-triggered photodynamic therapy with multitasking upconversion nanoparticles in combination with checkpoint blockade for immunotherapy of colorectal cancer.* ACS nano, 2017. **11**(5): p. 4463-4474.

250. El-Boubbou, K., et al., *Evaluating magnetic and thermal effects of various Polymerylated magnetic iron oxide nanoparticles for combined chemo-hyperthermia.* New Journal of Chemistry, 2022. **46**(12): p. 5489-5504.

251. Brites, C., A. Millán, and L. Carlos, *Lanthanides in luminescent thermometry*, in *Handbook on the physics and chemistry of rare earths*. 2016, Elsevier. p. 339-427.

252. Dramićanin, M.D., *Trends in luminescence thermometry.* Journal of Applied Physics, 2020. **128**(4).

253. Quintanilla, M., et al., *Intense ultraviolet upconversion in water dispersible SrF 2: Tm 3+, Yb 3+ nanoparticles: the effect of the environment on light emissions.* Journal of Materials Chemistry C, 2015. **3**(13): p. 3108-3113.

254. Runowski, M., et al., *Multifunctional optical sensors for nanomanometry and nanothermometry: high-pressure and high-temperature upconversion luminescence of*

lanthanide-doped phosphates—LaPO4/YPO4: Yb3+–Tm3+. ACS applied materials & interfaces, 2018. **10**(20): p. 17269-17279.

255. Goderski, S., et al., *Lanthanide upconverted luminescence for simultaneous contactless optical thermometry and manometry–sensing under extreme conditions of pressure and temperature.* ACS Applied Materials & Interfaces, 2020. **12**(36): p. 40475-40485.

256. Ximendes, E.C., et al., *In vivo subcutaneous thermal video recording by supersensitive infrared nanothermometers.* Advanced Functional Materials, 2017. **27**(38): p. 1702249.

257. Runowski, M., *Pressure and temperature optical sensors: luminescence of lanthanide-doped nanomaterials for contactless nanomanometry and nanothermometry*, in *Handbook of Nanomaterials in Analytical Chemistry*. 2020, Elsevier. p. 227-273.

258. Stefańska, J., A. Bednarkiewicz, and L. Marciniak, *Advancements in excited state absorption-based luminescence thermometry.* Journal of Materials Chemistry C, 2022. **10**(15): p. 5744-5782.

259. Labrador-Paez, L., et al., *Reliability of rare-earth-doped infrared luminescent nanothermometers.* Nanoscale, 2018. **10**(47): p. 22319-22328.

260. Stopikowska, N., et al., *Influence of excitation and detection geometry on optical temperature readouts–reabsorption effects in luminescence thermometry.* Journal of Materials Chemistry C, 2023. **11**(28): p. 9620-9627.

261. Hemmer, E., et al., *Exploiting the biological windows: current perspectives on fluorescent bioprobes emitting above 1000 nm.* Nanoscale horizons, 2016. **1**(3): p. 168-184.

262. Choi, S., et al., *Ultrasensitive all-optical thermometry using nanodiamonds with a high concentration of silicon-vacancy centers and multiparametric data analysis.* ACS photonics, 2019. **6**(6): p. 1387-1392.

263. Zheng, T., et al., *Tm2+ activated SrB4O7 bifunctional sensor of temperature and pressure—highly sensitive, multi-parameter luminescence thermometry and manometry.* Advanced Optical Materials, 2021. **9**(22): p. 2101507.

264. Maturi, F.E., et al., *Going Above and Beyond: A Tenfold Gain in the Performance of Luminescence Thermometers Joining Multiparametric Sensing and Multiple Regression (Laser Photonics Rev. 15 (11)/2021).* Laser & Photonics Reviews, 2021. **15**(11).

265. Binnemans, K., *Lanthanide-based luminescent hybrid materials.* Chemical reviews, 2009. **109**(9): p. 4283-4374.

266. Wybourne, B.G. and L. Smentek, *Optical spectroscopy of lanthanides: magnetic and hyperfine interactions*. 2007: CRC press.

267. Skripka, A., et al., *Advancing neodymium single-band nanothermometry.* Nanoscale, 2019. **11**(23): p. 11322-11330.

268. Wang, D., et al., *808 nm driven Nd 3+-sensitized upconversion nanostructures for photodynamic therapy and simultaneous fluorescence imaging.* Nanoscale, 2015. **7**(1): p. 190-197.

269. Ai, F., et al., *A core-shell-shell nanoplatform upconverting near-infrared light at 808 nm for luminescence imaging and photodynamic therapy of cancer.* Scientific reports, 2015. **5**(1): p. 10785.

270. Rocha, U., et al., *Nd3+ doped LaF3 nanoparticles as self-monitored photo-thermal agents.* Applied Physics Letters, 2014. **104**(5).

271. Xu, W., et al., *Multifunctional nanoparticles based on the Nd 3+/Yb 3+ codoped NaYF 4.* Optics letters, 2015. **40**(23): p. 5678-5681.

272. Chen, Y., et al., *Multifunctional Nd 3+-sensitized upconversion nanomaterials for synchronous tumor diagnosis and treatment.* Nanoscale, 2015. **7**(18): p. 8574-8583.

273. He, F., et al., *Optimization of upconversion luminescence of Nd 3+-sensitized BaGdF 5-based nanostructures and their application in dual-modality imaging and drug delivery.* Dalton Transactions, 2016. **45**(4): p. 1708-1716.

274. Shanthakumari, D., S. Srinivasalu, and S. Subramanian, *Effect of fluoride intoxication on lipidperoxidation and antioxidant status in experimental rats.* Toxicology, 2004. **204**(2-3): p. 219-228.

275. Shivarajashankara, Y., et al., *Histological changes in the brain of young fluoride-intoxicated rats.* Fluoride, 2002. **35**(1): p. 12-21.

276. Rao, M., S. Chawla, and N. Patel, *Melatonin reduction of fluoride-induced nephrotoxicity in mice.* Fluoride, 2009. **42**(2): p. 110.

277. Chen, G., et al., *Energy-cascaded upconversion in an organic dye-sensitized core/shell fluoride nanocrystal.* Nano letters, 2015. **15**(11): p. 7400-7407.

278. Hao, S., et al., *Enhancing dye-sensitized solar cell efficiency through broadband near-infrared upconverting nanoparticles.* Nanoscale, 2017. **9**(20): p. 6711-6715.

279. Hao, S., et al., *Nd 3+-Sensitized multicolor upconversion luminescence from a sandwiched core/shell/shell nanostructure.* Nanoscale, 2017. **9**(30): p. 10633-10638.

280. Estebanez, N., et al., *Breaking the Nd 3+-sensitized upconversion nanoparticles myth about the need of onion-layered structures.* Nanoscale, 2018. **10**(26): p. 12297-12301.

281. Rafique, R., et al., *Morphological evolution of upconversion nanoparticles and their biomedical signal generation.* Scientific reports, 2018. **8**(1): p. 17101.

282. Zhou, Y., *Controllable design, synthesis and characterization of nanostructured rare earth metal oxides.* Physical Sciences Reviews, 2020. **5**(3): p. 20180084.

283. Yu, Z., C. Eich, and L.J. Cruz, *Recent advances in rare-earth-doped nanoparticles for NIR-II imaging and cancer theranostics.* Frontiers in Chemistry, 2020. **8**: p. 496.

284. Mehra, S., et al., *Core/shell approach to dopant incorporation and shape control in colloidal zinc oxide nanorods.* Chemistry of Materials, 2016. **28**(10): p. 3454-3461.

285. Zhou, Z., et al., *Core–Shell Interface Engineering Strategies for Modulating Energy Transfer in Rare Earth-Doped Nanoparticles.* Nanomaterials, 2024. **14**(16): p. 1326.